**FEDERAL UNIVERSITY OF ALAGOAS - UFAL**
**GRADUATE PROGRAM IN PHYSICS**


**CATHARINA BATISTA DE ARAUJO**


**THEORETICAL-EXPERIMENTAL STUDY OF SOLVENTS' EFFECTS ON THE SPECTROSCOPIC PROPERTIES OF ORGANIC MOLECULES**


**MACEIÓ**
**2024**

**CATHARINA BATISTA DE ARAUJO**

# THEORETICAL-EXPERIMENTAL STUDY OF SOLVENTS' EFFECTS ON THE SPECTROSCOPIC PROPERTIES OF ORGANIC MOLECULES

Thesis has been presented to the Federal University of Alagoas—UFAL— as part of the prescribed criteria for the conferment of the Doctor of Physics degree.

Supervisor: Prof. Dr. Italo Nunes de Oliveira
Co-supervisor: Prof. Dr. Vinícius Manzoni Vieira

**Maceió**
**2024**

## PARECER DA BANCA EXAMINADORA DE DEFESA DE

## TESE DE DOUTORADO

**"Estudo téorico-experimental dos efeitos de solvente sobre as propriedades espectroscópicas de moléculas orgânicas"**

**por**

**Catharina Batista de Araújo**

A Banca Examinadora composta pelos professores Italo Marcos Nunes de Oliveira, como presidente da banca examinadora e orientador, do Instituto de Física da Universidade Federal de Alagoas; Vinícius Manzoni Vieira, como coorientador, do Instituto de Física da Universidade Federal de Alagoas; Maria Socorro Seixas Pereira, do Instituto de Física da Universidade Federal de Alagoas; Francisco Anacleto Barros Fidelis de Moura, do Instituto de Física da Universidade Federal de Alagoas; Rodrigo do Monte Gester, da Universidade Federal do Sul e Sudeste do Pará; e Dimas José da Paz Lima, da Universidade Federal Rural de Pernambuco; consideram a **candidata aprovada com conceito A**.

Maceió, 23 de agosto de 2024.

Prof. Dr. Italo Marcos Nunes de Oliveira

Prof. Dr. Vinícius Manzoni Vieira

Profª Drª Maria Socorro Seixas Pereira

Prof. Dr. Francisco Anacleto Barros Fidelis de Moura

Prof. Dr. Rodrigo do Monte Gester

Prof. Dr. Dimas José da Paz Lima

*This thesis is dedicated to adult children who have dreamed of becoming scientists.*

# Agradecimentos

Minha mais profunda gratidão aos meus pais, Maria Liege e José Cristiano, cujos valores moldaram a trajetória que me trouxe até aqui. Vocês sempre enfatizaram a importância da educação, não apenas como um caminho para a realização profissional, mas como um meio para enfrentar as adversidades. Suas escolhas (e sacrifícios) permitiram que eu e a Chris pudéssemos nos dedicar integralmente à essa caminhada, e por isso, serei eternamente grata. Este trabalho é tanto fruto do meu esforço quanto do apoio incondicional e do AMOR que vocês me deram.

À minha irmã, Christiane, que esteve comigo em cada passo (literalmente). Não tenho memória em que você não esteja e sua companhia é CONFORTO. Saber que sempre posso contar com você faz toda a diferença.

Ao meu orientador, professor Italo Nunes, que me acompanhou ao longo dos últimos 10 anos. Muito obrigada por todo ensinamento, desde a iniciação científica até o mestrado e, agora, doutorado. Sua orientação não só moldou meu desenvolvimento acadêmico, mas também me inspirou a alcançar novos patamares. Sua paciência, e apoio foram fundamentais para que eu pudesse trilhar esse caminho. Sou profundamente grata por todas as lições, conselhos e, acima de tudo, pela CONFIANÇA durante todos esses anos.

Agradeço sinceramente ao meu coorientador, professor Vinícius Manzoni, pelo apoio e pela disponibilidade para discutir e orientar em cada fase do processo. Sua colaboração foi crucial para que eu pudesse concluir esta etapa. Você que foi meu professor em diversas disciplinas durante a graduação e no doutorado. Seu compromisso com a formação dos seus alunos sempre foi evidente e influenciou profundamente minha trajetória acadêmica. Muito obrigada.

Aos meus colegas da Sala 6. Os momentos de risada, descontração e as conversas animadas, sempre regados a muito café, tornaram a jornada mais leve e prazerosa. Aos meus amigos do grupo de pesquisa, GLAP, que estiveram ao meu lado. Agradeço especialmente ao Raul pelo apoio. À Lavínia, que auxiliou no desenvolvimento deste trabalho. À Pam, seja discutindo física ou compartilhando uma dica literária. À Rafa, exemplo de comprometimento. E ao Waltinho, meu companheiro de jornada há 10 anos. Juntos em todas as disciplinas da graduação e da pós-graduação. Você é mais que um amigo e sou profundamente grata por tudo que compartilhamos ao longo desses anos. Ao Luciano, a primeira pessoa com quem conversei ao entrar na universidade, e que possui um coração gigante. Ao Matheus, agradeço pela constante disposição em ajudar, sempre paciente e atento. E ao Adenilson, exemplo de força e resiliência.

Agradeço ao Luís Paulo (Pato), pela contribuição para a realização desta pesquisa. Muito obrigada.

Gratidão a todos os colegas do Instituto de Física e aos funcionários que tornam o nosso ambiente mais acolhedor. Um agradecimento especial para o Miguel.

Gostaria de agradecer a todos os professores do Instituto de Física. Em especial, agradeço à professora Maria Tereza, exemplo de profissional e artista; à professora Socorro, por me acompanhar e ajudar desde a graduação; ao professor Marcelo Lyra, que admiro profundamente, e à professora Solange, pelos "sacodes" quando necessário. Agradeço ao professor Rodrigo Gester, pela orientação e ensinamentos, mesmo que por um período breve, mas extremamente enriquecedor.

Ao Naíbe, pela compreensão e paciência durante todo este período. Quem entende minha ausência e sempre demonstra completa empatia. Obrigada por cada gesto de carinho, por me apoiar nos momentos difíceis e por celebrar comigo cada conquista. Você trouxe amor, alegria e força.

Ao Galileu. Entre pensamentos e ideias, lá estava você, fiel amigo de quatro patas. Nas noites de estudo, você sempre permaneceu ao meu lado. Desde o início da graduação, seu silêncio é companhia.

Às agências de fomento CAPES, CNPq e FAPEAL .

*Begin at the beginning, the King said gravely,* "and go on till you come to the end: *then stop.*"

—Lewis Carroll, *Alice in Wonderland*

# RESUMO

Este estudo explora as propriedades fotoquímicas e espectroscópicas de moléculas orgânicas conjugadas. A pesquisa teve como base analisar o efeito de diversos solventes nas propriedaes ópticas. A análise da fluorescência a partir das soluções do PY-RES variando a polaridade permitiu observar o efefito solvatocrômico. A análise do deslocamento de Stokes revelou uma variação no momento dipolar molecular de 4,57 D após a excitação com o lasr de 450nm, consistente com os valores da literatura para compostos semelhantes. O comportamento das soluções com do PY-RES a partir do aumento da temperatura indicou uma diminuição na intensidade de emissão, especialmente em solventes menos polares, sugerindo que a temperatura não altera significativamente a diferença de energia entre os estados excitado e fundamental dentro de uma faixa de 25 a 40 °C. A sensibilidade do PY-RES à polaridade do solvente destaca seu potencial como uma sonda físico-química para detectar adulteração de solventes, evidenciada pelas mudanças de emissão ratiométricas em misturas de etanol e metanol.

O curcuminóide (*1E,4E*-1,5-bis(4-(dimetilamino)fenil)penta-1,4-dien-3-ona) foi examinado quanto aos seus espectros de absorção e emissão em vários solventes. Os resultados experimentais, apoiados por simulações de Teoria do Funcional da Densidade Dependente do Tempo (TDDFT), indicaram fortes efeitos da polaridade do solvente nos espectros de fluorescência. Os máximos de absorção variaram de 400 nm a 460 nm, com um deslocamento batocrômico observado em solventes mais polares, atingindo um pico de 458 nm no metanol. Estudos computacionais com o funcional B3LYP revelaram um intervalo HOMO-LUMO de 2,8 eV e um pico de absorção teórico próximo ao valor experimental no metanol. O curcuminóide exibiu um alto deslocamento de Stokes no metanol (175,6 nm), aumentando com a polaridade do solvente, sugerindo mudanças significativas na distribuição de carga após a excitação. A decomposição espectral e a análise de decaimento de intensidade confirmaram propriedades de emissão dependentes do solvente e o impacto da temperatura na intensidade de emissão sem alterar a forma espectral. Esses achados destacam o potencial da curcumina monocarbonil como uma sonda sensível ao ambiente.

O chalconóide *(E)-1-(4-aminofenil)-3-(4-(dimetilamino)fenil)prop-2-en-1-ona* foi investigado por meio de espectroscopia UV-vis e cálculos teóricos. O composto exibiu duas bandas principais de absorção correspondentes às transições $\pi - \pi^*$ e $n - \pi^*$, com deslocamentos significativos dependentes do solvente. Um deslocamento batocrômico foi particularmente notável em solventes menos polares como heptano e tolueno. Análises teóricas usando o funcional CAM-B3LYP e o conjunto de bases 6-311+G(d,p) corroboraram os achados experimentais, detalhando uma diferença de energia de transição HOMO-LUMO de 5,406 eV em acetonitrila e uma diferença de transição $n - \pi^*$ de 6,5 eV. Estudos de fluorescência revelaram um deslocamento de Stokes substancial em solventes apolares, reforçando a sensibilidade do composto ao ambiente do solvente e seu potencial em aplicações optoeletrônicas e farmacêuticas.

**Palavras-chave**: PY-RES, Chalcona, Monocarbonil Curcumin, Fluorescência, Propriedades Espectroscópicas

# ABSTRACT

The research focuses on the photochemical and spectroscopic properties of conjugated organic molecules. The study was based on exploring the effect of different solvents on the optical properties. The fluorescence analysis from PY-RES solutions varying the polarity allowed us to observe the solvatochromic effect. The Stokes shift analysis revealed a variation in the molecular dipole moment of 4.57 D after excitation with the 450 nm laser, consistent with the literature values for similar compounds. The behavior of PY-RES solutions as the temperature increased indicated a decrease in emission intensity, especially in less polar solvents. The sensitivity of PY-RES to solvent polarity highlights its potential as a physicochemical probe for detecting solvent adulteration, evidenced by the ratiometric emission changes in ethanol-methanol mixtures.

Monocarbonyl Curcumin (*1E,4E*-1,5-bis(4-(dimethylamino)phenyl)penta-1,4-dien-3-one) was examined for its electronic absorption and fluorescence spectra across various solvents. Experimental results, supported by Time-Dependent Density Functional Theory (TDDFT) simulations, indicated strong solvent polarity effects on fluorescence spectra. Absorption maxima ranged from 400 nm to 460 nm, with a bathochromic shift observed in more polar solvents, peaking at 458 nm in methanol. Computational studies with the B3LYP functional revealed a HOMO-LUMO gap of 2.8 eV and a theoretical absorption peak near the experimental value in methanol. Monocarbonyl Curcumin exhibited a high Stokes shift in methanol (175.6 nm), increasing with solvent polarity, suggesting significant changes in charge distribution upon excitation. Spectral decomposition and intensity decay analysis confirmed solvent-dependent emission properties and the impact of temperature on emission intensity without altering spectral shape. These findings highlight the potential of curcumin monocarbonyl as an environment-sensitive probe.

The chalconoid (E)-1-(4-aminophenyl)-3-(4-(dimethylamino)phenyl)prop-2-en-1-one was investigated through UV-vis spectroscopy and theoretical calculations. The compound exhibited two main absorption bands corresponding to $\pi - \pi^*$ and $n - \pi^*$ transitions, with significant solvent-dependent shifts. A bathochromic shift was particularly notable in less polar solvents like heptane and toluene. Theoretical analyses using the CAM-B3LYP functional and the 6-311+G(d,p) basis set corroborated experimental findings, detailing a HOMO–LUMO transition energy gap of 5.406 eV in acetonitrile and an $n - \pi^*$ transition gap of 6.5 eV. Fluorescence studies revealed a substantial Stokes shift in nonpolar solvents, reinforcing the compound's sensitivity to the solvent environment and its potential in optoelectronic and pharmaceutical applications.

**Keywords**: PY-RES, Monocarbonyl Curcumin, Chalconoid, Fluorescence, Spectroscopic Properties

# CONTENTS

# LIST OF FIGURES

| | |
|---|---|
| B3LYP | Becke, three-parameter, Lee-Yang-Parr |
| CAM-B3LYP | Coulomb-attenuating method B3LYP |
| cc | correlation-consistent |
| DFT | Density Functional Theory |
| DZ | Double Zeta |
| DZP | Double Zeta Valence |
| GGA | generalized gradient approximation |
| GTOs | Gaussian-type orbitals |
| GTF | Gaussian-type function |
| HF | Hartree-Fock |
| HGGA | hyper-generalized gradient approximation |
| HOMO | highest occupied molecular orbital |
| KS | Kohn-Sham |
| LSD | local spin density |
| LSDA | Local Spin Density Approximation |
| LUMO | lowest unoccupied molecular orbital |
| MC | Monte Carlo |
| MD | Molecular Dynamics |
| meta-GGA | meta-generalized gradient approximation |
| MO | Molecular orbital |
| MP | Møller-Plesset |
| MPn | Møller-Plesset series |
| PBE | Perdew-Burke-Ernzerhof |
| PW91 | Perdew-Wang 91 |
| QZ | Quadruple Zeta |
| RHF | Restricted Hartree-Fock |
| RPA | Random Phase Approximation |
| Rydberg states | high-energy excited states of atoms |
| SCF | Self-Consistent Field |
| STO | Slater-type orbital |
| STO-NG | Slater-type orbital with N Gaussian functions |
| SV | Split-Valence |
| TPSS | Tao-Perdew-Staroverov-Scuseria |
| TZ | Triple Zeta |

# LIST OF TABLES

# INTRODUCTION

F LUORESCENCE is a physical phenomenon with significant applications in various fields of science and technology, being frequently employed by researchers in the development of chemical and biological sensors [2–5]. Using fluorescent probes, researchers can extract valuable information about physicochemical processes occurring in complex systems. These probes have broad applications in clinical diagnostics, DNA sequencing, genetic analysis, bioimaging, environmental monitoring, and forensic science, among other areas [6–9].

Many physical systems exhibit fluorescence, mainly inorganic nanoparticles, rare earth ion-doped glasses, and organic materials [10–12]. It is these organic materials that are especially important for the development of this study.

This chapter's main proposal is to perform a comprehensive historical analysis of fluorescence research. This will cover the properties of light from the earliest optical studies to the investigations related to the central phenomenon addressed in this thesis.

## 1.1 WHAT IS LIGHT

Researchers have persistently studied light characteristics, given their vital importance to maintaining life. In the 18th century, the English physicist Isaac Newton proposed that light could behave as a particle. In his book "Opticks", published in 1704, Newton argued that light was composed of particles, which he called "corpuscles" [13]. However, in 1804, Thomas Young conducted an experiment known as the Double-Slit Experiment, which showed that light could be described as a wave [14].

In 1865, James Clerk Maxwell developed the mathematical theory that describes light as an electromagnetic wave [15]. He showed that light is a form of energy that travels through space in waves that are perpendicular to each other. Nonetheless, in the early 20th century, Max Planck began investigating the thermal radiation emitted by objects and realized that classical physics laws could not explain everything. To better understand this, Planck proposed that energy was not emitted continuously, as previously thought, but in small packets, which he called "quanta" [16].

These packets of energy differ from physical objects that move continuously. Instead, the quanta have a specific energy that is directly proportional to the frequency of the radiation. The equation $E = h\nu$ determines the energy of the quanta, where $E$ is the energy of the quanta, $h$ is

Planck's constant, and $\nu$ is the frequency of the radiation. As the frequency of electromagnetic radiation rises, the energy of the associated quanta also increases.

Although scientists initially met the idea of quanta with skepticism, it eventually became a fundamental principle of modern physics. Max Planck's discovery fundamentally changed our understanding of the nature of energy and matter and paved the way for many technological and scientific advances of the 20th century.

In 1905, Albert Einstein proposed a theory describing light as a subatomic particle called a photon [17]. He showed that photons have energy and momentum like other subatomic particles, such as electrons and protons. Such a theory, called the Photoelectric Effect Theory, has many critical technological applications, including solar cells [18], radiation detectors [19], and optical sensors [20]. Since then, researchers have focused on studying the properties of light as both a wave and a particle, known as wave-particle duality. From a theoretical perspective, Schrödinger's equation [21] describes the time evolution of a quantum system.

Researchers have studied light and its properties in different media, such as air, water, and glass. They have found that light undergoes refraction, a phenomenon where a beam changes direction as it passes from one medium to another due to the change in speed in different environments. This event is responsible for notable phenomena, such as the formation of rainbows [22]. Snell's Law mathematically describes this phenomenon. This Law states that the angle of incidence and the angle of refraction of light are related by the ratio of the refractive indices of the two media. Mathematically, the law is expressed as $n_1 \cdot \sin(\theta_1) = n_2 \cdot \sin(\theta_2)$, where $n_1$ and $n_2$ are the refractive indices of the media, and $\theta_1$ and $\theta_2$ are the angles of incidence and refraction, respectively. Snell's Law is a fundamental tool for understanding optics and applying its concepts in various fields, from technology to the understanding of natural phenomena [23, 24].

The German physicist and historian Eilhard Wiedemann first introduced the term luminescence as *luminescenz* in 1888 for all light emission phenomena that are not solely conditioned by an increase in temperature, that is, by incandescence [25]. However, based on the current understanding of luminescence, we classify the groups related to this phenomenon according to the excitation mode. In particular, we define *photoluminescence* as the light emission resulting "from the direct photoexcitation of the emitting species" [26]. Fluorescence, phosphorescence, and delayed fluorescence are widely recognized as examples of *photoluminescence*.

Therefore, the next section will introduce the topic of fluorescence in light of historical context by comprehensively and contextually describing some of the earliest milestones in studying this phenomenon.

## 1.2 EVOLUTION OF FLUORESCENCE STUDIES

The French mineralogist René-Just Haüy mentioned in the second edition of his treatise on mineralogy, published in 1822 [27], the two colors of some fluorite crystals, as illustrated in Figure 1. He described the color of reflected light as violet, while the color of transmitted light was green [25]. Haüy elucidated the phenomenon by stating that the two colors in question were complementary, with violet as the predominant hue in reflected light. At the same time, green was the dominant hue in transmitted light. Although his explanation was incorrect, Haüy's vision and the mineral fluorite played a central role in the understanding and nomenclature of fluorescence.

**Figure 1** – *Green fluorite crystals illuminated by sunlight (left) and a UV lamp (right).*
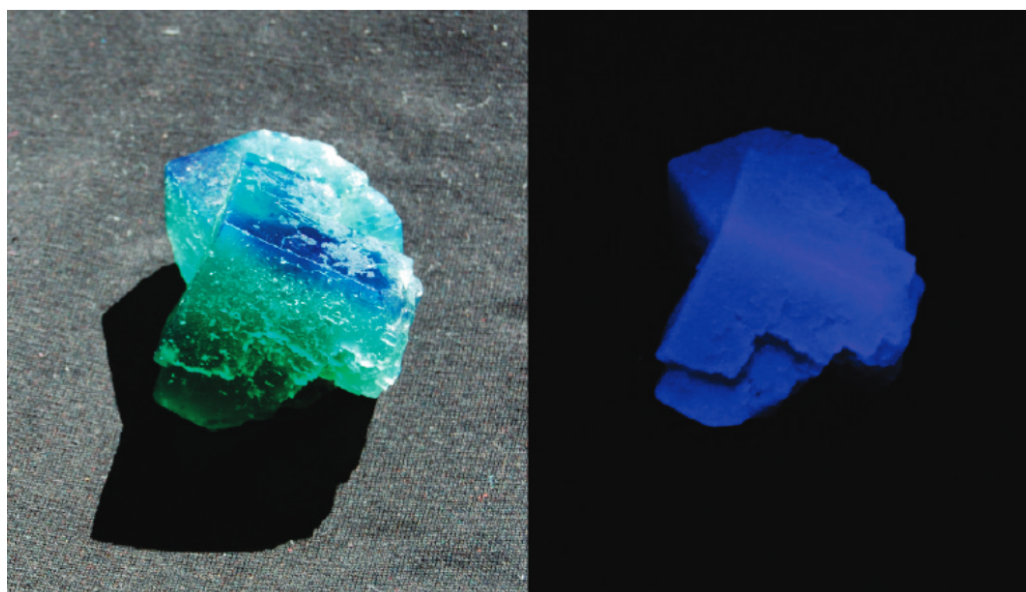


*Valeur & Berberan-Santos, 2011 [25].*

Since George Stokes conducted research in the mid-19th century, fluorescence has been the subject of studies and investigations in various scientific fields. Stokes, a British physicist and mathematician, analyzed fluorescence while investigating the luminescence properties in minerals. He observed that certain materials emit light in colors different from those they absorb when exposed to UV light [28]. Stokes named this phenomenon fluorescence in honor of fluorite, which is the same mineral René-Just Haüy analyzed.

In 1864, the French physicist Eduard Becquerel studied fluorescence in chemical solutions and discovered that fluorescence intensity decreases with increasing sample concentration. He also observed that this phenomenon is affected by the pH of the solution [28].

In 1888, the German physicist Heinrich Kayser conducted important experiments on fluores-

cence and its properties in the late 19th and early 20th centuries. He studied how temperature affects fluorescence and its characteristics, such as intensity and emission wavelength [28].

In 1901, the German physician Paul Ehrlich conducted a significant experiment that marked the beginning of fluorescent dyes in biological studies. Ehrlich discovered that these dyes could selectively bind to different cellular components, allowing the identification and visualization of specific structures in cells and tissues [29].

Ehrlich's discoveries significantly impacted the development of fluorescence microscopy and other techniques for visualizing cells and tissues. Using fluorescent dyes, Ehrlich identified and differentiated different types of blood cells, and he studied the distribution of mitochondria and other cellular organelles. His findings provided a deeper understanding of the structure and function of cells.

In 1924, F. Perrin, a French physicist, and F. Jablonski, a Polish chemist, studied the kinetics of fluorescence. They realized that the amount of light a molecule emits is affected by the speed of the chemical reactions occurring within it. In other words, the faster these chemical reactions occur, the weaker the light emitted by the sample [30].

In 1949, the German chemist A. Kuhn and the Japanese biologist K. Shimomura analyzed green fluorescent protein (GFP) in a species of jellyfish [31]. They discovered that GFP emits green light when exposed to UV light and realized it could be used to study biological processes in living cells.

The evolution of lasers in the 1960s marked a significant change in how researchers use fluorescence. Before this, excitation techniques were limited and imprecise, making it challenging to investigate processes at the molecular level. With the advent of lasers, researchers could selectively excite specific molecules using monochromatic light, increasing the sensitivity and resolution of fluorescence studies. Lasers provide a highly directional, coherent[1] light source with a single wavelength, allowing controlled excitation of molecules.

Fluorescence has become an indispensable tool in a wide range of scientific fields, including biology, chemistry, physics, medical sciences, and materials science. Its applications are diverse, from studying biological processes in living cells to detecting and quantifying molecules in solutions, and even exploring the properties of materials on a nanometric scale.

From observations concerning the study of photoluminescence, researchers have verified that some molecules are responsible for various visible effects in compounds, such as chromophores, which play a crucial role in the phenomenon of fluorescence. A chromophore is the specific region of a molecule where light absorption occurs, as well as the primary alteration in its geometry or electronic density. Detailed studies are required to precisely delimit the chromophore area in relation to the residual parts of the molecule, which do not actively participate in the absorption process.

---

[1]A form of light in which the waves have the same frequency, direction, phase, and polarization.

The evolution and developments of fluorescence studies since George Stokes' discovery and its application in different scientific fields reflect the importance and versatility of this optical phenomenon. Thus, the next section will discuss some of these applications.

## 1.3 APPLICATIONS OF FLUORESCENCE

### 1.3.1 EXAMPLES IN NATURE

Many organic beings, both animals and plants, exhibit fluorescence. For example, many species of jellyfish have fluorescent proteins in their tentacles and oral discs, emitting green, yellow, or red light. *Atolla wyvillei*, a species of jellyfish found in the deep waters of the Atlantic Ocean, is notable for its ability to produce fluorescence in response to external stimuli, such as the presence of predators or water turbulence [32]. Its body is usually transparent, with thin, long tentacles that extend to capture prey. Scientists study the bioluminescence and fluorescence of *Atolla wyvillei* to understand better the biological and chemical processes involved. Figure 2 shows an image of this jellyfish.

**Figure 2** *– Atolla wyvillei: A jellyfish found in the deep waters of the Atlantic Ocean, capable of producing bioluminescence and fluorescence in response to external stimuli.*
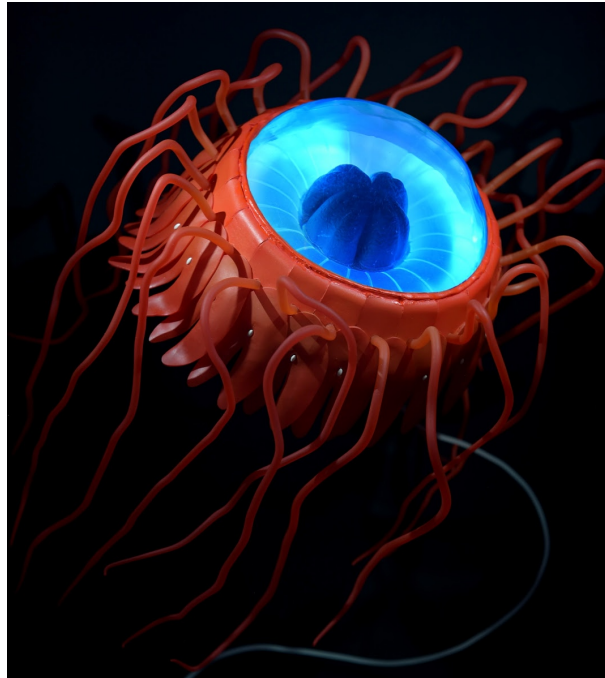


*Alarm Jellyfish, Google Arts & Culture, 2023 [33].*

Corals also exhibit fluorescence due to their symbiotic relationship with algae that perform photosynthesis within their tissues. Some of these algae produce fluorescent proteins, which help

absorb light and protect the coral from ultraviolet radiation [34, 35]. *Turbinaria reniformis*, also known as Dendro coral, is a species of coral that exhibits fluorescence. This species is common in reefs in the tropical and subtropical areas of the Indian and Pacific Oceans. The fluorescence observed in *Turbinaria reniformis* occurs due to the presence of specific fluorescent proteins. When exposed to an excitation source, these proteins emit light in the green-yellow range, such as ultraviolet light.

Some plant species, such as açaí and passion fruit, also exhibit fluorescence in their fruits. Additionally, chlorophyll, the pigment responsible for photosynthesis, can exhibit this phenomenon under certain conditions.

Fluorescence is significant not only from a biological perspective but also has essential applications in medicine, DNA and protein analysis, pathogen detection, biotechnology, materials science, and the cosmetics and paint industries [36–40].

### 1.3.2 USE OF CHROMOPHORES AND THE PHENOMENON OF FLUORESCENCE IN SOCIETY

In science and technology, chromophores are essential components that serve various purposes, including aiding in forensic analysis, detecting contaminants, and identifying biological markers.

The yellow chromophore of bilirubin, highlighted in Causin's study [41], plays a crucial role in forensic science, allowing the distinction of the timing of bruise occurrences. Observing bruises under different lighting conditions reveals the presence of the chromophore, which progressively accumulates in the injured area over time. This phenomenon distinguishes between recent bruises, which predominantly contain blood, and older ones, which exhibit a higher bilirubin concentration. Such distinction is crucial for estimating the age of an injury, providing valuable insights for investigations.

The chromophore temoporfin, a lipophilic photosensitizer for photodynamic therapy, is a practical sensor of metallic pollutants in water. In a study conducted by Bhimsen Rout [42], temoporfin demonstrated differential responses to metal binding at multiple absorption wavelengths, which utilized chemometric analysis[2]. This capability allows rapid detection and discrimination of a wide range of metals, including those known to cause adverse effects on human health, such as chromium, manganese, mercury, cadmium, zinc, copper, silver, lead, and nickel.

### 1.3.3 UNDERSTANDING THE ELECTRONIC STRUCTURE IN THE EXCITED STATE

Fluorescence plays a crucial role in investigating the electronic configuration of the excited state of aromatic molecules, such as Prodan, Laurdan, and Benzil, when in various solvents,

---

[2]Measurements performed in a chemical system or process, obtaining information about the system's state through the application of mathematical or statistical methods.

which exhibit anomalous behavior and exceptions to Kasha's rule, a topic addressed in Chapter 4.

A point of debate in studies concerning Prodan and Laurdan (molecular structure illustrated in Figure 3) relates to the nature of the excited state, evidenced by the presence of two lifetimes. One interpretation for this dual emission [43, 44] attributes it to two distinct excited states, $S_1$ and $S_2$, highlighting the anomalous behavior concerning Kasha's rule. The authors decomposed spectra into two Gaussian bands and conducted lifetime measurements, which corroborated their interpretation [43, 44].

**Figure 3** – *Molecular structure of Prodan and Laurdan.*
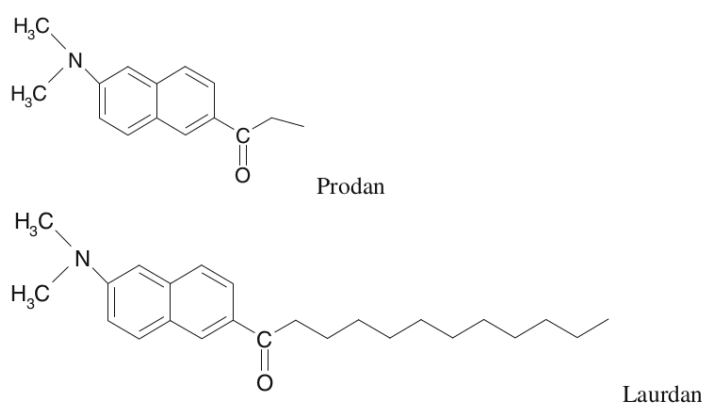


*Vequi-Suplicy CC et al., 2015 [43].*

Bhattacharya et al. [45] aimed to identify the origin of multiple emissions and characterize the different conformations of Benzil in various electronic states. They analyzed the multiple fluorescences of the molecular system, observing that the distorted form of Benzil emits from the $S_1$ state and the second excited state $S_2$, depending on the excitation wavelength.

Given the various applications of understanding the electronic structure and the phenomenon of fluorescence, this study will focus on analyzing the theoretical concepts surrounding it. In particular, it emphasizes the solvent effect on emission.

## 1.4 GENERAL PRESENTATION OF THE THESIS

In this research, we aim to investigate the emission process of organic compounds in different solvents, varying the polarity of the medium. In particular, we examined three compounds: a pyrrole-derived monomer linked to resorufin named Py-res, a chalconoid, and a curcuminoid. Additionally, we examine the most suitable computational methods to describe the systems of interest and compare and complement the experimental results obtained.

Chapter 2 of the thesis thoroughly covers the evolution and foundational aspects of molecular

orbital theory. It begins with historical models of the atom and introduces Robert S. Mulliken's development of molecular orbital theory, emphasizing atomic orbitals and their quantum mechanical descriptions. The chapter details hydrogen-like, Slater-type, and Gaussian-type orbitals, explaining their mathematical formulations and applications in quantum chemistry.

In Chapter 3, we comprehensively review spectroscopy and electronic transitions, as these concepts are intrinsically related to the underlying phenomena of absorption and emission processes. Chapter 4 of the thesis examines the phenomena of absorption and emission in organic compounds, focusing on fluorescence. It describes how materials absorb light energy and re-emit it at longer wavelengths, detailing the factors affecting fluorescence intensity. The chapter also delves into the quantum theory of photons, the principles of electromagnetic radiation, and the role of molecular structure in light absorption. Additionally, it highlights the Franck-Condon principle and the effect of conjugation on absorption properties.

Chapter 5 details the experimental apparatus employed to perform absorption, emission, and lifetime measurements to characterize the sample properly. In Chapter 6, we review the quantum mechanics methods used in the simulation of chemical systems, covering electronic structure calculations and molecular spectroscopy. We address the Hartree-Fock method and Density Functional Theory, commonly used in calculating chemical systems.

Chapter 7 presents the results obtained from the study of the absorption and emission of the py-res in various solvents. We discuss the properties related to temperature effects and lifetime in different solvents. Furthermore, we present the simulation results concerning the molecule of interest based on Time-dependent density-functional theory (TDDFT) methods.

Chapter 8 presents the results for absorption spectra of monocarbonyl curcumin, *(1E,4E)-1,5-bis(4-(dimethylamino)phenyl)penta-1,4-dien-3-ona*, in various solvents at room temperature. Emission spectra were recorded at excitation wavelengths of 405, 450, 488, and 532 nm, with the results supporting the Kasha-Vavilov rule, except for toluene. A significant Stokes shift was observed, particularly in methanol. Computational simulations using B3LYP and $6-31+G(d,p)$ basis set provided insight into the molecule's geometry, charge density, and HOMO–LUMO transitions, with calculated absorption peaks closely aligning with experimental data. The emission spectra were further analyzed through spectral deconvolution and fluorescence lifetime measurements, revealing solvent-dependent behaviors.

Chapter 9 examines the optical properties of the synthesized chalconoid, *(E)-1-(4-aminophenyl)-3-(4-(dimethylamino)phenyl)prop-2-en-1-one*, through UV–vis absorption and fluorescence spectroscopy in various solvents. The compound displays notable solubility and spectroscopic behavior in solvents such as heptane, toluene, dichloromethane, ethyl acetate, and acetonitrile. Computational analysis using TDDFT and CAM-B3LYP, in conjunction with State-Specific PCM calculations, provided insights into the molecular orbitals and energy transitions, with experimental results validating the predicted absorption and emission energies. Additionally, a

pronounced Stokes shift was observed, particularly in nonpolar solvents like heptane and toluene. These findings highlight the significant influence of solvent polarity on the optical properties of the chalconoid.

# MOLECULAR ORBITAL THEORY

J J Thomson's discoveries in 1897 led him to propose the "plum pudding" model to describe the structure of an atom [46]. In 1904, the Japanese physicist Hantaro Nagaoka proposed an alternative planetary model for the atom, in which a positively charged center is surrounded by a number of revolving electrons, similar to Saturn and its rings [47].

Nagaoka's model made two predictions: a massive atomic center and electrons orbiting the nucleus, bound by electrostatic forces. Ernest Rutherford successfully confirmed both predictions and mentioned Nagaoka's model in his 1911 paper that proposed the atomic nucleus [48].

In 1909, Ernest Rutherford found that most atomic mass was condensed in a positively charged nucleus. His analyses showed that the plum pudding model could not explain the atomic structure. In 1913, Niels Bohr, Rutherford's postdoctoral student, proposed a new atomic model where electrons orbited the nucleus with classical periods but could only have discrete angular momentum values, quantized in units of $\hbar$ [49]. This restriction allowed only specific electron energies. Bohr's atomic model resolved the energy loss problem by radiation from a ground state and explained the origin of hydrogen's spectral emission lines.

The American chemist Robert S. Mulliken pioneered the development of Molecular Orbital Theory. In 1932, aiming to describe and understand molecules in terms of one-electron wave functions, he was the first to use the term "orbital" as an abbreviation for a one-electron wave function [50, 51].

## 2.1 ATOMIC ORBITAL

An atomic orbital describes the probability of finding an electron in a specific region around the atom's nucleus [52–54]. Each orbital in an atom is characterized by a set of values, $n$, $\ell$, and $m_\ell$, which correspond, respectively, to the electron's energy level (principal quantum number), orbital angular momentum, and the projection of the orbital angular momentum along a chosen axis (magnetic quantum number).

An orbital can accommodate a maximum of two electrons, each with its spin projection $m_s$. The $\mathbf{s}$, $\mathbf{p}$, $\mathbf{d}$, and $\mathbf{f}$ orbitals, for example, refer to orbitals with $\ell = 0, 1, 2$, and $3$, respectively. These descriptions, along with the value of $n$, are used to describe the electronic configurations of atoms.

We can define atomic orbitals as approximate solutions to the Schrödinger equation for

electrons bound to the atom by the nucleus's electric field. Specifically, we approximate the state of an atom by an expansion in linear combinations of antisymmetrized products - the Slater determinants, detailed in section 6.2 - of one-electron functions. We call the spatial components of these one-electron functions atomic orbitals [55, 56]. When considering the spin component, we refer to atomic spin orbitals [57].

The concept of an atomic orbital is fundamental for visualizing the excitation process associated with a particular transition. For example, one can describe a given transition as the excitation of an electron from an occupied orbital to an unoccupied orbital, considering the restrictions imposed by the Pauli exclusion principle[1] [58].

In summary, an atomic orbital as a one-electron wave function is an approximation for describing electronic behavior. Exploring the atomic orbital theory, we associate the orbital with the Hartree-Fock approximation, which reduces the complexities of molecular orbital theory [59, 60]. We will address the Hartree-Fock method in detail in section 6.2.

## 2.2 TYPES OF ORBITALS

When working with spherical coordinates to describe an orbital, we obtain the product of three factors: $\psi(r, \theta, \varphi) = R(r)\Theta(\theta)\Phi(\varphi)$. The angular terms of atomic orbitals $\Theta(\theta)\Phi(\varphi)$ generate **s**, **p**, **d**, and **f** functions, for example, as real combinations of spherical harmonics $Y_{\ell m}(\theta, \varphi)$ [61]. Usually, three mathematical approaches are used to describe the radial functions $R(r)$, which can be chosen as a starting point for calculating the properties of atoms and molecules with many electrons.

### HYDROGEN-LIKE ORBITALS

The nomenclature "hydrogen-like atom" is for any atom or ion with a sole valence electron, considered isoelectronic with hydrogen.[62] Since hydrogen-like atoms are two-particle systems with an interaction that depends only on the distance between these particles, the (non-relativistic) Schrödinger equation can be solved analytically. The solutions are one-electron functions and are called hydrogen-like atomic orbitals [63].

Hydrogen-like atomic orbitals are eigenfunctions of the one-electron angular momentum operator $L$, and its $z$ component, $L_z$, and the eigenvalues depend only on the principal quantum number $n$. Consequently, to describe a hydrogen-like atomic orbital, we need no more than the following values: $n$, $\ell$, and $m_\ell$. The spin quantum number $m_s = \pm 1/2$ must also be added following the Aufbau principle[2] [63, 64]. This principle restricts the allowed values of the four

---

[1]The Pauli Exclusion Principle states that no two identical fermions, such as electrons, can occupy the same quantum state simultaneously in a system.

[2]The principle concerns the hypothetical process of constructing an atom's electronic distribution. As electrons

quantum numbers in electronic configurations of atoms with more electrons. In hydrogen-like atoms, all degenerate orbitals[3] for fixed $n$ and $L$, with varying $L_z$ and $s$, form an atomic shell.

## SLATER-TYPE ORBITALS

Slater-type orbitals (STOs), also called Slater orbitals, are functions used as atomic orbitals. They are named after physicist John C. Slater, who introduced them in 1930 [65]. STOs are primarily used to calculate wave functions for atomic and diatomic systems. This method is popular in computational chemistry in *ab initio* methods.

STOs have the following radial parts:

$$R(r) = N r^{n-1} e^{-\zeta r} \tag{2.1}$$

where $n$ is the principal quantum number; in particular, we have $n = 1, 2, \ldots$; $N$ is a normalization constant; $r$ is the distance of the electron from the atomic nucleus, and $\zeta$ is a constant related to the effective nuclear charge.

We calculate the normalization constant from the integral [65, 66]:

$$\int_0^\infty x^n e^{-\alpha x} \, \mathrm{d}x = \frac{n!}{\alpha^{n+1}}. \tag{2.2}$$

Therefore,

$$N^2 \int_0^\infty \left( r^{n-1} e^{-\zeta r} \right)^2 r^2 \, \mathrm{d}r = 1 \implies N = (2\zeta)^n \sqrt{\frac{2\zeta}{(2n)!}}. \tag{2.3}$$

We commonly use spherical harmonics $Y_l^m(\mathbf{r})$, depending on the polar coordinates of the position vector $\mathbf{r}$, as the angular part of the Slater orbital.

## GAUSSIAN-TYPE ORBITALS

In quantum chemistry, we use Gaussian-type orbitals (GTOs) as atomic orbitals in linear combinations forming molecular orbitals [67]. GTOs serve as the basis functions in most quantum chemistry software packages. Replacing Slater functions (STOs) with Gaussian basis functions (GTOs) increases efficiency because the product of two Gaussians at different points in space equals a Gaussian centered along the axis connecting them, making three- and four-index

---

are progressively added, they assume the most stable conditions concerning the nucleus and the already present electrons. According to the principle, electrons fill orbitals starting from the lowest available energy states before filling higher states. The Pauli exclusion principle limits the number of electrons occupying each orbital.

[3]Electronic orbitals with the same energy levels are called degenerate orbitals. According to the Aufbau principle, the lowest energy levels are filled before the higher energy levels. Therefore, according to Hund's rule, degenerate orbitals are equally filled before electrons are inserted into higher energy levels.

integrals easily reducible to two-index integrals [68]. We write a GTO as [68]:

$$\varphi_{\ell_x,\ell_y,\ell_z,\zeta}(x,y,z) = \left(\frac{2\zeta}{\pi}\right)^{\frac{3}{4}} \left[\frac{\ell_x!\ell_y!\ell_z!(8\zeta)^{\ell_x+\ell_y+\ell_z}}{(2\ell_x)!\,(2\ell_y)!\,(2\ell_z)!}\right]^{\frac{1}{2}} x^{\ell_x}y^{\ell_y}z^{\ell_z}e^{-\zeta\left(x^2+y^2+z^2\right)}, \qquad (2.4)$$

where $\zeta$ is a parameter that controls the width of the Gaussian describing the orbital, and $\ell_x, \ell_y$, and $\ell_z$ are non-negative integers indicating the nature of the orbital [68].

Specifically, when $\ell_x = \ell_y = \ell_z = 0$, the orbital is spherically symmetric, i.e., of type $s$. When $\ell_x + \ell_y + \ell_z = 1$, there are three $p$-type orbitals ($p_x, p_y$, or $p_z$). For $\ell_x + \ell_y + \ell_z = 2$, the functions are of type $d$. In Cartesian coordinates, six possible factors can appear in 2.4 multiplying the Gaussian: $x^2, y^2, z^2, xy, xz$, and $yz$ [68]. Figure 4 presents a diagram of the spatial distribution of $s$, $p$, and $d$ type orbitals.

**Figure 4** – *Atomic orbitals of types s, p, and d. The red and blue regions indicate positive and negative phases (angle $\phi$ of the spherical harmonic corresponding to the orbital), respectively.*
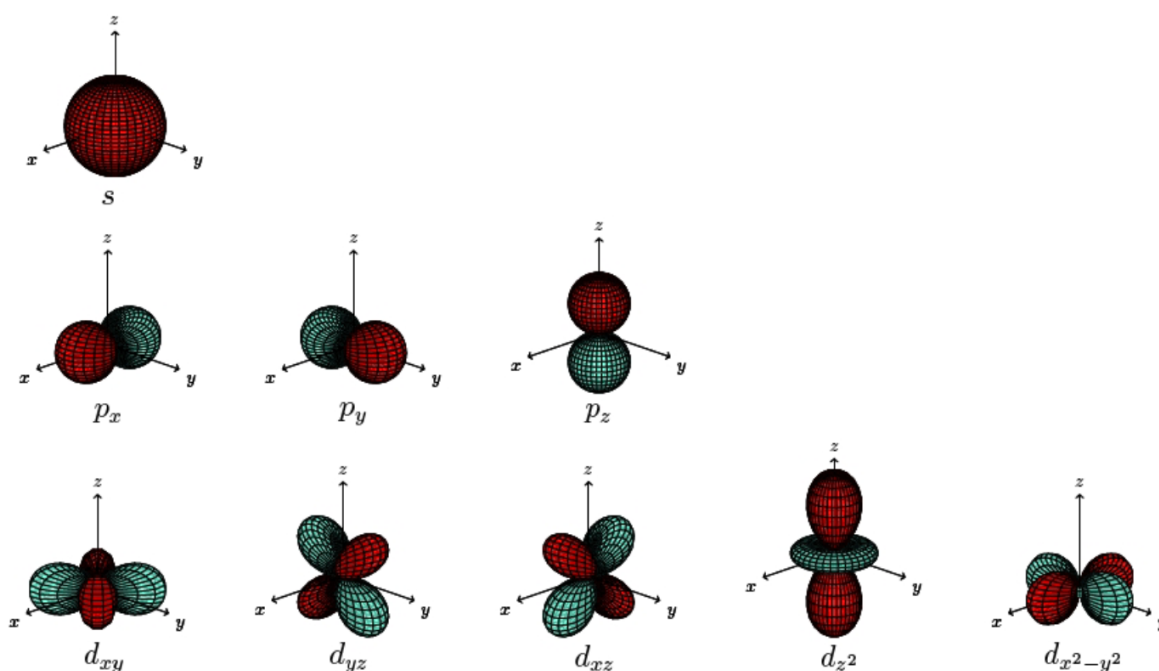


*Manzoni, 2010 [68].*

## 2.3 MOLECULAR ORBITAL THEORY

Molecular orbital theory constitutes a fundamental element in quantum chemistry that elucidates the electronic structure of molecules. Originating in the early 20th century, this theory

marks a significant transition from conventional atomic bonding models to a perspective based on quantum mechanics. Essentially, this theory advances with the premise that electrons in a molecule are not restricted to specific atomic bonds. Instead, it suggests that electrons are delocalized, influenced by all atomic nuclei.

For most covalent molecules, we can sketch the Lewis structure[4], describe the molecular geometry, and approximate the prediction of bond angles. However, one of the most significant known molecules, the oxygen molecule $O_2$, presents an inconsistency with the description from the Lewis structure. The representation has a double bond $O = O$, with each oxygen atom surrounded by eight electrons. However, this structure conflicts with the paramagnetic nature of dioxygen, a characteristic of molecules that have unpaired electrons. The Lewis structure of $O_2$ thus suggests that all electrons pair up.

Molecular orbital theory (MO theory) explains chemical bonding, addressing, among other phenomena, the paramagnetism of the oxygen molecule. Additionally, this theory clarifies the bonds in other molecules, such as those that violate the octet rule, and molecules with more complex bonds, which are difficult to describe using Lewis structures. Furthermore, MO theory provides a framework for characterizing the energies of electrons in a molecule and the possible location of these electrons. In contrast to valence bond theory, which uses hybrid orbitals attributed to specific atoms, MO theory employs the combination of atomic orbitals to generate molecular orbitals that are dispersed throughout the molecule rather than being located on its constituent atoms [69, 70].

Molecular orbital theory describes the distribution of electrons in molecules similarly to the distribution of electrons in atoms, using atomic orbitals. In this theory, we describe the behavior of an electron in a molecule by a wave function, $\psi$, similar to the behavior of an electron in an atom. Just as electrons around isolated atoms are confined to discrete energies, electrons around atoms in molecules are confined to discrete energies. We call the region of space with the highest probability of electron occupation in a molecule a molecular orbital ($\psi^2$) [69, 70]. Similarly to an atomic orbital, a molecular orbital is filled when it contains two electrons with opposite spins.

### 2.3.1 COMBINATION OF ATOMIC ORBITALS

We call the mathematical process of combining atomic orbitals to generate molecular orbitals the linear combination of atomic orbitals. The wave function describes the wave properties of an electron. Molecular orbitals are combinations of the wave functions of atomic orbitals. The combination of waves can lead to constructive or destructive interference – peaks align with valleys. In orbitals, the waves are three-dimensional, and they combine with in-phase waves, producing regions with a higher probability of electron density, and out-of-phase waves produce

---

[4]In the Lewis structure, valence electrons are represented as dots around the symbols of atoms. Chemical bonds are shown through the sharing of pairs of electrons between atoms, represented by a line.

nodes.

**Figure 5** – *Sigma ($\sigma$) and sigma-star ($\sigma^*$) molecular orbitals are formed by the combination of two atomic s orbitals.*

(a)

(b)

σ bonding molecular orbital        σ* antibonding molecular orbital
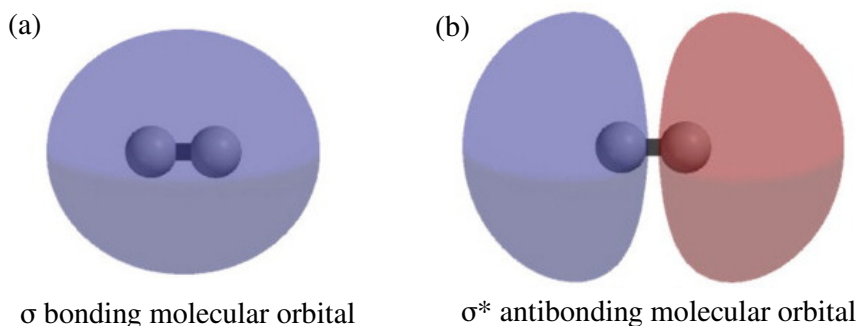
*Angarov, 2018 (Adapted) [71].*

Two molecular orbitals can form from overlapping two atomic $s$ orbitals in adjacent atoms [70]. Figure 5 illustrates the two types. The in-phase combination produces a lower-energy $\sigma_s$ molecular orbital, known as the bonding orbital, with the greatest electron density between the nuclei. The out-of-phase addition creates a higher-energy $\sigma_s^*$ molecular orbital [70]. The asterisk indicates that the orbital is an antibonding orbital. Electrons in a $\sigma_s$ orbital are attracted by both nuclei simultaneously and are more stable than in isolated atoms. Electrons fill the lower-energy $\sigma_s$ orbital before the higher-energy $\sigma_s^*$ orbital, just as they fill lower-energy atomic orbitals before filling higher-energy atomic orbitals.

In $p$ orbitals, the wave function originates two lobes with opposite phases. We indicate the phases by coloring the orbital lobes in different colors, as illustrated in Figure 6 [70]. When lobes of the same phase overlap, wave interference increases the electron density. Conversely, wave interference decreases electron density and creates nodes when regions of opposite phases overlap. When $p$ orbitals overlap, they produce $\sigma$ and $\sigma^\star$ orbitals, as shown in Figure 6. For instance, if two atoms are located along the $x$ axis in a Cartesian coordinate system, the two $p_x$ orbitals overlap and form $\sigma_{px}$, a bonding orbital, and $\sigma_{px}^*$, an antibonding orbital.

**Figure 6** – *Combination of two p atomic orbitals creating $(\sigma_p)$ and $(\sigma_p^*)$ orbitals.*
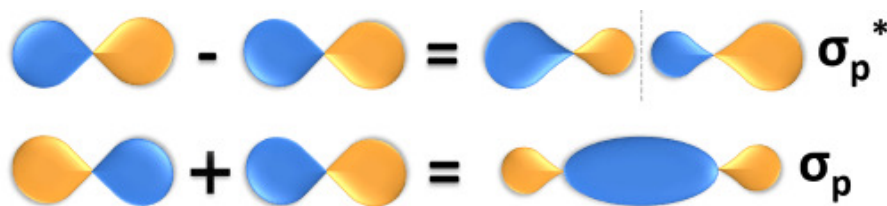
*Gates, 2019 [72] (Adapted).*

The overlap of two $p$ orbitals results in the formation of two $\pi$ molecular orbitals when oriented, as shown in Figure 7 [70, 73]. An antibonding molecular orbital with two nodes is obtained when out-of-phase orbitals are combined, as depicted in Figure 7 (a). One node contains the internuclear axis, and the other is perpendicular to the axis. On the other hand, a bonding orbital results in-phase orbitals are combined, as shown in Figure 7 (b).

**Figure 7** – *Combination of two $p$ atomic orbitals that can result in (a) $\pi_p$ and (b) $\pi_p^*$ orbitals.*
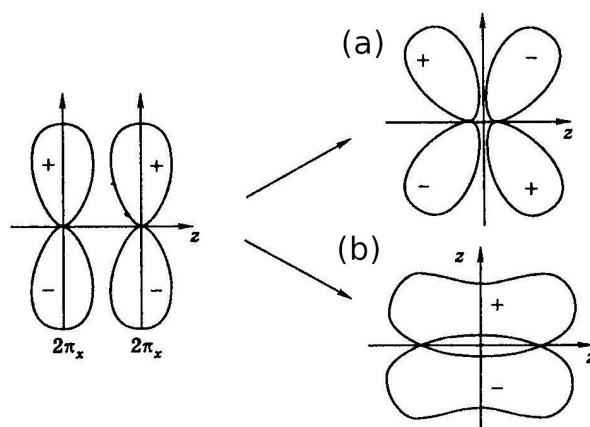


*Moscow Region State University, 2019 (Adapted) [73].*

In the molecular orbitals of diatomic molecules, each atom has two sets of $p$ orbitals oriented side by side ($p_y$ and $p_z$). These four atomic orbitals combine in pairs to create two $\pi$ and two $\pi^*$ orbitals [74]. The $\pi_{py}$ and $\pi_{py}^*$ orbitals are oriented at right angles to the $\pi_{pz}$ and $\pi_{pz}^*$ orbitals. Except for their orientation, the $\pi_{py}$ and $\pi_{pz}$ orbitals are identical and have the same energy, making them degenerate orbitals. The antibonding $\pi_{py}^*$ and $\pi_{pz}^*$ orbitals are also identical except for their orientation. The combination of the six $p$ atomic orbitals in two atoms produces a total of six molecular orbitals: $\sigma_{px}$ and $\sigma_{px}^*$, $\pi_{py}$ and $\pi_{py}^*$, $\pi_{pz}$ and $\pi_{pz}^*$. Figure 8 provides an example of fluorine fluoride.

Within the framework of molecular orbital theory, we analyze the distribution of electrons in molecules by considering the overlap and combination of atomic orbitals. This analysis is crucial for understanding the content addressed in the next chapter, which deals with electronic transitions.

**Figure 8** – *Molecular orbital diagram for $F_2$. Note that the $\pi$-type MOs formed by combining $p_x$ and $p_y$ orbitals form degenerate sets. The highest occupied molecular orbitals are the $1\pi_g$ orbitals, and the lowest unoccupied molecular orbital is the $3\sigma_u$ orbital.*
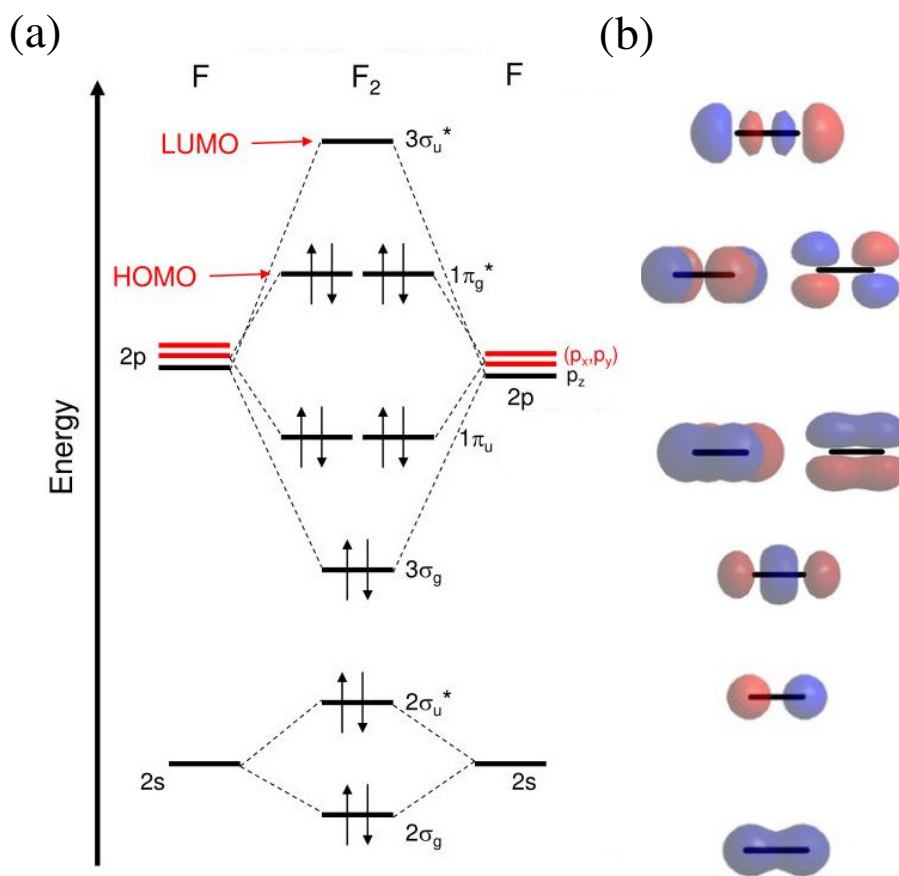


*Eames, 2014 (Adapted) [74].*

# SPECTROSCOPY AND ELECTRONIC TRANSITIONS

$S$ PECTROSCOPY uses electronic transitions to provide information about the structure and properties of matter [75]. Analyzing electronic transitions is fundamental for interpreting absorption and emission spectra, providing valuable material information. Furthermore, the chemistry of organic compounds is governed by the electrons in their molecules. Knowledge about the interaction of electrons with light is essential, as it allows understanding of the absorption and emission processes of energy in the form of electromagnetic radiation. Electronic transitions involve the transfer of electrons between atomic or molecular orbitals. These processes are responsible for various organic compounds' color, fluorescence, and optical properties.

## 3.1 ELECTRONIC TRANSITIONS

Changes in the energy of the involved electrons accompany electronic transitions. When an electron absorbs a photon, a transition to a higher-energy orbital occurs, denoted as an exciting transition. When an electron in a higher-energy orbital returns to a lower-energy orbital, it emits a photon. We call this transition a relaxed transition.

### 3.1.1 HOMO-LUMO ENERGY GAP

The HOMO-LUMO energy gap is the energy difference between the highest occupied molecular orbital (HOMO) and the lowest unoccupied molecular orbital (LUMO) in a molecule. The HOMO-LUMO energy gap is essential in describing a molecule's electronic and optical properties.

The HOMO-LUMO energy gap determines the molecule's ability to absorb photons and transfer electrons. Light absorption occurs when a photon with energy equal to or greater than the HOMO-LUMO energy gap is absorbed by a molecule, resulting in an excited electronic transition.

In the case of molecular hydrogen, between the $\sigma$ orbital (HOMO) and the $\sigma^*$ orbital (LUMO). The $\sigma$ orbital is filled with electrons, while the $\sigma^*$ orbital is empty, as schematized in Figure 9. When a photon with a specific energy is absorbed, an electron is excited from the $\sigma$ orbital to the $\sigma^*$ orbital, creating an excited state. We call this transition a $\sigma$ - $\sigma^*$ transition, and it is possible because the photon energy corresponds to the energy difference between the HOMO and the

LUMO. The excited electron in the LUMO is less stable than in the HOMO. It tends to relax to the ground state, returning from the $\sigma^*$ orbital to the $\sigma$ orbital and releasing the absorbed energy as a photon.

**Figure 9** – *The electronic transition of hydrogen has an energy variation $\Delta E$ of 258 kcal/mol, which corresponds to light with a wavelength of 111 nm.*
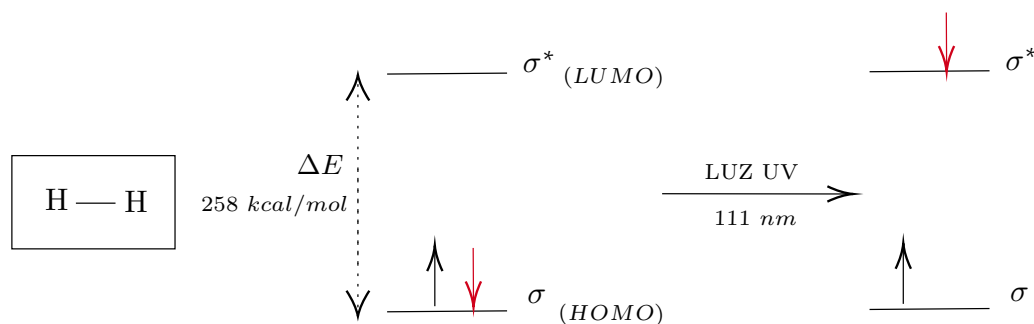


*Author, 2023.*

When a molecule with a double bond, such as ethene, absorbs light, it undergoes a $\pi - \pi^*$ electronic transition. Unlike the $\sigma - \sigma^*$ transition, the $\pi - \pi^*$ energy gap is narrower, meaning the energy required to excite an electron is lower. This mechanism causes ethene to absorb light at a longer wavelength than molecular hydrogen - around 165 nm.

The $\pi - \pi^*$ transition is possible because the double bond in ethene has two $\pi$ orbitals. When a photon with sufficient energy is absorbed, it excites an electron from the $\pi$ orbital to the $\pi^*$ orbital, creating an excited state. The photon's energy must match the energy difference between the HOMO and the LUMO.

As in the case of molecular hydrogen, the excited electron in the LUMO of ethene is less stable than in the HOMO and tends to relax to the ground state, returning from the $\pi^*$ orbital to the $\pi$ orbital and releasing the absorbed energy as a photon. This process, known as emission, is responsible for the light emitted by certain fluorescent materials, including some dyes and organic compounds.

Thus, the HOMO-LUMO energy gap in the $\pi - \pi^*$ transition is smaller in conjugated chains. Because the energy required to excite electrons is lower, the absorbed light has a longer wavelength.

In the case of 1,3-butadiene, a molecule with four carbon atoms in a chain, there are four available 2pz atomic orbitals for forming molecular orbitals, as shown in image 10. The bottom two orbitals form bonds, while the top two form antibonds. When we compare this molecular

orbital representation to ethene, an example of an isolated $\pi$ bonding, we observe that the energy gap between the HOMO and the LUMO is smaller for the conjugated system.

**Figure 10** – *The 1,3-butadiene absorbs UV light with a wavelength of 217 nm. We see that the HOMO-LUMO energy gap is indeed smaller for the conjugated system.*
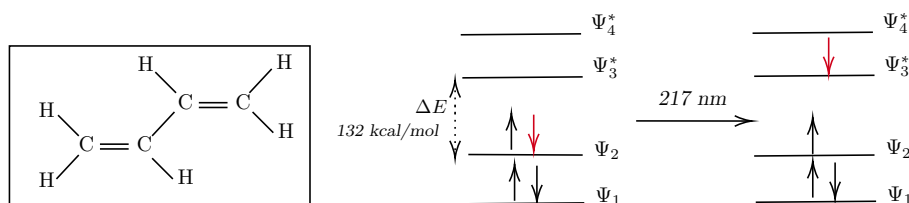


*Author, 2023.*

Chromophores are functional groups or parts of a molecule responsible for absorbing light at a specific wavelength. These groups absorb light when an electron is promoted from the HOMO to the LUMO. We will thus study chromophores in more detail.

### 3.1.2 CHROMOPHORES

Chromophores are functional groups responsible for the color of organic compounds. They can absorb visible light photons, resulting in excited electronic transitions. Physical equations govern the absorption of light by chromophores, describing the phenomenon. In this section, we will explore chromophores and the physical equations that describe them [30].

### 3.1.2.1 Functional Groups and Properties of Visible Light Absorption

Chromophores are functional groups with $\pi$ or non-bonding electrons in their structure. These electrons can absorb visible light photons, resulting in excited electronic transitions. These functional groups have unique light absorption properties, making them useful as indicators for different chemical reactions and biological processes. Additionally, the presence of chromophores in organic compounds can affect their physical and chemical properties, such as solubility, reactivity, and stability [76–78].

Among the most common chromophores, the nitro group ($NO_2$) stands out, with its high dipole moment allowing it to interact with other molecules through hydrogen bonding and dipole-dipole forces. The carbonyl group ($C = O$), found in compounds such as ketones, aldehydes, and carboxylic acids, shows intense absorption in the electromagnetic spectrum region corresponding to visible light.

Other important chromophores include the azo group ($-N = N-$), which is frequently used as a dye in paints and fabrics; the azomethine group ($-N = N - C-$), which is found in compounds like azo dyes and luminescent materials; and the azide group ($-N = N - N = N-$), which shows intense absorption in the visible light region of the electromagnetic spectrum and is used as a dye in various applications.

Besides these functional groups, chromophores can also include aromatic groups such as benzene ($C_6H_6$) and naphthalene ($C_{10}H_8$), which exhibit intense absorption in the visible light region of the electromagnetic spectrum and are often used as dyes and indicators.

## 3.2 SPECTROSCOPY

Spectroscopy is a technique used to study the interaction of light with matter. It allows the analysis of light absorbed, transmitted, or reflected by materials at different wavelengths. By analyzing these spectra, one can determine information about the chemical composition and properties of materials, such as molecular structure and optical properties.

### 3.2.1 APPLICATIONS OF SPECTROSCOPY IN THE ANALYSIS OF MOLECULAR PROPERTIES

Scientists widely use spectroscopy in various fields, from the analysis of chemical compounds to astrophysics [79]. The study of electronic transitions is crucial for interpreting absorption and emission spectra, which provide valuable information about the structure and properties of matter.

Infrared spectroscopy is a vibrational analysis technique that provides information about the molecular properties of materials. In infrared spectroscopy, vibrating atoms in a molecule absorb energy from infrared radiation, leading to changes in the molecules' energy levels.

Molecules exhibit different vibrational modes corresponding to different infrared spectrum frequencies. These vibrational modes can be divided into two main types: stretching and bending modes.

Symmetric and asymmetric stretching are two distinct vibrational modes that differ in how the atoms in a molecule move relative to each other. Symmetric stretching preserves the geometry of the molecule, while asymmetric stretching results in changes in the molecular geometry [80], as illustrated in Figure 11.

Bending vibration is another type of vibrational mode that occurs in polyatomic molecules. Unlike stretching vibrations, which involve changes in the distances between the atoms of a chemical bond, bending vibrations refer to changes in the angles between chemical bonds [80].

In bending vibrations, the atoms move in a pattern that causes the angle between the chemical bonds to increase or decrease. These movements can occur in different planes and directions and sometimes combine with stretching movements. Different bending vibrations include in-plane

**Figure 11** – *Stretching vibrational modes.*



Stretching

Symmetric Stretch    Asymmetric Stretch
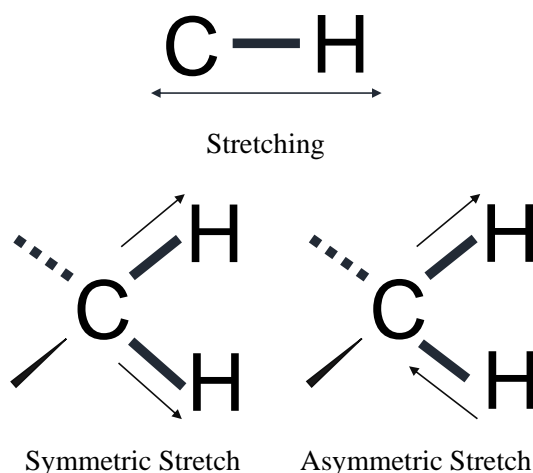
*Author, 2023.*

**Figure 12** – *Bending vibrational modes.*



in-plane rocking    in-plane scissoring    out-of-plane wagging    out-of-plane twisting
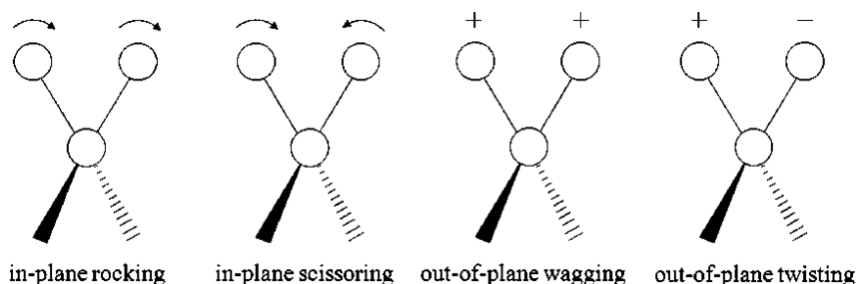
*Ojeda, Jesús & Dittrich, Maria, 2012 [81].*

bending, where the atoms move in the same plane as the chemical bonds. A typical example is angular vibration, where two atoms bonded to a central atom move in opposite directions in the same plane, causing the angle between the chemical bonds to increase or decrease, and out-of-plane bending, where the movement of the atoms happens outside the plane of the chemical bonds. An example is torsional vibration, where the atoms move in opposite directions in different planes, resulting in a change in the angle between the chemical bonds and a rotation of the molecule.

### 3.2.2 UV-VIS SPECTROSCOPY

UV-VIS spectroscopy is a widely used analytical technique for determining light absorption in organic and inorganic compounds. This technique is based on the electrons present in the compounds absorbing ultraviolet (UV) and visible (VIS) light.

The absorption of UV-VIS radiation is directly proportional to the number of electrons present in the molecule, and the absorption intensity is influenced by the wavelength of the radiation and the concentration of the sample.

The Beer-Lambert law, which relates light absorption to the concentration of the sample, is [30]:

$$A = \epsilon l c \tag{3.1}$$

where $A$ is the absorption, $\epsilon$ is the molar extinction coefficient, $l$ is the optical path length of the sample, and $c$ is the concentration of the sample.

Using the Beer-Lambert law, we can determine a sample's unknown concentration from its measured absorbance. Additionally, we can use UV-VIS spectroscopy to determine a sample's purity by comparing its measured absorbance with the theoretical absorbance of a pure substance.

UV-VIS spectroscopy is also helpful for identifying functional groups present in organic compounds. Functional groups, such as double bonds or aromatic rings, can lead to characteristic absorptions at specific wavelengths.

We can describe the energy of UV-VIS radiation absorbed by the electrons in compounds using Planck's equation:

$$E = h\nu \tag{3.2}$$

where $E$ is the energy of the radiation, $h$ is Planck's constant, and $\nu$ is the frequency of the radiation.

Using Planck's equation, we can determine the energy of the electrons in compounds from the absorbed wavelengths. This information can help us determine the electronic structure of the compounds and better understand the optical properties of the materials.

### 3.2.3 ABSORPTION IN SPECTROSCOPY

We use transmittance and absorbance in spectroscopy to describe the interaction of light with a sample. Transmittance is the fraction of incident light that passes through the sample, meaning the amount of light not absorbed by the sample. It is often expressed as a percentage or a value between 0 and 1 [58, 82].

The absorption spectrum is the graphical representation of the amount of light absorbed by a substance as a function of the radiation's energy. We obtain this spectrum by measuring the transmittance or absorbance of light at a series of wavelengths. We define absorbance as:

$$A = -\log_{10}(T) \tag{3.3}$$

where $T$ is the transmittance, the fraction of incident light passing through the sample. We can interpret the absorption spectrum regarding allowed electronic transitions between different energy states in molecules and atoms.

Absorbance is directly proportional to the concentration of the sample and the optical path length of light through the sample. Therefore, the higher the sample concentration or the optical path length, the greater the absorbance. We frequently use absorbance in spectroscopy due to its linearity with sample concentration, allowing us to quantify the amount of a substance in a solution. On the other hand, we use transmittance to evaluate the sample's quality and the efficiency of the absorbance measurement, as very low transmittance values may indicate that the sample is too thick or contains particles that interfere with the measurement.

The absorption spectrum is an essential tool in chemistry, biochemistry, and physics for identifying substances, quantifying solution concentrations, determining oxidation states, and studying chemical reactions. We also use the absorption spectrum to analyze substance mixtures, allowing the identification and quantification of each component in a mixture. Furthermore, we use the absorption spectrum to study the properties of molecules and atoms in gases, liquids, and solids, providing information about the energies of electronic, rotational, and vibrational states.

# ABSORPTION AND EMISSION OF ORGANIC COMPOUNDS

F LUORESCENCE is a physical phenomenon that occurs when a material absorbs energy from a light source and emits it at a longer wavelength. This excitation happens when the material's electrons absorb the incident light energy, causing them to transition to higher energy levels. This absorbed energy is emitted as light when the electrons relax back to their original levels [30].

The intensity and wavelength of the emitted light in fluorescence depend on the material's properties, including its electronic and molecular structure. Additionally, the intensity of fluorescence can be affected by various factors, including the concentration of the material, temperature, and the presence of quenchers[1].

In addition to the above, it is crucial to emphasize that studies related to the photon theory proposed by Einstein have proven relevant in understanding the behavior of light under other circumstances. For instance, this theory explains how light can interact with matter, producing effects of singular importance, such as fluorescence and phosphorescence. Understanding these phenomena has been vital in various fields of science, from investigating the structure of molecules [83] to the development of new materials and technologies [84–88].

To deepen the understanding of the fluorescence phenomenon, it becomes essential to possess a solid and comprehensive knowledge of concepts related to light absorption. This concept is crucial for elucidating the underlying mechanisms governing fluorescence.

## 4.1 ABSORPTION

In 1865, as previously discussed in this work, James Clerk Maxwell developed the dynamic theory of the electromagnetic field, in which he demonstrated that light corresponds to transverse electromagnetic waves whose vibration frequency ($\nu$) and wavelength ($\lambda$) are related by $\nu\lambda = \upsilon$, where $\upsilon$ is the propagation speed in the medium. When an electromagnetic wave passes through a medium, it can undergo absorption, which means that part of the wave's energy is transferred

---

[1]In physics and chemistry, a quencher is a substance or molecule that reduces the fluorescence or luminescence of another substance or molecule, usually through an energy transfer process. Examples of quenchers include metal ions (such as ferrous ion ($Fe^{2+}$) and copper ion ($Cu^{2+}$)); organic quenchers, such as aromatic amine quenchers like acetamide and urea, and anthraquinone acid quenchers like 9,10-dicyanoanthracene; and inorganic compounds, such as ascorbic acid and sodium chloride.

to the medium and converted into another form of energy. Thus, the investigation of absorption has its initial milestones in concepts that pervade the electromagnetic description of light.

### 4.1.1 ELECTROMAGNETIC RADIATION

Like any other periodic phenomenon, electromagnetic radiation can be characterized by its amplitude, frequency ($\nu$), and phase ($\phi$). The frequency can be measured in waves per second. The number of waves per centimeter is the wavenumber, $\overline{\nu}$, related to the frequency ($\nu$) by the relation [22]:

$$\overline{\nu} = \frac{\nu}{c} \ ,$$ (4.1)

where $c$ is the speed of light in the medium through which the waves propagate. The wavelength is given by:

$$\lambda = \frac{1}{\overline{\nu}} \ .$$ (4.2)

While the frequency is independent of the propagation medium, the wavenumber and wavelength are not. The dependence of propagation speed on the medium gives rise to the phenomenon of dispersion, which is of fundamental importance in spectroscopy.

### 4.1.2 PHOTONS

According to the formalism of quantum mechanics, radiant energy is absorbed or emitted only in discrete quantities. The energy ($e$) of a photon is related to the wave frequency by Planck's relation:

$$e = h\nu = h\frac{c}{\lambda} = hc\overline{\nu} \ .$$ (4.3)

where $h$ is Planck's constant, equal to $6.62 \times 10^{-27}$ erg $\cdot$ s.

In photochemical applications, dealing with the energy transported by 1 mole of photons is often convenient, thus connecting the energy changes occurring in absorption and emission to the energy content per mole of the substance responsible for absorption or emission. The energy in 1 mole of photons is the Einstein (E)[2][89–91]:

$$E = Ne = Nh\frac{c}{\lambda} \ ,$$ (4.4)

with $N$ being Avogadro's number ($6.023 \times 10^{23}$).

---

[2]In photobiology, the Einstein unit is defined as the energy of one mole of photons. The Einstein is not part of the International System of Units (SI).

### 4.1.3 Light Absorption by Molecules

#### 4.1.3.1 General Considerations

For atoms in the gaseous state, electronic absorption bands are remarkably sharp [92], as exemplified in Figure 13. The linewidth is determined only by pressure and temperature and is generally $10^{-2} - 10^{-1}$ Å. The energy levels are distinctly separated, and the absorption states can be characterized entirely [93].

**Figure 13** – *Spectra for nitric oxide and sulfur dioxide.*
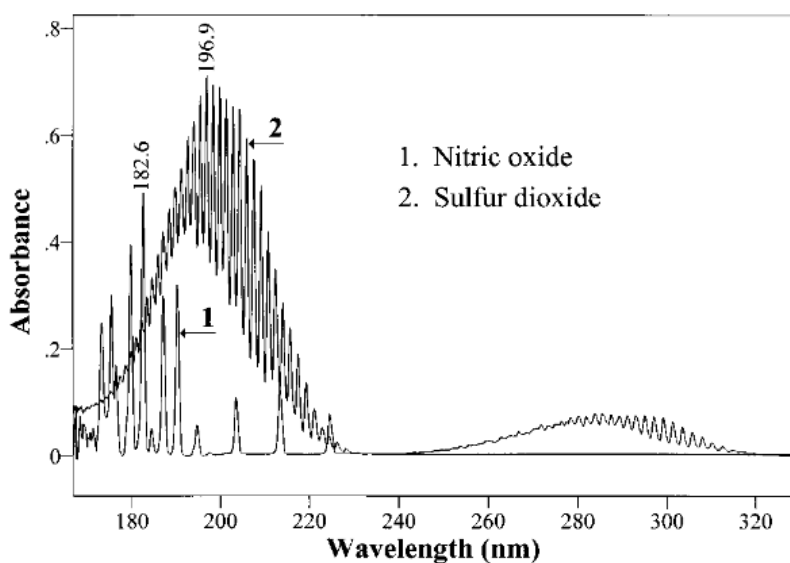


*Lagesson-Andrasko et al., 1998. [93].*

For molecules in solution, the situation is considerably more complicated. Instead of a single absorption line, a band is observed. The amplitude originates from electronic, vibrational, and rotational transitions that may occur [58]. To illustrate the principles involved, consider the case of a simple diatomic molecule. The potential energy, $E$, as a function of the internuclear distance, $r$, is given by the familiar Morse diagram, illustrated in Figure 14.

The minima in the energy level curves correspond to the equilibrium internuclear distance. $v_0$ is the zero-point energy; $v_1, v_2, ...$, each corresponds to the potential energies of the vibrational states that the molecule can assume. In an environment without incident electromagnetic radiation, thermal equilibrium produces a distribution of molecules among the levels following Boltzmann statistics [58, 94]. The number of molecules in the $N_j$-th level, compared to the number in the ground state, $N_0$, is given by:

$$\frac{N_j}{N_0} = \frac{P_j}{P_0} e^{\frac{-\Delta E}{kT}} \quad ,$$

(4.5)

where $\Delta E$ is the energy difference between the $j$-th and ground levels, $P_0$ and $P_j$ are the degeneracies of the ground and $j$-th states (i.e., the number of states with the same energy), and $k$ is Boltzmann's constant ($1.38 \times 10^{-16}$erg K$^{-1}$). The vibrational energy levels are typically separated by about $3$kcal mol$^{-1}$ so that at room temperature, only $0.1\%$ are found in levels above zero. For practical purposes and at room temperature, we can consider that light absorption originates from molecules in the lowest level of the ground state. The distribution along $r$ (internuclear separation) is characteristically different for molecules in the zero level than in other levels. The most probable distance for the zero level is $r_0$, the equilibrium internuclear distance. For $v > 1$, the distribution becomes bimodal or multimodal, with extreme values being the most significant. For a certain value, $r_d$, of $r$, the interaction becomes negligible, and the atoms can separate without further change in $v$. The energy difference between this state and $v = 0$ is the dissociation energy[3] $D$ of the molecule, which in turn determines the molecule's overall bond energy.

**Figure 14** – *Energy diagram for a diatomic molecule with potential energies of upper and lower states for two electronic levels.*
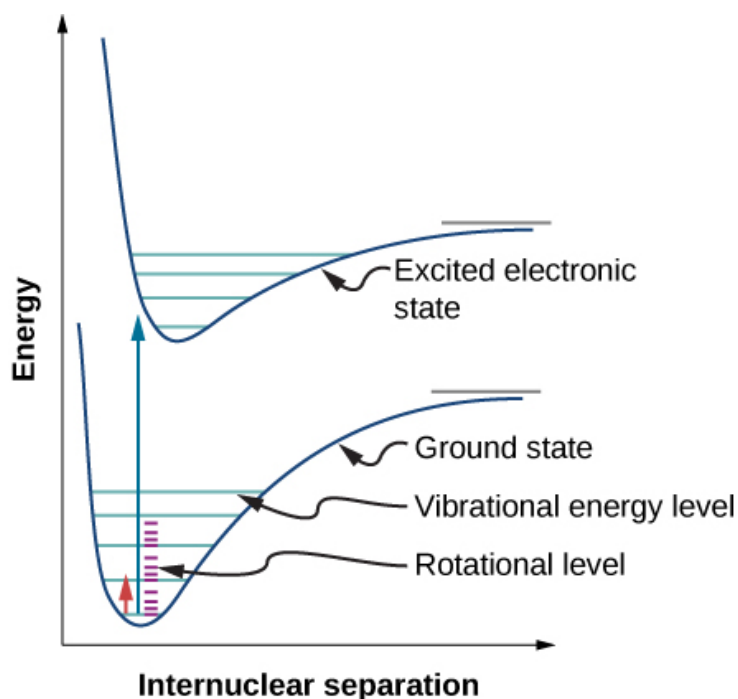


*Harilal et al. (Adapted), 2018. [95].*

---

[3]The dissociation energy of a molecule is a quantity that represents the minimum energy required to separate the atoms constituting a molecule and bring them to their isolated states. The dissociation energy measures the molecule's stability; the higher the dissociation energy, the stronger the chemical bond between the atoms.

### 4.1.3.2 Franck-Condon Principle

Absorption or emission in polyatomic molecules is governed by the Franck-Condon principle, formulated by James Franck and Edward Condon in 1926 [96]. In its simplest form, the principle states that changes in the electronic distribution occur rapidly compared to bond angles and lengths. Therefore, the nuclear configuration of a molecule, i.e., the set of bond distances and angles, cannot appreciably change during the process of light absorption or emission by the molecule.

In the simplest case of a diatomic molecule, the Franck-Condon principle means that an electronic transition can be represented by a vertical line starting at $r_0$ and ending in an excited state with that same value of $r$, as depicted in Figure 14. Since $r_0^* > r_0$, an excited vibrational level is almost always reached upon absorption.

The field can reach higher vibrational levels if it contains the necessary energy. Some molecules in the ground state have $r$ values greater or smaller than $r_0$, as there is a distribution of $r$ values in the molecules in the zero level of the ground state. Molecules in the ground state still possess vibrational energy, and thus, their internuclear distances are not constant. Due to this vibrational energy, the molecules are in constant motion, and their internuclear distances vary around the equilibrium position. Therefore, there is a distribution of $r$ values in the molecules in the zero level of the ground state [97].

Absorption bands with long tails instead of abrupt terminations can exist. In long-tailed bands, absorption is often considered thermally sensitive. In these bands, a decrease in temperature almost invariably results in a shift of the band edge to shorter wavelengths due to the reduction of the thermally excited population.

### 4.1.3.3 Effect of Conjugation on Absorption

A simplified way to consider light absorption by molecules containing conjugation involves molecular orbital theory, which uses a linear combination of atomic orbitals (LCAO) to represent molecular orbitals encompassing the entire molecule. The classification of these molecular orbitals includes bonding, antibonding, and non-bonding.

In most systems of interest, $\pi$-$\pi^*$ transitions are responsible for light absorption in the lower energy absorption regions (in some cases, $n$-$\pi^*$ transitions) [58]. Since $\pi$ bonds occur in double bonds, carbon-carbon, it follows that molecules with double bonds are of particular interest, especially when there is a system of alternating single and double bonds, which allows for the delocalization of $\pi$ electrons, or conjugation. As conjugation in a molecule increases, the energy of the $\pi$-$\pi^*$ transition decreases – which corresponds to a red shift (also known as bathochromic shift) in absorption [98], as illustrated in Figure 15. It is noted that absorption also intensifies

with the increase in conjugation. In the case of cis and trans isomers[4], the cis isomer generally absorbs at shorter wavelengths with a lower extinction coefficient than the trans isomer.

**Figure 15** – *The appearance of absorption peaks and dependence on conjugated systems.*
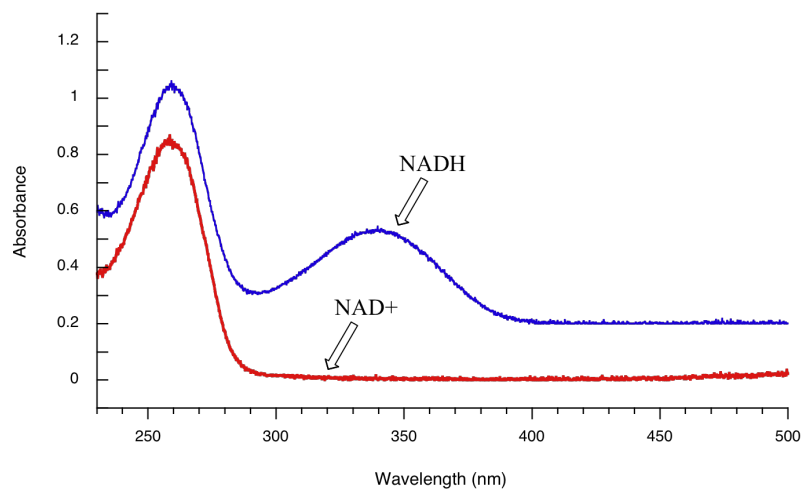


*LibreTexts Chemistry, 2014 [98].*

This conjugation also occurs in aromatic systems and, as discussed, the greater the extent of conjugation, the more significant the red shift of absorption and the higher the molar extinction coefficient [99]. In cases where the conjugated system, whether linear or aromatic, contains additional chemical groups, such as carbonyl groups, amide[5] or azo[6] groups, the absorption characteristics can be altered by two effects.

Firstly, the additional chemical group can be a chromophore (a concept that will be further explored in Chapter 3), thus increasing absorption at specific wavelengths. For example, a carbonyl group ($RHC = O$) will exhibit a maximum absorption around 290 nm with a molar extinction coefficient near 16 due to an $n–\pi^*$ transition. These transitions can appear as an elevated side bump in the main absorption band [80]. Secondly, the chemical group can affect the underlying absorption characteristic of the original molecule. The effect of these groups depends on whether they are electron donors or withdrawers [80]. These general considerations are helpful when examining a molecular structure and estimating the wavelength region in which it is likely to absorb light.

---

[4]Isomers are compounds with the same molecular formula but different spatial arrangements.

[5]An amide is a functional group found in organic molecules, such as proteins, starch, and DNA. It consists of a nitrogen atom bonded to two hydrogen atoms and a carbonyl group (-C=O), which is in turn bonded to another carbon atom in the molecule.

[6]Found in organic molecules, the azo group consists of two nitrogen atoms (N) joined by a double bond (N=N). This double bond is highly polar, conferring reactive properties and distinctive characteristics to the group.

### 4.1.4 BEER-LAMBERT EQUATION

The molecule's ability to absorb light at specific wavelengths can be considered in the context of the Beer-Lambert law, sometimes known as the Beer-Lambert-Bouguer law, to recognize the contributions of August Beer (a German physicist), Johann Heinrich Lambert (a Swiss astronomer), and Pierre Bouguer (a French astronomer).

The Beer-Lambert equation is a mathematical relationship that describes light absorption by a medium, such as a solution or gas. The equation is given by [100]:

$$I = I_0 e^{-\epsilon cl} \ , \tag{4.6}$$

where $I$ is the intensity of light emerging from the medium, $I_0$ is the initial intensity of light entering the medium, $c$ is the concentration of the solution, $l$ is the path length through the medium, and $\epsilon$ is the molar extinction coefficient of the solution at a specific wavelength.

In the context of fluorescence, the Beer-Lambert equation can be modified to account for the emission of light by the material, resulting in the modified Beer-Lambert equation [100]:

$$I = I_0 e^{-\epsilon cl} \phi(\lambda) \ , \tag{4.7}$$

where $\phi(\lambda)$ is the fluorescence quantum efficiency at a given wavelength.

Fluorescence quantum efficiency is the ratio of the number of photons emitted per unit time to the number of photons absorbed per unit time. Thus, the Beer-Lambert equation allows us to predict the intensity of light emitted by a fluorescent material as a function of the material concentration, optical path length, and quantum efficiency.

### 4.1.5 EINSTEIN EQUATION

The Einstein equation describing the quantum efficiency of fluorescence is given by [100]:

$$\phi_f = \frac{k_{if}}{k_{if} + k_{nr} + k_{ic}} \ , \tag{4.8}$$

where $\phi_f$ is the fluorescence quantum efficiency, $k_{if}$ is the radiative decay rate from the excited state to the ground state via fluorescence photon emission, $k_{nr}$ is the non-radiative decay rate from the excited state to the ground state through vibrational or rotational relaxation processes, and $k_{ic}$ is the radiative decay rate from the excited state to a lower quantum state via heat emission.

The radiative decay rate $k_{if}$ is given by:

$$k_{if} = \frac{2\pi}{\hbar} |\langle f|\hat{\mu}|i\rangle|^2 \rho(\nu) \ , \tag{4.9}$$

where $|i\rangle$ and $|f\rangle$ are the initial and final states, respectively, $\hat{\mu}$ is the electric dipole moment operator, $\rho(\nu)$ is the density of photonic states, and $\hbar$ is the reduced Planck constant.

The non-radiative decay rate $k_{nr}$ is given by:

$$k_{nr} = \frac{1}{\tau_{nr}} \ , \tag{4.10}$$

where $\tau_{nr}$ is the lifetime of the excited state through non-radiative processes.

The radiative decay rate $k_{ic}$ is given by:

$$k_{ic} = \frac{2\pi}{\hbar}|\langle i|\hat{\mu}|c\rangle|^2 \rho(\nu) \ , \tag{4.11}$$

where $|c\rangle$ is a state lower than the excited state. The equation shows that the quantum efficiency of fluorescence depends on the excited state's radiative and non-radiative decay rates.

The Einstein equation is fundamental for understanding the physics behind fluorescence and its application in various fields. It is used in fluorescence experiments to measure different fluorescent materials' quantum efficiency and optimize experimental conditions to maximize fluorescence intensity. Additionally, the Einstein equation is employed in research in chemistry, physics, and biology to study molecular dynamics, protein structure, and molecular interactions [101–104].

## 4.2 CHARACTERISTICS OF FLUORESCENCE EMISSION

A Jablonski diagram is schematized in Figure 16. The singlet electronic states of the ground state, as well as the first and second excited states, are represented by $S_0$, $S_1$, and $S_2$, respectively. In each of these electronic energy levels, fluorophores can exist in a series of vibrational energy levels, represented by 0, 1, 2, and so on. Vertical lines represent transitions between states, and it is highlighted that light absorption is instantaneous. The transitions occur in about $10^{-15}$ s, a time too short for significant nuclear displacement, according to the Franck-Condon principle [58].

Under ambient temperature conditions, the available thermal energy is insufficient to populate the excited vibrational states significantly. Thus, absorption and emission processes primarily occur from molecules in the lowest vibrational energy state. The energy difference between the excited states $S_0$ and $S_1$ is considerably high, making the thermal population of $S_1$ insufficient. For this reason, light rather than heat is used to induce fluorescence [58].

After light absorption, several processes typically occur. A fluorophore is generally excited to some higher vibrational level of $S_1$ or $S_2$. With some rare exceptions, molecules in condensed phases rapidly relax to the lowest vibrational level of $S_1$. This process is called internal conversion

**Figure 16** – *Schematic of the Jablonski Diagram.*
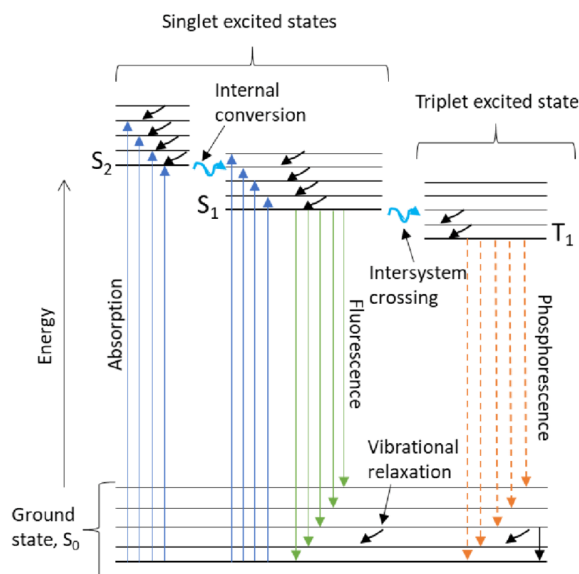


*Eiring, 2021[105].*

and generally occurs within $10^{-12}$ s or less. Since the lifetimes of fluorescence are typically close to $10^{-8}$ s, internal conversion is usually complete before emission. Therefore, fluorescence emission generally results from a thermally equilibrated excited state, i.e., the lowest vibrational energy state of $S_1$.

Return to the ground state generally occurs from a higher vibrational energy level in the excited ground state. Subsequently, this level rapidly reaches thermal equilibrium in a relaxation process ($10^{-12}$ s). An exciting consequence of emission to higher fundamental vibrational states is that the emission spectrum is typically a mirror image of the absorption spectrum of the $S_0 \rightarrow S_1$ transition.

Molecules in the $S_1$ state can also undergo spin conversion to the first triplet state $T_1$. The conversion from $S_1$ to $T_1$ is called intersystem crossing. The transition from $T_1$ to the singlet ground state is forbidden due to selection rules governing electronic transitions. However, although the $T_1$ to $S_0$ transition is considered forbidden, it can still occur in phosphorescence, but with a lower probability and over a longer time compared to fluorescence. Molecules containing heavy atoms, such as bromine and iodine, are often phosphorescent. The heavy atoms facilitate intersystem crossing, increasing the quantum yields of phosphorescence [30].

### 4.2.1 STOKES SHIFT AND KASHA'S RULE: PRINCIPLES AND IMPLICATIONS IN EMISSION SPECTROSCOPY

The phenomenon of fluorescence exhibits several general characteristics. Exceptions are known but rare. Generally, if a given fluorophore does not exhibit any general characteristics,

some particular behavior of that compound can be inferred.

### 4.2.1.1 The Stokes Shift

The analysis of the Jablonski diagram, Figure 16, reveals that the emission energy is generally lower than that of absorption. This phenomenon was first observed by Sir G. G. Stokes in 1852 at the University of Cambridge.

The Stokes shift is the difference between the positions of the absorption and emission peaks of the fluorescent molecule. It occurs due to the energy loss during the transition from the excited state back to the ground state, resulting in light emission with a longer wavelength (and consequently lower energy) than the absorbed light. It is important to note that energy losses between excitation and emission processes are common phenomena in fluorescent molecules in solution. One of the leading causes of the Stokes shift is the rapid decay of the molecule to the lowest vibrational level of the excited state $S_1$. Additionally, fluorophores tend to decay to higher vibrational levels of the ground state $S_0$, causing further loss of excitation energy due to the thermalization of excess vibrational energy. Besides these factors, fluorophores may exhibit additional Stokes shifts due to solvent-related effects, excited-state reactions, complex formation, and/or energy transfer [30].

### 4.2.1.2 Kasha's Rule

Another general property of fluorescence is that the same fluorescent emission spectrum is usually observed regardless of the excitation wavelength. Such phenomenon is known as Kasha's rule [30]. Excess energy is rapidly dissipated after excitation to higher electronic and vibrational levels, leaving the fluorophore in the lowest vibrational level of $S_1$. This relaxation occurs in about $10^{-12}$ s and is the result of a substantial overlap between several nearly equal energy states. Due to this rapid relaxation, emission spectra are generally independent of the excitation wavelength.

Exceptions exist, such as fluorophores in two ionization states, each exhibiting distinct absorption and emission spectra. Fluorophores in two ionization states are fluorescent molecules that can assume two distinct ionized forms depending on environmental conditions, such as pH or the presence of other ions. Each ionized form of the fluorophore has different absorption and emission properties, which can result in distinct absorption and emission spectra for each ionization state.

Additionally, some molecules are known to emit from the $S_2$ level, but such emission is rare and usually not observed in biological molecules. When a molecule emits from the $S_2$ level, the emission occurs from the second electronically excited state rather than the first excited

state ($S_1$), which is more common. The emission spectrum of a molecule emitting from the $S_2$ level may exhibit distinct features compared to molecules emitting from the $S_1$ level. Since the $S_2$ level has higher energy than the $S_1$ level, the emission energy of molecules emitting from the $S_2$ level will also be higher. This will result in shorter emission wavelengths compared to emission from the $S_1$ level. Due to $S_2$ level emission, the emission spectrum may not be a mirror image of the absorption spectrum corresponding to the $S_1$ level. Differences in peaks and spectrum shape may occur due to the electronic structure and energy distribution in the $S_2$ level. Furthermore, since the $S_2$ level is a higher energy excited state, the relaxation rate to the ground state ($S_0$) is generally faster. This can result in shorter emission lifetimes compared to emission from the $S_1$ level. Finally, due to the higher energy of the $S_2$ level, there is a greater likelihood of non-radiative processes, such as energy transfer to other molecules or internal conversion, competing with photon emission. This can lead to lower fluorescence quantum yields for molecules emitting from the $S_2$ level.

# SPECTROSCOPIC TECHNIQUES

THE APPLICATION of spectroscopic techniques has been a significant advancement in investigating the properties of matter in various scientific fields. These techniques provide precise and non-invasive information, enabling analyses of samples without compromising their integrity.

The history of spectroscopy began when researchers developed experimental methods in the accessible region of the electromagnetic spectrum, enabling them to employ the human eye as a detector. Progress in technology and a deeper understanding of the fundamental principles of physics and chemistry have further expanded the application of different regions of the electromagnetic spectrum for various types of samples [106–108].

Researchers use visible and ultraviolet light absorption and emission spectroscopy to determine the molecular structure of organic and inorganic compounds [109–111]. Conversely, they apply infrared and Raman spectroscopy techniques to identify chemical bonds in molecules and compounds [112–114]. Nuclear magnetic resonance spectroscopy and X-ray photoelectron spectroscopy are powerful tools for studying the electronic structure of materials at an atomic scale.

Advanced microscopy techniques, such as transmission electron microscopy, provide an enlarged view beyond the human eye's capability, allowing the observation of structures at the nanometer scale. This capability is essential for understanding morphology at significantly reduced scales, enabling precise and detailed analyses of the organization of materials in their most elementary form.

This chapter is intended to describe the experimental techniques used to extract information and characterize the materials analyzed in this study. The objective is to provide a comprehensive overview of the techniques employed to obtain detailed information about the properties of the materials, such as the absorption spectrum, emission, and lifetime of the samples.

## 5.1 ABSORPTION

The absorption process is essential for understanding various physical and chemical processes, as it transfers energy between photons and electrons in a system. In Chapter 1, the fundamental aspects of this phenomenon were addressed, including the explanation of the process of promoting an electron to an excited state and returning to the ground state with the emission of a photon. This understanding is essential for interpreting the various experimental results.

Absorption spectroscopy is a widely used technique across all regions of the electromagnetic spectrum. Conducting an absorption experiment is straightforward, requiring only four main elements: a light source, an absorption cell, a dispersing element, and a detector. Figure 17 illustrates this simple experimental apparatus.

**Figure 17** – *Main components of an absorption experiment.*



| Light Source | Collimator | Prism or Grating | Wavelength Selector | Sample Solution | Detector |
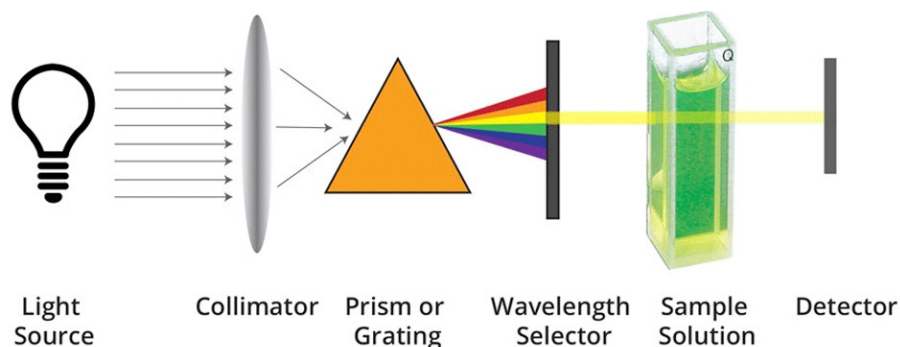
*WPI, 2019 [115].*

The choice of an appropriate light source for an absorption spectroscopy experiment is related to the region of the electromagnetic spectrum in which the sample absorbs. Generally, the light source must present a broad range of wavelengths with uniform intensity. Tungsten filaments and deuterium lamps commonly emit light in the visible and near-ultraviolet range.

The cell in the absorption technique must allow the radiation emitted by the source to pass through the sample and have an appropriate wavelength for absorption. Researchers commonly use quartz cuvettes with polished faces for the absorption tests. However, various other cells are available, such as glass, KBr, and mica cells, which should be chosen according to experimental needs. The dispersing element, in turn, is responsible for separating the wavelengths of the light transmitted by the sample. This process can be performed using a prism, a diffraction grating, or an interferometer.

In absorption spectroscopy, the detector measures the radiation transmitted by the sample after passing through the dispersing element. The available detectors are crystal diodes, Golay cells, photomultipliers, and photographic plates. Currently, most spectrometers employ CCD cameras as detectors. The collected spectrum is usually sent to a computer and processed by specialized software that displays and captures the data, presented in a graph of absorbance or percentage of transmittance as a function of wavelength or wavenumber.

In high-resolution spectroscopy, the phase of the material is a critical factor that must be considered. The sample is generally in the gas phase at low pressure, as this is where information about the rotational structure is best obtained. In the liquid phase, this information is not as readily available, and in the solid phase, rotational movement is extinguished. Therefore, to avoid a loss of information, it is necessary to carefully choose the range of the electromagnetic spectrum where absorption occurs and consider the phase in which the material should be.

In the following chapters, we obtained the absorption measurements using the Ocean Optics UV-VIS spectrometer with plate number 1. A computer program can interpret the resulting spectrum, which produces a graph of absorbance or transmittance as a function of wavelength or wavenumber.

## 5.2 EMISSION

Specific equipment can perform absorption and emission spectrum measurements, as the experimental setups for both techniques are similar. The emission spectrum of a sample is the wavelength distribution of the light emitted when excited by a single wavelength [116]. Typically, researchers represent this spectrum as intensity versus wavelength (measured in nm), but in some cases, they display it as a function of wavenumber (measured in $cm^{-1}$).

A spectrofluorometer is an equipment used for measuring light emission. The equipment uses a xenon lamp, which produces high-intensity light with a broad emission spectrum. Motorized monochromators in the equipment allow for the automatic selection of excitation and emission wavelengths [116]. These monochromators are motorized, enabling automatic scanning of all wavelengths. A photomultiplier tube detects the emission, and the data is then sent to a computer for processing by specialized software, which generates the spectrum graph.

Spectrofluorometers feature optical components that support the sample, such as the shutter

**Figure 18** – *Spectrometer. 1) connector; 2) slit; 3) filter; 4) collimator mirror; 5) diffraction grating; 6) focusing mirror; 7) detector collection lens L2; 8) detector.*
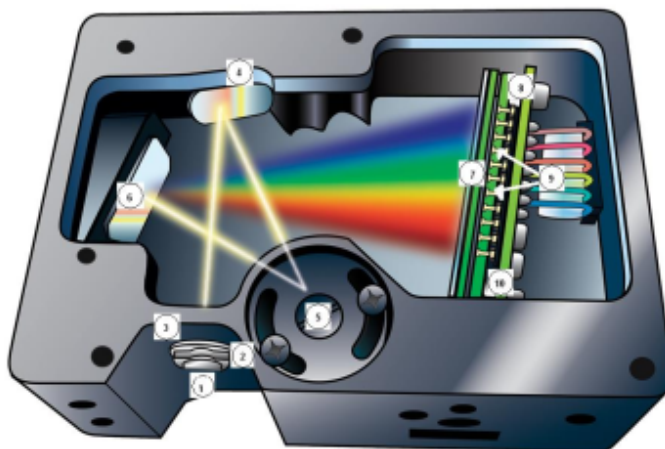


*USB2000+ Fiber Optic Spectrometer Operation Manual, 2010. [117]*

and beam splitter. The beam splitter is used to obtain a reference beam, which can help correct variations in the light source's intensity.

A widely used instrument in emission analyses is the spectrometer, which exhibits remarkable versatility in experimental configuration and is notably helpful in spectroscopy laboratories. This equipment consists of a static module that includes mirrors, filters, diffraction gratings, and a CCD detector. Incident light in the spectrometer passes through a slit and a filter before being reflected by a first mirror, which collimates it for the diffraction grating. The resulting beam, decomposed into different wavelengths, is reflected by a second mirror and directed to the CCD detector.

As with the spectrofluorometer, the collected data are interpreted by software that generates the intensity graph versus wavelength (or wavenumber). Figure 19 illustrates a standard experimental configuration used in spectroscopy tests employing a spectrometer.

## 5.3 LIFETIME

The study of the dynamics of excited states is essential for understanding photophysical, photobiological, and photochemical processes. Two time-resolved techniques used to measure lifetime are pulse fluorometry and phase modulation fluorometry. The former involves exciting the sample with a short light pulse, while the latter involves excitation with sinusoidally modulated

**Figure 19** – *Typical emission collection setup using a spectrometer.*
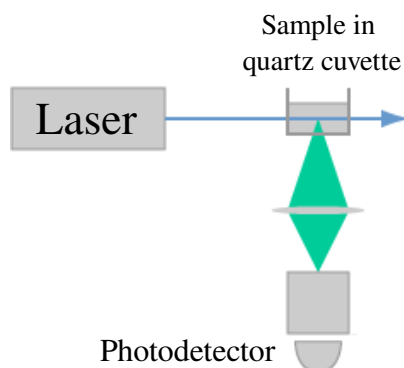


*Paschotta [118].*

light at high frequency. Although theoretically equivalent, pulse fluorometry is more suitable for visualizing fluorescence decay, making it the technique of choice for the lifetime measurements presented in this work. Figure 20 illustrates the principles of these techniques.

**Figure 20** – *Principles of phase-modulation fluorometry. The phase shift $\phi$ and the modulation ratio $M = m/m_0$, where $m$ is the modulation depth of the fluorescence, characterize the harmonic response of the system. These parameters are measured as a function of the modulation frequency. The dotted line on the right represents the corresponding fluorescence.*
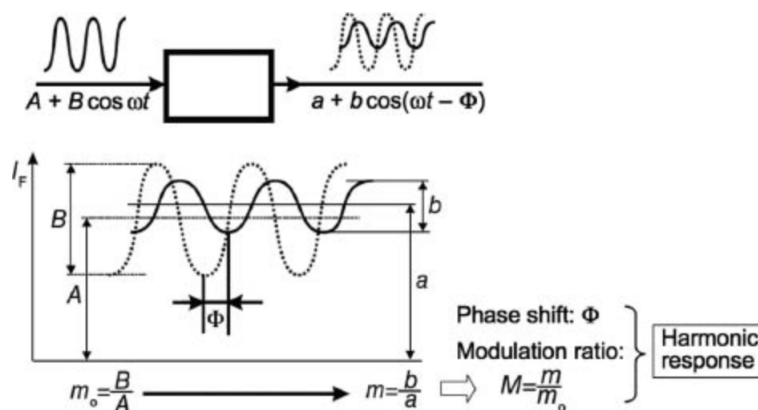


*Adapted from Valeur et al., 2012. [119]*

A light pulse exciting a sample produces fluorescence intensity that follows exponential decay. This decay mathematically describes a sum of exponentials, indicating the excitation of multiple states. The time constant obtained from this exponential decay is known as the excited state lifetime. In most cases, the decay better represents a sum of exponentials due to the excitation of various states. The exponential decay of fluorescence intensity $I(t)$ can be mathematically expressed as:

$$I(t) = \alpha e^{-t/\tau} \ , \tag{5.1}$$

where $\tau$ is the decay time (or lifetime) and $\alpha$ is the pre-exponential factor or amplitude.

In scenarios where the decay is monoexponential, $\alpha$ is the intensity at time $t = 0$. For multiexponential decay with $n$ components, the intensity $I(t)$ is written as:

$$I(t) = \sum_{i=1}^{n} \alpha_i e^{-t/\tau_i}. \tag{5.2}$$

In cases where the fluorescence decay is multiexponential, the lifetime (or average decay time) can be defined as:

$$< \tau > = \frac{\sum_{i=1}^{n} \alpha_i \tau_i}{\sum_{i=1}^{n} \alpha_i}. \tag{5.3}$$

Pulse fluorometry is a widely used technique for determining the lifetime of excited states. This method counts photons emitted by the sample after light pulse excitation. The fluorescence intensity is proportional to the probability of detecting a single photon at a given time. After repeated excitation, researchers time and record individual photons, allowing them to reconstruct the fluorescence decay curve. A conventional photon counting instrument includes an excitation source (flash lamp or laser), a time-to-amplitude converter (TAC), and a photomultiplier. The decay curve is constructed from a histogram of pulse heights generated after many excitation and detection cycles. The technique offers high sensitivity, excellent dynamic range and linearity, and well-defined statistics (Poisson distribution), allowing for the analysis's proper weighting of data points.

The lifetime measurements in the present thesis were acquired using the Horiba NanoLog UV-VIS-NIR Fluorometer at the Laboratory of Nano-Photonics and Imaging (IF-UFAL).

This section provides an overview of the experimental techniques employed in the study. The upcoming section will delve into the computational methods, detailing the pivotal Density Functional Theory used for the theoretical analysis in this thesis.

**Figure 21** – *The operation of a conventional single-photon counting instrument, including the generation and routing of electrical pulses, excitation of the sample, and photon detection using a photomultiplier. After a large number of excitation and detection events, the histogram of pulse heights represents the fluorescence decay curve.*
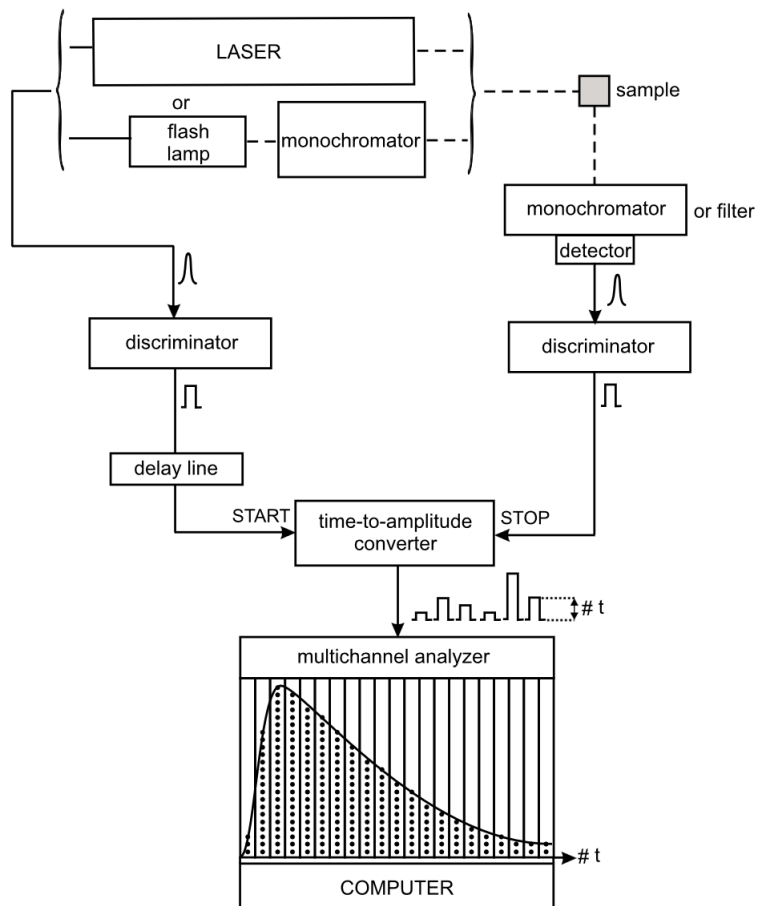


*Valeur et al., 2012. [119]*

# DENSITY FUNCTIONAL THEORY

COMPUTACIONAL simulations have become a valuable tool for the mathematical modeling of many natural systems with applications in areas such as physics, astrophysics, climatology, chemistry, biology, and engineering [120–124]. This tool is powerful for estimating complex systems. The resulting mathematical dynamics from the program execution represent the behavior of the natural system. The advantages of computational simulations include testing proposed models of natural phenomena and generating data that may be difficult to obtain experimentally.

Monte Carlo (MC) simulations and Molecular Dynamics (MD) simulations utilize prototype systems, which interact through a known force field and provide valuable information on thermodynamics, structure, and, in the case of MD, the dynamics of liquids. The success of these methods lies mainly in the quality of the potential models employed without compromising the computational feasibility of the calculations. Compared to macroscopic systems, the application of these models to systems of reduced size is sufficient to allow measurements of observable properties in remarkable agreement with experimental data.

However, quantum mechanics simulate chemical systems, including electronic structure calculations and molecular spectroscopy. *Ab initio* methods[1] usually are employed that use Schrödinger's equations to describe the electronic structure of molecules, and the simulations are performed through numerical methods that solve these equations [62].

Envisaging the use of quantum mechanics methods to simulate chemical systems, the Hartree-Fock (HF) method has garnered significant interest. This method is widely used in theoretical

---

[1]*Ab initio* methods are computational theoretical chemistry methods used to calculate properties of molecules and materials without using experimental information or prior data. The term "ab initio" comes from Latin and means "from first principles".

chemistry and physics because it provides an approximate description of the behavior of electrons in molecules and solids. The application of this method allows researchers to investigate and predict molecular properties, such as energy, equilibrium geometry, and vibrational spectra. The HF method calculates molecules' electronic structure and aims to find the solution to the system's Schrödinger equation. The Hartree-Fock energy is not as low as the exact energy. The difference is due to electron correlation effects and is called the correlation energy. The Hartree-Fock wavefunction does not include these correlation effects because it describes the electrons as moving in the average potential field of all the other electrons (more details in 6.2.1). This method is based on an approximation that considers the system's wave function through a single Slater determinant.

Density Functional Theory (DFT) is is a quantum-mechanical method used in theoretical chemistry to calculate properties of chemical systems, such as binding energy, molecular geometry, polarizability, and electron density, among other properties [125]. The main difference between DFT and other ab initio methods is that electron density is the fundamental variable, unlike the wave function used by traditional quantum mechanics methods. DFT uses an approximation for the density functional, a mathematical expression that relates the electron density to the system's total energy.

On the other hand, the Hohenberg-Kohn Theorem, which establishes that electron density contains all the necessary information to determine the system's total energy, is the basis for DFT [126]. This means that, from the theorem, it is possible to determine the total energy of a chemical system only with its electron density. With this in mind, we will delve deeper into the concepts discussed in this section.

## 6.1 BORN-OPPENHEIMER APPROXIMATION

The problem essentially consists of obtaining solutions to the Schrödinger equation for a system with $n$ electrons at $\mathbf{r} = \{\mathbf{r}_i\}$ and $N$ nuclei at $\mathbf{R} = \{\mathbf{r}_\alpha\}$. Considering only the electrostatic interactions between the particles, the Schrödinger equation is given by

$$\widehat{\mathbf{H}}|\Psi(\mathbf{r};\mathbf{R})\rangle = E|\Psi(\mathbf{r};\mathbf{R})\rangle, \tag{6.1}$$

where $\widehat{\mathbf{H}}$ is the Hamiltonian of the system given by:

$$\widehat{\mathbf{H}} = -\sum_{\alpha=1}^{N} \frac{1}{2m_\alpha} \nabla_\alpha^2 - \sum_{i=1}^{n} \frac{1}{2} \nabla_i^2 + \sum_{\alpha}^{N} \sum_{\beta>\alpha}^{N} \frac{Z_\alpha Z_\beta}{r_{\alpha\beta}} - \sum_{i}^{n} \sum_{\alpha}^{N} \frac{Z_\alpha}{r_{i\alpha}} + \sum_{i}^{n} \sum_{j>i}^{n} \frac{1}{r_{ij}}. \tag{6.2}$$

In the given context, $Z_\alpha$ and $m_\alpha$ correspond to the atomic number and mass of the nucleus $\alpha$ respectively. At the same time, $r_{\alpha\beta}$ represents the distance between the nuclei $\alpha$ and $\beta$, $r_{i\alpha}$ denotes the distance between the electron $i$ and the nucleus $\alpha$, and $r_{ij}$ stands for the distance between the electrons $i$ and $j$.

To simplify, the Hamiltonian can be expressed as:

$$\widehat{\mathbf{H}} = \widehat{\mathbf{T}}_N(\mathbf{R}) + \widehat{\mathbf{T}}_e(\mathbf{r}) + \widehat{\mathbf{U}}_{NN}(\mathbf{R}) + \widehat{\mathbf{U}}_{eN}(\mathbf{r};\mathbf{R}) + \widehat{\mathbf{U}}_{ee}(\mathbf{r}). \tag{6.3}$$

The first and second terms in the above expression are the nuclear and electronic kinetic energies, respectively. The other terms are associated with the nucleus-nucleus, electron-nucleus, and electron-electron interactions. For simplicity, the equations will be written in the Hartree atomic units (a.u.) system where the electron mass ($m_e$), electron charge ($e$), Bohr radius ($a_0$), Coulomb's law constant ($1/4\pi\varepsilon_0$), and Dirac constant ($\hbar$) are defined as unitary.

In expression 6.3, the term $\widehat{\mathbf{U}}_{eN}(\mathbf{r};\mathbf{R})$ prevents the separation of the Hamiltonian into an electronic and a nuclear part, which would allow writing the wave function as a product of a nuclear and an electronic term ($\Psi(\mathbf{r};\mathbf{R}) = \psi(\mathbf{r})\phi(\mathbf{R})$). Considering that the electrostatic forces between electrons and nuclei acting on the system are of the same order of magnitude, the variations in the momenta of the particles caused by these forces must also be of the same order of magnitude. Assuming that the momenta of the electrons and nuclei are of the same order of magnitude, the more massive nuclei will have much lower velocities than the electrons. Thus, on the time scale of nuclear motions, the electrons quickly relax to the configuration corresponding to the stationary state at that instant. Therefore, solving the time-independent Schrödinger equation is acceptable, assuming that the nuclei are stationary. Initially, the problem for the electronic ground state is solved, and then the system's energy in the configuration corresponding to this state is calculated, including the nuclear motion. This separation of electronic and nuclear motion is known as the Born-Oppenheimer approximation [127] and allows separating the electronic

and nuclear wave functions ($\Psi(\mathbf{r}; \mathbf{R}) = \psi(\mathbf{r}; \mathbf{R})\phi(\mathbf{R})$), where the parametric dependence of the potential $\widehat{U}_{eN}(\mathbf{r}; \mathbf{R})$ with $R$ was created. When using this approximation, the Schrödinger equation must be written while considering the nuclei as fixed:

$$\widehat{H}'\psi(\mathbf{r}; \mathbf{R}) = E'\psi(\mathbf{r}; \mathbf{R}), \tag{6.4}$$

where $\widehat{H}'$ is given by:

$$\widehat{H}' = \widehat{T}_e(\mathbf{r}) + \widehat{U}_{NN}(\mathbf{R}) + \widehat{U}_{eN}(\mathbf{r}; \mathbf{R}) + \widehat{U}_{ee}(\mathbf{r}). \tag{6.5}$$

Since $\widehat{T}_e(\mathbf{r}) \gg \widehat{T}_N(\mathbf{R})$, the term $\widehat{T}_N(\mathbf{R})$ has been eliminated from the Hamiltonian. In general, the second term is neglected in expression 6.5, as this term contributes only with a shift in the energy levels since $\mathbf{R}$ enters as a parameter in the Hamiltonian and consequently $\widehat{U}_{NN}(\mathbf{R})$ will contribute as a constant. Removing $\widehat{U}_{NN}(\mathbf{R})$ from the Hamiltonian, the electronic Schrödinger equation can be written as:

$$\widehat{H}_e\psi(\mathbf{r}; \mathbf{R}) = E_e\psi(\mathbf{r}; \mathbf{R}), \tag{6.6}$$

where $\widehat{H}_e$ is the electronic Hamiltonian given by:

$$\widehat{H}_e = \widehat{T}_e(\mathbf{r}) + \widehat{U}_{eN}(\mathbf{r}; \mathbf{R}) + \widehat{U}_{ee}(\mathbf{r}). \tag{6.7}$$

Rewriting the Schrödinger equation considering the total Hamiltonian 6.3 and rewriting the wave function in terms of the electronic ($\psi(\mathbf{r}; \mathbf{R})$) and nuclear ($\phi(\mathbf{R})$) wave functions, we obtain

$$\left[\widehat{T}_N(\mathbf{R}) + \widehat{T}_e(\mathbf{r}) + \widehat{U}_{NN}(\mathbf{R}) + \widehat{U}_{eN}(\mathbf{r}; \mathbf{R}) + \widehat{U}_{ee}(\mathbf{r})\right] \psi(\mathbf{r}; \mathbf{R})\phi(\mathbf{R}) = E\psi(\mathbf{r}; \mathbf{R})\phi(\mathbf{R}). \tag{6.8}$$

Using 6.6 and 6.7, and applying the chain rule for $\widehat{T}_N(\mathbf{R}) = -\sum_{\alpha=1}^{N} \frac{1}{2m_\alpha}\nabla_\alpha^2$, we can write

$$\left(\widehat{U}_{NN}(\mathbf{R}) + E_e\right) \psi(\mathbf{r}; \mathbf{R})\phi(\mathbf{R}) + \psi(\mathbf{r}; \mathbf{R})\widehat{T}_N(\mathbf{R})\phi(\mathbf{R}) - \sum_{\alpha=1}^{N} \frac{1}{2m_\alpha} \left[2\nabla_\alpha\psi(\mathbf{r}; \mathbf{R})\nabla_\alpha\phi(\mathbf{R})\right.$$
$$\left. + \phi(\mathbf{R})\nabla_\alpha^2\psi(\mathbf{r}; \mathbf{R}) = E\psi(\mathbf{r}; \mathbf{R})\phi(\mathbf{R}). \tag{6.9}$$

The terms in brackets, which are proportional to the first and second derivatives of the

electronic wave function concerning the nuclear coordinates, are known as vibronic coupling terms. These terms are difficult to calculate and are neglected in the Born-Oppenheimer approximation, as the term $\nabla_\alpha \psi(\mathbf{r}; \mathbf{R})$ is approximately of the same order of magnitude as $\nabla_i \psi(\mathbf{r}; \mathbf{R})$ and consequently the contribution of the term in brackets will be of the order of $1/(2m_\alpha) \nabla_\alpha^2 \psi(\mathbf{r}; \mathbf{R}) \approx p_e^2/(2m_\alpha) = (m_e/m_\alpha) T_e \sim 1/1840 T_e$. Thus, after neglecting the vibronic coupling, we obtain

$$\psi(\mathbf{r}; \mathbf{R}) \widehat{\mathbf{T}}_N(\mathbf{R}) \phi(\mathbf{R}) + \widehat{\mathbf{U}}_{NN}(\mathbf{R}) \psi(\mathbf{r}; \mathbf{R}) \phi(\mathbf{R}) + E_e \psi(\mathbf{r}; \mathbf{R}) \phi(\mathbf{R}) = E \psi(\mathbf{r}; \mathbf{R}) \phi(\mathbf{R}). \quad (6.10)$$

Consequently, a nuclear Schrödinger equation can be written as

$$\widehat{\mathbf{H}}_N \phi(\mathbf{R}) = \left[ \widehat{\mathbf{T}}_N(\mathbf{R}) + \widehat{\mathbf{U}}_{NN}(\mathbf{R}) + E_e \right] \phi(\mathbf{R}) = E \phi(\mathbf{R}). \quad (6.11)$$

The movement of the nuclei is determined by the potential generated by the electrons, which can be computed by solving the electronic problem for a specific set of nuclear coordinates, as described by the equation.

$$\widehat{\mathbf{H}}_e \psi(\mathbf{r}; \mathbf{R}) = \left[ \widehat{\mathbf{T}}_e(\mathbf{r}) + \widehat{\mathbf{U}}_{eN}(\mathbf{r}; \mathbf{R}) + \widehat{\mathbf{U}}_{ee}(\mathbf{r}) \right] \psi(\mathbf{r}; \mathbf{R}) = E_e \psi(\mathbf{r}; \mathbf{R}). \quad (6.12)$$

## 6.2 THE HARTREE-FOCK METHOD

The already well-established Hartree-Fock method boasts significant relevance. It not only provides a pleasing estimate for the challenge involving multiple electrons but also serves as a starting point for other sophisticated techniques, such as Møller-Plesset perturbation methods (MP) and Density Functional Theory (DFT), both of which will be addressed throughout the chapter.

Initially, it is essential to consider the Born-Oppenheimer approximation, whose purpose is to solve the electronic Schrödinger equation. In an electronic system, the wave function must adhere to the property of antisymmetry when exchanging coordinates of a pair of electrons. [62]. This antisymmetry can be incorporated by representing the wave function as a combination of specific determinants. These determinants are known as Slater determinants [62].

However, solving this issue presents a considerable challenge. An appropriate approximation

consists of replacing the impediment of identifying a single wave function for the $N$ electrons of the system with the problem of determining $N$ individual wave functions for one electron, known as molecular spin-orbitals. This approximation is the essence of the HF method, and according to this model, the wave function can be written as just one Slater determinant:

$$\psi = \psi(\mathbf{r}; \mathbf{R}) = \frac{1}{\sqrt{n!}} \begin{vmatrix} \chi_1(\mathbf{r}_1) & \chi_2(\mathbf{r}_1) & \cdots & \chi_n(\mathbf{r}_1) \\ \chi_1(\mathbf{r}_2) & \chi_2(\mathbf{r}_2) & \cdots & \chi_n(\mathbf{r}_2) \\ \vdots & \vdots & \ddots & \vdots \\ \chi_1(\mathbf{r}_n) & \chi_2(\mathbf{r}_n) & \cdots & \chi_n(\mathbf{r}_n) \end{vmatrix} \tag{6.13}$$

where $\chi_i(\mathbf{r}_j)$ correspond to the normalized single-electron molecular spin-orbitals. It is simple to prove that the described wave function is normalized.

According to the properties of determinants, it can be observed that the exchange of coordinates between two electrons $(\mathbf{r}_i \leftrightarrow \mathbf{r}_j)$ implies the inversion of the sign of the electronic wave function.

Effectively, by swapping columns $i$ and $j$ of the determinant:

$$\psi(\mathbf{r}_1, \ldots, \mathbf{r}_i, \ldots, \mathbf{r}_j, \ldots, \mathbf{r}_n) \rightarrow \psi(\mathbf{r}_1, \ldots, \mathbf{r}_j, \ldots, \mathbf{r}_i, \ldots, \mathbf{r}_n). \tag{6.14}$$

According to the properties of determinants, the permutation of two columns results in the inversion of the determinant's sign:

$$det(\psi(\mathbf{r}_1, \ldots, \mathbf{r}_j, \ldots, \mathbf{r}_i, \ldots, \mathbf{r}_n)) = -det(\psi(\mathbf{r}_1, \ldots, \mathbf{r}_i, \ldots, \mathbf{r}_j, \ldots, \mathbf{r}_n)). \tag{6.15}$$

Furthermore, it is observed that two identical spin-orbitals imply two identical columns in the determinant, rendering it null. This is consistent with the Pauli exclusion principle, which states that two electrons cannot occupy the same quantum state.

Using Dirac notation, the HF wave function can be written in a manner equivalent to the determinant form [68]:

$$|\psi\rangle = \frac{1}{\sqrt{n!}} \sum_{i=1}^{n!} (-1)^{p_i} \left| \widehat{\mathcal{P}}_i \{\chi_1(1)\chi_2(2)\ldots\chi_n(n)\} \right\rangle, \tag{6.16}$$

where $\chi_l(j) \equiv \chi_l(\mathbf{r}_j)$, $\widehat{\mathcal{P}}_i$ is the operator that generates the $i$-th permutation of the particle

coordinates, and $p_i$ is the minimum number of pair exchange operations needed to transform the state $|\chi_1(1)\chi_2(2)\ldots\chi_n(n)\rangle$ into the state $\left|\widehat{\mathcal{P}}_i\left\{\chi_1(1)\chi_2(2)\ldots\chi_n(n)\right\}\right\rangle$. Thus, the expected value of the electronic Hamiltonian is:

$$\left\langle \psi\left|\widehat{\mathbf{H}}_e\right|\psi\right\rangle = \langle\psi\left|(\mathcal{O}_1 + \mathcal{O}_2)\right|\psi\rangle = \langle\psi\left|\mathcal{O}_1\right|\psi\rangle + \langle\psi\left|\mathcal{O}_2\right|\psi\rangle, \tag{6.17}$$

where $\mathcal{O}_1$ and $\mathcal{O}_2$ are one-electron and two-electron operators, given by

$$\mathcal{O}_1 = \sum_{i=1}^{n} h(i), \tag{6.18}$$

with

$$h(i) = -\frac{1}{2}\nabla_i^2 - \sum_{\alpha}^{N}\frac{Z_\alpha}{r_{i\alpha}}, \tag{6.19}$$

and

$$\mathcal{O}_2 = \sum_{i}^{n}\sum_{j>i}^{n}\frac{1}{r_{ij}}. \tag{6.20}$$

From equations (6.18) and (6.20), the expected value of the operator $\mathcal{O}_1$, which acts on an electron, is calculated using antisymmetric permuted wave functions. The simplified expression for the expected value of the operator $\mathcal{O}_1$ is obtained by considering the symmetry of the permuted wave functions and the indistinguishability of identical particles in quantum mechanics. The final expression is a sum of the expected values of $\mathcal{O}_1$ in all possible states $\alpha$. Next, the average value of the two-electron operator, $\mathcal{O}_2$, is calculated similarly, again considering the symmetry of the permuted wave functions and the indistinguishability of identical particles in quantum mechanics, as discussed in Appendix A.

$$E(\psi) = \langle\psi|\widehat{\mathbf{H}}|\psi\rangle = \sum_{\alpha=1}^{n}\langle\alpha|h|\alpha\rangle + \frac{1}{2}\sum_{\alpha,\beta}\langle\alpha\beta||\alpha\beta\rangle. \tag{6.21}$$

This equation is an expression to calculate the total expected energy, $E(\psi)$, of a quantum system described by a wave function $\psi$, considering an orthogonal basis of states. The equation consists of two main parts. The first part of the equation, $\sum_{\alpha=1}^{n}\langle\alpha|h|\alpha\rangle$, represents the kinetic and potential energy of the electrons in the system. The operator $\widehat{\mathbf{H}}$ is the Hamiltonian operator, which

describes the system's total energy. The symbol $\langle\alpha|h|\alpha\rangle$ is a Dirac notation (bra-ket) representing the expected value of the Hamiltonian operator for the state $|\alpha\rangle$. The sum is performed over all possible states, from $1$ to $n$. The second part of the equation, $\frac{1}{2}\sum_{\alpha,\beta}\langle\alpha\beta|\alpha\beta\rangle$, describes the electrostatic repulsion energy between the electrons. The term $\langle\alpha\beta|\alpha\beta\rangle$ represents the repulsion energy between the electrons in the states $|\alpha\rangle$ and $|\beta\rangle$. The factor $1/2$ is necessary to avoid double-counting the interactions between the electrons, as the sum is performed over all possible pairs of states $(\alpha, \beta)$.

Initially, an approximation for the wave function was adopted, assuming it could be described as a single Slater determinant. To find the closest value to the exact energy, minimizing the HF energy expression (6.21) is necessary; for that, the variational theorem must be used. The functional to be minimized is given by:

$$\mathcal{L} = E - \sum_{\alpha,\beta}\varepsilon_{\alpha\beta}\left(\langle\alpha\mid\beta\rangle - \delta_{\alpha\beta}\right). \tag{6.22}$$

where $\delta_{\alpha\beta}$ is the Kronecker delta. This problem can be solved using the technique of Lagrange multipliers. The solution to this problem is continued in Appendix B. Thus, we have

$$\delta\mathcal{L} = \sum_{\alpha}\langle\delta\alpha|h|\alpha\rangle + \sum_{\alpha,\beta}(\langle\delta\alpha\beta\mid\alpha\beta\rangle - \langle\delta\alpha\beta\mid\beta\alpha\rangle) - \sum_{\alpha,\beta}\varepsilon_{\alpha\beta}\langle\delta\alpha\mid\beta\rangle + \mathcal{CC}, \tag{6.23}$$

where $\mathcal{CC}$ represents the complex conjugate of the previous terms. Usually, a one-electron Coulomb operator $\widehat{\mathbf{J}}_{\beta}(1)$ is defined, which represents the repulsion resulting from electron $\beta$, according to the relation:

$$\widehat{\mathbf{J}}_{\beta}(1)\chi_{\alpha}(1) = \left\langle\chi_{\beta}(2)\left|\frac{1}{r_{12}}\right|\chi_{\beta}(2)\right\rangle\chi_{\alpha}(1), \tag{6.24}$$

and an exchange operator $\widehat{\mathbf{K}}_{\alpha}(\beta)$,

$$\widehat{\mathbf{K}}_{\beta}(1)\chi_{\alpha}(1) = \left\langle\chi_{\beta}(2)\left|\frac{1}{r_{12}}\right|\chi_{\alpha}(2)\right\rangle\chi_{\beta}(1). \tag{6.25}$$

Using these definitions, the expression (6.23) can be rewritten as

$$\delta\mathcal{L} = \sum_{\alpha} \left\langle \delta\alpha \left| \left\{ \widehat{\mathbf{F}}(1)|\alpha\rangle - \sum_{\beta} \varepsilon_{\alpha\beta}|\beta\rangle \right\} \right. + \mathcal{CC} \right., \tag{6.26}$$

where

$$\widehat{\mathbf{F}}(1) = h(1) + \sum_{\beta} \left[ \widehat{\mathbf{J}}_{\beta}(1) - \widehat{\mathbf{K}}_{\beta}(1) \right] \tag{6.27}$$

is the Fock operator[2]. To find a minimum for the functional $\mathcal{L}$, we must have $\delta\mathcal{L} = 0$. In this way, we can write equivalently.

$$\widehat{\mathbf{F}}(1)|\alpha\rangle = \sum_{\beta} \varepsilon_{\alpha\beta}|\beta\rangle. \tag{6.28}$$

Since $\varepsilon_{\alpha\beta}$ are elements of a Hermitian matrix $\bar{\varepsilon}$, a unitary operator $\widehat{U}$ can be applied to transform the set $\{|\beta\rangle\}$, in such a way that the matrix $\bar{\varepsilon}$ is diagonal in this new basis. Under these conditions,

$$\widehat{\mathbf{F}}'(1)\left|\alpha'\right\rangle = \sum_{\beta'} \varepsilon_{\alpha'\beta'}\left|\beta'\right\rangle = \varepsilon_{\alpha'}\left|\alpha'\right\rangle, \tag{6.29}$$

where $\widehat{\mathbf{F}}'(1)$ is the Fock operator in the new basis, $|\alpha'\rangle \equiv \widehat{U}|\alpha\rangle$ are the elements of the new basis, and $\varepsilon_{\alpha'} = \varepsilon_{\alpha'\alpha'}$ are the non-zero elements (on the diagonal) of the matrix $\bar{\varepsilon}$ written in the new basis.

It is important to note that the new wave function $\psi'$ differs from $\psi$ by only a phase factor $e^{i\varphi}$e, as the observables depend only on $|\psi|^2$, the states $\psi'$ and $\psi$ are equivalent.

To calculate the representation of the Fock operator on this new basis, consider the following:

$$\sum_{\alpha} \widehat{\mathbf{J}}_{\alpha'} = \sum_{\alpha} \left\langle \alpha' \left| \frac{1}{r_{12}} \right| \alpha' \right\rangle = \sum_{\alpha} \left\langle \alpha \left| \widehat{U}^{\dagger} \frac{1}{r_{12}} \widehat{U} \right| \alpha \right\rangle \tag{6.30}$$

---

[2]Note that the Fock operator is defined as the sum of the one-electron Hamiltonian operator, which includes kinetic energy and external potential, the Coulomb operator for electron 1, which describes the average electrostatic repulsion interaction between electron 1 and all other electrons in the system, with the electron density represented by the occupied orbitals $\beta$, and the exchange operator for electron 1, which arises due to the Pauli exclusion principle and the symmetry of electronic wave functions.

$$= \sum_{\alpha,\beta,\gamma} \langle \alpha \mid \beta' \rangle \left\langle \beta \left| \frac{1}{r_{12}} \right| \gamma \right\rangle \langle \gamma' \mid \alpha \rangle$$

$$= \sum_{\alpha,\beta,\gamma} \left\langle \beta \left| \frac{1}{r_{12}} \right| \gamma \right\rangle \langle \gamma' \mid \alpha \rangle \langle \alpha \mid \beta' \rangle$$

$$= \sum_{\beta} \left\langle \beta \left| \frac{1}{r_{12}} \right| \beta \right\rangle = \sum_{\beta} \widehat{\mathbf{J}}_\beta = \sum_{\alpha} \widehat{\mathbf{J}}_\alpha.$$

Similarly, it can be shown that $h'(1) = h(1)$ and $\sum_\alpha \widehat{\mathbf{K}}_{\alpha'} = \sum_\alpha \widehat{\mathbf{K}}_\alpha$ and consequently, $\widehat{\mathbf{F}}' = \widehat{\mathbf{F}}$. Thus, by suppressing the lines, we obtain

$$\widehat{\mathbf{F}}(1)|\alpha\rangle = \varepsilon_\alpha|\alpha\rangle, \tag{6.31}$$

where

$$\widehat{\mathbf{F}}(1)|\alpha\rangle = h(1)|\alpha\rangle + \sum_\beta \left[ \widehat{\mathbf{J}}_\beta(1)|\alpha\rangle - \widehat{\mathbf{K}}_\beta(1)|\alpha\rangle \right]$$

$$= h(1)|\alpha(1)\rangle + \sum_\beta \left[ \left\langle \beta(2) \left| \frac{1}{r_{12}} \right| \beta(2) \right\rangle |\alpha(1)\rangle - \left\langle \beta(2) \left| \frac{1}{r_{12}} \right| \alpha(2) \right\rangle |\beta(1)\rangle \right]. \tag{6.32}$$

The equation (A.10) is known as the Hartree-Fock equation.

The orbital energies can be obtained by substituting the Fock operator equation into the above expression and performing some manipulations. In this way, we obtain

$$\varepsilon_\alpha^{(so)} = \langle \alpha \left| \varepsilon_\alpha \right| \alpha \rangle = \langle \alpha|h|\alpha \rangle + \sum_\beta \langle \alpha\beta||\alpha\beta\rangle. \tag{6.33}$$

By calculating molecular orbitals and the eigenvalues of the Fock operator, it is possible to compute the excitation energy and ionized states. It is essential to highlight that the excitation energy is required to promote an electron from a ground state to an excited state. By solving the Fock equation, we can determine the excitation energy from the difference between the eigenvalues of the involved electronic states. These excitation energies are related to molecules' spectroscopic and optical properties [128]. The energy of ionized states refers to the energy required to remove an electron from the molecule, resulting in an ion. The calculation of the eigenvalues of the Fock operator also allows us to estimate these ionization energies [128].

Ionization energy is essential for understanding chemical reactivity and the interactions between molecules and other particles, such as ions and electrons.

Using equation (6.21), the total electronic energy can be obtained as a function of the orbital energies

$$E = \sum_{\alpha} \varepsilon_{\alpha}^{(so)} - \frac{1}{2} \sum_{\alpha,\beta} \langle \alpha\beta \| \alpha\beta \rangle. \tag{6.34}$$

The orbital energies are the eigenvalues of the Fock operator that include the repulsion of a given electron with the others. Thus, the total electron-electron repulsion energy is counted twice by summing the orbital energies. To compensate for this double-counting, it must be subtracted. The same reasoning applies to the exchange energy in the above expression.

It is crucial to highlight that the Fock operator depends on the spin-orbitals, and each spin-orbital is related to each other through an equation that incorporates the Fock operator. Thus, this set of equations must be solved in a coupled manner using an iterative procedure called the self-consistent field (SCF) method. SCF is a numerical technique used to solve problems in quantum physics and quantum chemistry. This method aims to find a stable solution to the equations describing the studied system, considering the average interaction between the particles [62]. The process starts with an initial estimation of the spin-orbitals. Subsequently, the solution undergoes iterative refinement until convergence is attained, meaning that the variances between successive solutions are less than a predetermined threshold. Upon achieving convergence, the self-consistent solution offers a satisfactory depiction of the system under study, encompassing the energies and wave functions of the electrons.

Note that the formulation presented so far has not made any restrictions regarding the molecular orbitals. However, there can be two distinct formulations: the first for systems where each orbital is doubly occupied, and the second, where there is no restriction regarding the spatial parts of the molecular spin-orbitals. For a system where two electrons occupy each molecular orbital, the HF equation can be rewritten with only the spatial parts of the molecular spin-orbitals present, which is called restricted Hartree-Fock (RHF). In a different formulation, unrestricted HF, the molecular spin-orbitals have different spatial parts for different spins.

### 6.2.1 LIMITATIONS AND COMPUTATIONAL COST OF THE HARTREE-FOCK METHOD

The main inherent limitation of the Hartree-Fock method lies in the need for a complete set of basis functions, which must encompass an infinite number of functions. This requirement makes exact calculations unfeasible [68]. In practice, a finite set of basis functions is adopted, selected based on the desired accuracy and acceptable computational cost for the problem at hand [62, 129].

It is important to emphasize that, despite its relative simplicity, the calculation of four-index integrals, represented by $(\langle \alpha\beta | \mu\nu \rangle)$, in the context of the Hartree-Fock method, presents a computational complexity that scales with $N^4$, where $N$ corresponds to the number of basis functions employed. This characteristic poses a considerable challenge since increasing the number of basis functions leads to a substantial increase in the demand for computational resources and processing time required to solve the problem. Thus, a careful analysis must be conducted to balance the desired accuracy with the limitations imposed by the computational cost.

Another limitation is that the Hartree-Fock method treats each electron as if it were in an average field generated by others, lacking detailed electron correlation. Configuration interaction (CI) addresses this by creating Slater determinants from multiple orbital configurations. The CI wavefunction is a linear combination of these determinants, with coefficients adjusted to minimize energy. To obtain good quality one-electron molecular orbitals, a large basis set is used along with optimization of parameters using the variational method. The self-consistent field method is employed to account for electron-electron repulsion, while electron correlation effects are considered using configuration interaction. This involves writing a wavefunction as a series of Slater Determinants involving different configurations, similar to the approach used for atoms.

In many cases, electronic correlation is seen as the numerical correction of the HF solution. Since the HF method assumes that only one Slater determinant can represent the wave function, processes requiring more than one Slater determinant can be interpreted as processes with electronic correlation [130].

Most methods employed in theoretical chemistry for determining the electronic structure use the Hartree-Fock method as a starting point [68]. Electronic correlation is obtained through configuration interaction or perturbative approaches, such as Møller-Plesset perturbation theory,

detailed in the subsequent section. An alternative formulation is Density Functional Theory (DFT), which requires calculating the system's state function [68].

### 6.2.2 MØLLER-PLESSET PERTURBATION THEORY

In this section, we elucidate the perturbative method based on Rayleigh-Schrödinger perturbation theory, proposed by Møller-Plesset (MP) [131], employed as an approach to overcome the challenge of electronic correlation inherent to HF theory. Essentially, this method initially involves solving the unperturbed problem. This usually involves applying HF theory, which provides an approximate solution to the system's wave function and the corresponding energy. The unperturbed solution is then used to apply Rayleigh-Schrödinger perturbation theory. In this context, the perturbation is represented by the electronic interaction that is not considered within the HF theory framework. The perturbation theory is applied iteratively, leading to correction terms of increasing order. These terms are added to the system's energy obtained in the initial step. The sequence of successive approximations is known as the Møller-Plesset series (MPn), where "$n$" indicates the order of the perturbation. In practice, the MPn is typically truncated at a certain order, with MP2 (second order) and MP4 (fourth order) approximations being the most common, due to the significant increase in computational complexity at higher orders [62, 132].

The MP method has been widely used in quantum chemistry and physics. It provides more accurate results than Hartree-Fock theory and helps to better understand the nature of electronic interactions in molecular systems.

### 6.2.2.1 Formalism

The correction to the energy of a many-body system in Møller-Plesset perturbation theory is given through the inclusion of the perturbation potential [62]:

$$\widehat{\mathbf{V}} = \widehat{\mathbf{H}} - \widehat{\mathbf{H}}^{(0)}, \tag{6.35}$$

where $\widehat{\mathbf{H}}$ and $\widehat{\mathbf{H}}^{(0)}$ correspond to the perturbed and unperturbed Hamiltonians, respectively. One way to define the unperturbed Hamiltonian is by using the Fock operator:

$$\widehat{\mathbf{H}}^{(0)} = \sum_{i=1}^{n} \widehat{\mathbf{F}}(i). \tag{6.36}$$

Moreover, let us remember that the definition of the total Hamiltonian $\widehat{\mathbf{H}}$ can be given in terms of kinetic and potential energy:

$$\widehat{\mathbf{H}} = \sum_{i=1}^{n} h(i) + \sum_{i=1}^{n} \sum_{j>i}^{n} \frac{1}{r_{ij}}, \tag{6.37}$$

where $h(i)$ is the sum of the kinetic energies of the electrons and the potential attraction between electrons and nuclei. Now, let's consider again the unperturbed Hamiltonian $\widehat{\mathbf{H}}^{(0)}$ defined by the Fock operator:

$$\widehat{\mathbf{H}}^{(0)} = \sum_{i=1}^{n} \widehat{\mathbf{F}}(i). \tag{6.38}$$

The Fock operator $\widehat{\mathbf{F}}(i)$, as discussed, consists of the one-electron energy terms, along with the Coulomb $\widehat{\mathbf{J}}_{\beta}(i)$ and exchange operators $\widehat{\mathbf{K}}_{\beta}(i)$:

$$\widehat{\mathbf{F}}(i) = h(i) + \sum_{\beta=1}^{n} \left[ \widehat{\mathbf{J}}_{\beta}(i) - \widehat{\mathbf{K}}_{\beta}(i) \right]. \tag{6.39}$$

By substituting the expression for the Fock operator into the equation for the unperturbed Hamiltonian, we have:

$$\widehat{\mathbf{H}}^{(0)} = \sum_{i=1}^{n} \left\{ h(i) + \sum_{\beta=1}^{n} \left[ \widehat{\mathbf{J}}_{\beta}(i) - \widehat{\mathbf{K}}_{\beta}(i) \right] \right\}. \tag{6.40}$$

Now, we can use the expressions for the total and unperturbed Hamiltonians to calculate the perturbation potential $\widehat{\mathbf{V}}$:

$$\widehat{\mathbf{V}} = \left[ \sum_{i=1}^{n} h(i) + \sum_{i=1}^{n} \sum_{j>i}^{n} \frac{1}{r_{ij}} \right] - \left[ \sum_{i=1}^{n} \left\{ h(i) + \sum_{\beta=1}^{n} \left[ \widehat{\mathbf{J}}_{\beta}(i) - \widehat{\mathbf{K}}_{\beta}(i) \right] \right\} \right]. \tag{6.41}$$

Grouping the terms and simplifying the expression, we arrive at the relation:

$$\widehat{\mathbf{V}} = \sum_{i=1}^{n} h(i) + \sum_{i=1}^{n}\sum_{j>i}^{n} \frac{1}{r_{ij}} - \sum_{i=1}^{n} \left\{ h(i) + \sum_{\beta=1}^{n} \left[ \widehat{\mathbf{J}}_\beta(i) - \widehat{\mathbf{K}}_\beta(i) \right] \right\}. \tag{6.42}$$

This is the expression for the perturbation potential $\widehat{\mathbf{V}}$ in Møller-Plesset perturbation theory regarding the Hamiltonian, both perturbed and unperturbed, and their components. The expression (6.42) can be written as:

$$\widehat{\mathbf{V}} = \sum_{i=1}^{n} \left[ \sum_{j>i}^{n} \frac{1}{r_{ij}} - \widehat{\mathbf{V}}^{HF}(i) \right], \tag{6.43}$$

where $\widehat{\mathbf{V}}^{HF}$ is the HF operator given by

$$\widehat{\mathbf{V}}^{HF}(i) = \sum_{\beta=1}^{n} \left[ \widehat{\mathbf{J}}_\beta(i) - \widehat{\mathbf{K}}_\beta(i) \right]. \tag{6.44}$$

The unperturbed system, whose Hamiltonian is given by (6.40), has as its solution the eigenstate $|\psi_0\rangle$, which is the Slater determinant formed by the occupied spin-orbitals. The energy $E_0^{(0)}$ for this problem can be found using [68]:

$$\widehat{\mathbf{H}}^{(0)} |\psi_0\rangle = \sum_{i=1}^{n} \widehat{\mathbf{F}}(i) |\psi_0\rangle = \sum_{i=1}^{n} \varepsilon_i |\psi_0\rangle$$
$$= E_0^{(0)} |\psi_0\rangle. \tag{6.45}$$

where

$$E_0^{(0)} = \sum_{i=1}^{n} \varepsilon_i. \tag{6.46}$$

In this expression, summation is performed for all occupied molecular spin-orbitals. The unperturbed Hamiltonian has as its eigenfunctions the zeroth-order wave functions ($|\psi_0\rangle$), which correspond to the eigenfunctions obtained by the HF method. The other eigenfunctions of $\widehat{\mathbf{H}}^{(0)}$ can be obtained from the set of Slater determinants, formed by replacing one (or more) occupied orbital with one (or more) virtual orbital because this replacement results in a new electronic configuration, which is a linear combination of the Slater determinants corresponding to the original electronic configurations. Therefore, the eigenfunctions corresponding to these new electronic configurations are also eigenfunctions of the unperturbed Hamiltonian. The complete

set of eigenfunctions of $\widehat{\mathbf{H}}^{(0)}$ is composed of the zeroth-order wave functions (corresponding to the ground state) and the wave functions obtained from all possible substitutions of one (or more) occupied orbital with one (or more) virtual orbital [62].

It can be observed that the expression (6.46) does not correspond to the energy obtained in the HF method. The "error" in considering only the zeroth-order term in the energy arises from the fact that when summing the orbital energies, the total electron-electron repulsion energy is counted twice. In this way, the correction can be included through the perturbative potential $\widehat{\mathbf{V}}$, resulting in the expression for the total energy:

$$E_0 = \sum_{i=0} E_0^{(i)} = E_0^{(0)} + E_0^{(1)} + E_0^{(2)} + \dots . \tag{6.47}$$

The expression for the total energy corrected to first order can be obtained from the first-order perturbation equation:

$$E_0^{(1)} = \langle \psi_0 | \widehat{\mathbf{V}} | \psi_0 \rangle, \tag{6.48}$$

where $\widehat{\mathbf{V}}$ is the perturbative operator, representing the total electron-electron repulsion energy. In the Born-Oppenheimer approximation, the expression for $\widehat{\mathbf{V}}$ can be written as:

$$\widehat{\mathbf{V}} = \frac{1}{2} \sum_{\alpha=1}^{n} \sum_{\beta=1}^{n} \langle \alpha\beta | \alpha\beta \rangle, \tag{6.49}$$

where $\langle \alpha\beta | \alpha\beta \rangle$ is the Coulomb integral, representing the electrostatic interaction between the electrons in the molecular orbitals $\alpha$ and $\beta$. Note that the sum is performed only over the occupied orbitals in the expression above to avoid counting the electron-electron repulsion energy twice.

Substituting the expression for $\widehat{\mathbf{V}}$ into the first-order perturbation equation, we obtain:

$$E_0^{(1)} = \frac{1}{2} \sum_{\alpha=1}^{n} \sum_{\beta=1}^{n} \langle \alpha\beta | \alpha\beta \rangle. \tag{6.50}$$

Therefore, the total energy corrected to first order can be written as:

$$E_0 = E_0^{(0)} + E_0^{(1)} = \sum_{i=1}^{n} \varepsilon_i - \frac{1}{2} \sum_{\alpha=1}^{n} \sum_{\beta=1}^{n} \langle \alpha\beta | \alpha\beta \rangle. \tag{6.51}$$

where the first term corresponds to the Hartree-Fock energy (zeroth order), and the second term

corresponds to the first-order correction due to the electron-electron repulsion energy.

The expression for the total energy corrected to first order is identical to that obtained in the HF method. This means the HF method is valid up to the first order in the Møller-Plesset perturbation theory. However, perturbation theory up to the first order (MP1) does not provide additional information compared to the Hartree-Fock method. The contribution of electronic correlation only becomes evident from higher-order terms. In other words, including electronic correlation is necessary to explain the effects of electron interaction on the total energy of the molecule. However, this is only possible from higher-order terms in Møller-Plesset perturbation theory. Thus, to improve the energy obtained by the HF method, electronic correlation, which is given from the second-order term, must be included [68].

$$
\begin{aligned}
E_0^{(2)} &= \sum_{\alpha \neq \lambda, \beta \neq \mu} \frac{\left| \left\langle \psi_0 | \widehat{\mathbf{V}} | \psi_{\alpha\beta}^{\lambda\mu} \right\rangle \right|^2}{\varepsilon_\alpha + \varepsilon_\beta - \varepsilon_\lambda - \varepsilon_\mu} \\
&= \sum_{\alpha \neq \lambda, \beta \neq \mu} \frac{|\langle \alpha\beta || \lambda\mu \rangle|^2}{\varepsilon_\alpha + \varepsilon_\beta - \varepsilon_\lambda - \varepsilon_\mu},
\end{aligned}
\tag{6.52}
$$

where $\left| \psi_{\alpha\beta}^{\lambda\mu} \right\rangle$ represents the state corresponding to a double excitation and the occupied states $\alpha$ and $\beta$ are replaced by virtual orbitals $\lambda$ and $\mu$, respectively; $\varepsilon_\alpha, \varepsilon_\beta, \varepsilon_\lambda$ and $\varepsilon_\mu$ are the energies of the occupied orbitals $\alpha$ and $\beta$ and the virtual orbitals $\lambda$ and $\mu$, respectively.

When using the correction up to the second order, the perturbative method is called the Møller-Plesset perturbation theory of the second order, or simply MP2. The total energy of the molecule in the MP2 method is given by the sum of the zero-order energy (obtained by the Hartree-Fock method), the first-order correction due to electron-electron repulsion energy, and the second-order correction due to electron-electron interaction. The expression for the total energy is given by:

$$
E_0 = E_0^{(0)} + E_0^{(1)} + E_0^{(2)} \quad = \sum_{i=1}^{n} \varepsilon_i - \frac{1}{2} \sum_{\alpha=1}^{n} \sum \sum \beta = 1^n \langle \alpha\beta | \alpha\beta \rangle + \sum_{\alpha \neq \lambda, \beta \neq \mu} \frac{|\langle \alpha\beta | \lambda\mu \rangle|^2}{\varepsilon_\alpha + \varepsilon_\beta - \varepsilon_\lambda - \varepsilon_\mu}.
\tag{6.53}
$$

In the above expression, the first term corresponds to the Hartree-Fock energy (zero-order), the second term corresponds to the first-order correction due to electron-electron repulsion energy, and the third term corresponds to the second-order correction due to electron-electron

interaction. The second-order term represents corrections to the total energy from the interaction between two electrons in different orbitals.

## 6.3 Density Functional Theory in Molecular Systems

Since the beginning of the section, the investigation has focused on analyzing the electronic structure of molecular systems. To address the problem of $n$ bodies, the Hartree-Fock (HF) method utilizes a simplification that allows considering $n$ one-body problems. In this approach, the main object of study is the total wave function $\Phi$ that depends on the coordinates of the $n$ electrons. The Møller-Plesset Perturbation Theory, which aims to correct the absence of electronic correlation in the HF method, was previously presented. MP1 theory is the first correction to the total energy of the molecule, taking into account the electron-electron repulsion energy. MP2 theory includes an additional correction due to the interaction between electrons in different orbitals.

The HF method is capable of providing satisfactory results for electronic correlation energy. However, treating considerably large molecular systems, such as those composed of about 20 atoms, can become highly complex due to the high computational cost. To address this difficulty, Density Functional Theory (DFT) was proposed in 1964 by physicists P. Hohenberg and W. Kohn [133]. This method, based on the concepts of the Thomas-Fermi model, formulates the many-electron problem in terms of electron density. From this perspective, the search for a wave function with $3n$ variables is replaced by the search for electron density with only three variables [125, 134].

In the present section, the formulation of Density Functional Theory (DFT) will be detailed, given its vast applicability in treating molecular systems [125, 126, 135, 136]. DFT enables treating systems of considerable size with satisfactory accuracy and lower computational cost compared to post-Hartree-Fock methods [68].

### 6.3.1 Formalism

The problem at hand refers to a system of $n$ electrons interacting. When the Born-Oppenheimer approximation is assumed, the Schrödinger equation for the electronic problem is expressed as follows [137]:

$$\widehat{\mathbf{H}}_e\psi\left(\{\mathbf{r}_i\}\right) = \left[\widehat{\mathbf{T}}_e + \widehat{\mathbf{U}}_{eN} + \widehat{\mathbf{U}}_{ee}\right]\psi\left(\{\mathbf{r}_i\}\right) = E_e\psi\left(\{\mathbf{r}_i\}\right). \tag{6.54}$$

In this equation, $\psi\left(\{\mathbf{r}_i\}\right)$ is the electronic wave function, which depends on the coordinates of the $n$ electrons in the system. The electronic Hamiltonian, $\widehat{\mathbf{H}}_e$, is composed of the following terms: $\widehat{\mathbf{T}}_e$, which describes the motion of electrons in the system; $\widehat{\mathbf{U}}_{eN}$, which represents the interaction of electrons with the atomic nuclei of the system; and $\widehat{\mathbf{U}}_{ee}$, the electron-electron potential, which describes the interaction of electrons with each other. Note that in the notation, the dependence of the wave function $\psi\left(\{\mathbf{r}_i\}\right)$ on the nuclear coordinates $\mathbf{R} = \{\mathbf{r}_\alpha\}$ has been omitted because, in the Born-Oppenheimer approximation, the Schrödinger equation separates the electronic and nuclear variables, so the nuclear coordinates are considered external parameters for the electronic problem. The electron density is defined as:

$$\rho(\mathbf{r}) = N \int \psi^*\left(\{\mathbf{r}_i\}\right)\psi\left(\{\mathbf{r}_i\}\right) d^3\mathbf{r}_2 d^3\mathbf{r}_3 \ldots d^3\mathbf{r}_n. \tag{6.55}$$

The total energy of the system is given by:

$$E_0 = \left\langle \psi\left(\{\mathbf{r}_i\}\right)\left|\left(\widehat{\mathbf{T}}_e + \widehat{\mathbf{U}}_{eN} + \widehat{\mathbf{U}}_{ee}\right)\right|\psi\left(\{\mathbf{r}_i\}\right)\right\rangle. \tag{6.56}$$

DFT is based on two theorems proposed by Hohenberg and Kohn [133] stated as:

**Theorem 1 (First Hohenberg-Kohn Theorem).** The external potential felt by the electrons is a unique functional of the electron density $\rho(\mathbf{r})$.

This allows us to use the electron density as an alternative description of the system instead of the wave function $\psi$, which is more difficult to obtain and manipulate.

Therefore, the fact that the external potential felt by the electrons is a unique functional of the electron density implies that the electron density contains all the information necessary to characterize the system's ground state. This is an important simplification in the description of the many-electron system, as it allows the system's physical properties to be expressed in terms of a single variable.

**Theorem 2 (Second Hohenberg-Kohn Theorem).** The ground state energy $E[\rho]$ is minimal for the exact density $\rho(\mathbf{r})$.

Proof: Let $\rho' = \rho'(\mathbf{r})$ be a density for a given state $\psi'$ and $\rho$ the density for the ground state $\psi$. In this way,

$$E[\rho'] = \left\langle \psi' | \widehat{\mathbf{H}} | \psi' \right\rangle = \left\langle \psi' \left| \left( \widehat{\mathbf{T}}_e + \widehat{\mathbf{U}}_{eN} + \widehat{\mathbf{U}}_{ee} \right) \right| \psi' \right\rangle$$
$$E[\rho] = \left\langle \psi | \widehat{\mathbf{H}} | \psi \right\rangle = \left\langle \psi \left| \left( \widehat{\mathbf{T}}_e + \widehat{\mathbf{U}}_{eN} + \widehat{\mathbf{U}}_{ee} \right) \right| \psi \right\rangle \tag{6.57}$$

Through the variational theorem, it is easy to show that.

The inequality $E[\rho] \leq E[\rho']$ means that the energy functional $E[\rho]$ is minimal when the electron density is equal to the actual electron density of the system $\rho'$. Equality holds only if $\rho = \rho'$. The functional to be calculated in DFT is given by:

$$E[\rho] = U_{eN}[\rho] + U_{ee}[\rho] + T[\rho], \tag{6.58}$$

or,

$$E[\rho] = \int \rho(\mathbf{r}) v(\mathbf{r}) d^3\mathbf{r} + \frac{1}{2} \iint \frac{\rho(\mathbf{r})\rho(\mathbf{r}')}{|\mathbf{r} - \mathbf{r}'|} d^3\mathbf{r} d^3\mathbf{r}' + G[\rho], \tag{6.59}$$

where $G[\rho]$ is a universal functional of the density. Kohn and Sham [138] proposed a first approximation for the functional $G[\rho]$, defining it as

$$G[\rho] \equiv T_0[\rho] + E_{xc}[\rho], \tag{6.60}$$

where $T_0[\rho]$ is the kinetic energy of a system of non-interacting electrons with density $\rho(\mathbf{r})$ and $E_{xc}[\rho]$ is the exchange-correlation energy of an interacting system with density $\rho(\mathbf{r})$. The exact formulation for the exchange-correlation energy functional $E_{xc}[\rho]$ in DFT is complex due to the Schrödinger equation's non-linear nature and the system's electron-electron interaction. Different approximations and methods are used to address the exchange-correlation term, each with its own limitations and advantages in terms of efficiency and accuracy [139]. It is important to note that the second term in (6.59) is an approximation for the electron-electron interaction term that includes only the classical interaction between electronic densities. The potential energy written in this form includes self-interaction, that is, the interaction energy of an electron with itself, as electronic correlation has been eliminated from this term. It can also be noted that the exchange term is excluded in this approximation.

The energy functional (6.59) to be minimized is subject to the constraint.

$$\int \rho(\mathbf{r})d^3\mathbf{r} = N, \tag{6.61}$$

which means that the total electronic charge is fixed.

Using the variational principle, one can write [68]:

$$\delta \left\{ E[\rho] - \mu \left[ \int \rho(\mathbf{r})d^3\mathbf{r} - N \right] \right\} = 0. \tag{6.62}$$

Given a density functional $F[\rho]$, the functional derivative of $F[\rho]$ with respect to a small variation in the density $\delta\rho(\mathbf{r})$ is defined as

$$\delta F[\rho]/\delta\rho(\mathbf{r}) = F[\rho(\mathbf{r}) + \delta\rho(\mathbf{r})] - F[\rho(\mathbf{r})] = \int \frac{\delta F[\rho]}{\delta\rho(\mathbf{r})}\delta\rho(\mathbf{r})d^3\mathbf{r}. \tag{6.63}$$

In this way, using (6.59) the expression obtained is

$$\int \delta\rho(\mathbf{r}) \left\{ v(\mathbf{r}) + \int \frac{\rho(\mathbf{r}')}{|\mathbf{r} - \mathbf{r}'|}d^3\mathbf{r}' + \frac{\delta T_0}{\delta\rho} + v_{xc}[\rho] - \mu \right\} d^3\mathbf{r} = 0, \tag{6.64}$$

where

$$v_{xc}[\rho] = \frac{\delta E_{xc}}{\delta\rho}. \tag{6.65}$$

Assuming that the electron density can be written as

$$\rho(\mathbf{r}) = \sum_{i=1}^{n} |\psi_i(\mathbf{r})|^2, \tag{6.66}$$

we have:

$$H^{KS}\psi_i(\mathbf{r}) = \left( -\frac{1}{2}\nabla^2 + v^{KS}[\rho] \right) \psi_i(\mathbf{r}) = \varepsilon_i\psi_i(\mathbf{r}), \tag{6.67}$$

where $v^{KS}[\rho]$ is the Kohn-Sham (KS) effective potential given by

$$v^{KS} = v(\mathbf{r}) + \int \frac{\rho(\mathbf{r}')}{|\mathbf{r} - \mathbf{r}'|}d^3\mathbf{r}' + v_{xc}[\rho]. \tag{6.68}$$

Equation (6.67) is called the Kohn-Sham (KS) equation, and it arises with the aid of the Schrödinger equation for a particle. We have that $\psi_i(\mathbf{r})$ is the wave function of the $i$-th electron and $\varepsilon_i$ is the energy of the $i$-th electronic state. The KS effective potential, $v^{KS}[\rho]$, is given

by the sum of the external potential, $v(\mathbf{r})$, with the three-dimensional Coulomb integral of the electron density, $\rho(\mathbf{r'})$, and the exchange-correlation potential functional, $v_{xc}[\rho]$. The exchange-correlation potential functional, $v_{xc}[\rho]$, is obtained by varying the exchange-correlation energy functional, $E_{xc}$, concerning the electron density, $\rho$.

It is noted that the KS effective potential depends on the electron density, which, in turn, is calculated from the solutions of the KS equations. Therefore, solving the KS equations must be done in a self-consistent manner, that is, iteratively, similar to the Hartree-Fock method. The KS effective potential, $v^{KS}[\rho]$, has a mathematically similar form to the potential of the Thomas-Fermi model but is adjusted to reproduce the energies and densities of the real electronic states of the system [140].

To find the total electronic energy, one must calculate

$$\sum_{i=1}^{n} \int \varepsilon_i \psi_i(\mathbf{r})\psi_i^*(\mathbf{r})d^3\mathbf{r} = T_0[\rho] + \int \left[v(\mathbf{r}) + v_{xc}(\mathbf{r})\right]\rho(\mathbf{r})d^3\mathbf{r} + \iint \frac{\rho(\mathbf{r'})\rho(\mathbf{r})}{|\mathbf{r}-\mathbf{r'}|}d^3\mathbf{r}d^3\mathbf{r'}, \quad (6.69)$$

where $T_0 = -\frac{1}{2}\sum_i \int \psi_i^*\nabla^2\psi_i d^3\mathbf{r}$ was considered. Thus, using (6.59), it is possible to arrive at the following expression for the total electronic energy of the system:

$$E[\rho] = \sum_{i=1}^{n} \varepsilon_i - \frac{1}{2}\iint \frac{\rho(\mathbf{r'})\rho(\mathbf{r})}{|\mathbf{r}-\mathbf{r'}|}d^3\mathbf{r}d^3\mathbf{r'} + E_{xc} - \int v_{xc}(\mathbf{r})\rho(\mathbf{r})d^3\mathbf{r}. \quad (6.70)$$

Equation (6.70) represents the total energy functional $E[\rho]$ of the electron system, expressed in terms of the electron density $\rho(\mathbf{r})$, the eigenvalues $\varepsilon_i$, and the exchange-correlation potential $E_{xc}$. Thus, the first term on the right-hand side of the equation represents the total kinetic energy of the electrons. In contrast, the second term represents the Coulomb interaction potential energy between the electrons. The third term represents the exchange-correlation energy, while the last term is the potential energy of the system due to interaction with the external potential.

### 6.3.1.1 Physical Meaning of the Kohn-Sham Orbital Energies

The work of Janak [141], titled "Proof that $\epsilon_i$ is the energy derivative of the density," published in 1978, demonstrated that the eigenvalues $\varepsilon_i$ of the Kohn-Sham (KS) equation are the derivatives concerning the electron density $\rho(\mathbf{r})$ of the system's total energy $E[\rho]$, i.e., $\varepsilon_i = \frac{\partial E[\rho]}{\partial \rho_i}$. This result

is significant because it provides a clear physical interpretation of the eigenvalues of the KS equation and allows the theory to be applied to determine properties of electronic systems in thermodynamic equilibrium, such as ionization energy and electron affinity. In his work, Janak defines the kinetic energy functional as:

$$T_0[\rho] = \sum_{i=1}^{n} t_i, \tag{6.71}$$

where $t_i$ is given by:

$$t_i = -\frac{1}{2} \int \psi_i^* \nabla^2 \psi_i d^3\mathbf{r} = \varepsilon_i - \int \psi_i^* \left( v^{KS}[\rho] \right) \psi_i d^3\mathbf{r}. \tag{6.72}$$

Thus, $t_i$ is obtained from the self-consistent solution of the KS equation for $n$ electrons, and $T_0[\rho]$ is obtained in terms of the $n$ solutions of the KS equation. Janak defined the charge density as a function of the occupation number $n_i$ of each orbital $\psi_i$, i.e.,

$$\rho(\mathbf{r}) = \sum_{i=1}^{n} n_i \left| \psi_i(\mathbf{r}) \right|^2, \tag{6.73}$$

$n_i$ is a parameter that takes non-integer values. Thus, the functional is defined as

$$\tilde{T}[\rho] \equiv \sum_{i=1}^{n} n_i t_i, \tag{6.74}$$

which provides the following energy:

$$\tilde{E}[\rho] \equiv \tilde{T}[\rho] + U_{eN}[\rho] + U_{ee}[\rho] + E_{xc}[\rho], \tag{6.75}$$

where the functionals $U_{eN}[\rho], U_{ee}[\rho]$, and $E_{xc}[\rho]$ depend on the occupation numbers $n_i$ through equation (6.73). The obtained result, $\frac{\partial \tilde{E}}{\partial n_i} = \varepsilon_i$, does not depend on the form of the exchange-correlation functional $E_{xc}[\rho]$. This means that the validity of this expression is independent of the choice of the exchange-correlation functional, which is a crucial part of the Kohn-Sham method. This is an important result because it shows that the relationship between the eigenvalues of the Kohn-Sham states and the electronic occupations is a general property of the method, valid regardless of the choice of the exchange-correlation functional. This also suggests that the eigenvalues of the Kohn-Sham states can be interpreted as independent particle energies, which

is one of the basic premises of the model.

Consider the variation of $\tilde{E} \equiv \tilde{E}[\rho]$ with respect to $n_i$,

$$\frac{\partial \tilde{E}}{\partial n_i} = t_i + \sum_{j \neq i} n_j \frac{\partial t_j}{\partial n_i} + \int v(\mathbf{r}) \frac{\partial \rho(\mathbf{r})}{\partial n_i} d^3\mathbf{r} + \iint \frac{\partial \rho(\mathbf{r})}{\partial n_i} \frac{\rho(\mathbf{r'})}{|\mathbf{r} - \mathbf{r'}|} d^3\mathbf{r} d^3\mathbf{r'} + \int \frac{\delta E_{xc}}{\delta \rho} \frac{\partial \rho}{\partial n_i} d^3\mathbf{r}. \quad (6.76)$$

It is possible to obtain, Appendix C, the expression

$$\frac{\partial \tilde{E}}{\partial n_i} = \varepsilon_i. \quad (6.77)$$

Through equation (6.77), which provides the connection between the ground states of a system with $N$ and $(N + 1)$ particles through the introduction of $n(0 \leq n \leq 1)$ electrons into the lowest unoccupied level, one can obtain the relation [68]:

$$E_{N+1} - E_N = \int_0^1 \varepsilon_i(n) dn. \quad (6.78)$$

In order to calculate the integral above, it is imperative to possess knowledge of the eigenvalues of the highest occupied orbital of a system with $N + 1$ particles, $\varepsilon_i(n)$, for all values of $n$ within the range of 0 to 1. This calculation can be carried out through approximations for $\varepsilon_i(n)$ [68].

It is essential to highlight that Almbladh and von Barth showed that, for any finite system (such as atoms or molecules), the last occupied eigenvalue of DFT, denoted as $\varepsilon_+$, is equal to the exact ionization energy for the exact exchange-correlation functional $E_{xc}$. Equation (6.79) expresses this relationship, where $E(N)$ is the total energy of the system with $N$ electrons and $E(N - 1)$ is the total energy of the system with $N - 1$ electrons.

$$\varepsilon_+ = E(N) - E(N - 1). \quad (6.79)$$

This relationship is essential because, even if the KS orbital energies do not have a clear physical meaning, the ionization energy is a well-defined physical quantity of great interest in various applications. Thus, this relationship allows the ionization energy obtained from DFT results. However, we emphasize that the accuracy of this result depends on the choice of the exchange-correlation functional used in DFT.

One of the main advantages of density functional theory (DFT) is its scalability, which is proportional to $N^3$, where $N$ represents the number of basis functions required to represent the Kohn-Sham (KS) orbitals. Compared to the Hartree-Fock (HF) method, the computational cost of DFT is reduced by a factor of $N$, resulting in a significantly lower computational cost than other post-HF methods [68]. This characteristic makes DFT a powerful tool for studying complex systems with many electrons.

## 6.4 USING DFT TO CALCULATE SPECTROSCOPIC PROPERTIES OF MOLECULES

In the previous sections it was addressed the use of Density Functional Theory (DFT) for computing the spectral characteristics of molecules and explains the main components of the Kohn-Sham energy expressions. In this framework, it is reasonable to consider electrons in atoms or molecules as independent particles moving within an effective potential $v_{KS}(\mathbf{r})$. This effective potential incorporates all the complexities of the electron-electron interactions into a single potential function.

The evolution of exchange-correlation functionals can be conceptualized as a series of approximations, often depicted as Jacob's Ladder, each rung representing a higher level of approximation aimed at improving the accuracy of $E_{xc}$. The earliest and most straightforward of these is the Local Spin Density Approximation (LSDA), which is based on the spin-density functional for the exchange-correlation energy [138].

$$E_{xc}^{LSD}[n_\uparrow, n_\downarrow] = \int d^3\mathbf{r}\, n\varepsilon_{xc}^{unif}(n_\uparrow, n_\downarrow),\qquad(6.80)$$

where $\varepsilon_{xc}^{unif}(n_\uparrow, n_\downarrow)$ is the exchange-correlation energy of each particle in an electron gas with uniform spin densities $n_\uparrow$ and $n_\downarrow$, known from quantum Monte Carlo calculations and other many-electron methods [142]. The next rung on Jacob's Ladder is the generalized gradient approximation (GGA) method [136, 143, 144]:

$$E_{xc}^{GGA}[n_\uparrow, n_\downarrow] = \int d^3\mathbf{r}\, n\varepsilon_{xc}^{GGA}(n_\uparrow, n_\downarrow, \nabla n_\uparrow, \nabla n_\downarrow),\qquad(6.81)$$

where the gradients of the spin densities $\nabla n_\uparrow(\mathbf{r})$ and $\nabla n_\downarrow(\mathbf{r})$ are additional arguments of $\varepsilon_{xc}^{GGA}$. Frequently used functionals of this class include PBE [143] and PW91 [145].

Adding the next set of local arguments yields meta-GGA [146, 147], or the so-called third rung of Jacob's Ladder:

$$\mathrm{E}_{xc}^{MGGA}\left[n_\uparrow, n_\downarrow\right] = \int d^3\mathbf{r} n\varepsilon_{xc}^{MGGA}\left(n_\uparrow, n_\downarrow, \nabla n_\uparrow, \nabla n_\downarrow, \nabla^2 n_\uparrow, \nabla^2 n_\downarrow, \tau_\uparrow, \tau_\downarrow\right). \tag{6.82}$$

The appearance of the Laplacian $\nabla^2 n_\sigma(r)$ is logical when "ascending" the ladder in the fourth-order gradient expansion. The Kohn-Sham orbital kinetic energy densities are represented as:

$$\tau_\sigma = \frac{1}{2}\sum_i^{\mathrm{occ}} |\nabla\psi_{i\sigma}(\mathbf{r})|^2. \tag{6.83}$$

They appear in the Taylor expansion of the exchange hole density around $|r' - r| = 0$. An example of a non-empirical meta-GGA is the TPSS functional.

The fourth rung adds a computationally expensive non-local orbital functional

$$\varepsilon_{x\sigma}(\mathbf{r}) = \frac{1}{2}\int d^3\mathbf{r}' \frac{n_x^\sigma(\mathbf{r}, \mathbf{r}')}{|\mathbf{r}' - \mathbf{r}|} = -\frac{1}{2n_\sigma(r)}\int d^3\mathbf{r}' \frac{|\sum_i^{occ} \psi_{i\sigma}^*(\mathbf{r})\psi_{i\sigma}(\mathbf{r}')|^2}{|\mathbf{r}' - \mathbf{r}|}. \tag{6.84}$$

Alternatively, its analog represents the exact exchange energy found using it. Thus, hyper-GGA [148] can be represented as

$$\mathrm{E}_{xc}^{\mathrm{HGGA}}\left[\mathrm{n}_\uparrow, \mathrm{n}_\downarrow\right] = \int d^3\mathbf{r}\varepsilon_{xc}^{\mathrm{HGGA}}\left(\mathrm{n}_\uparrow, \mathrm{n}_\downarrow, \nabla \mathrm{n}_\uparrow, \nabla \mathrm{n}_\downarrow, \tau_\uparrow, \tau_\downarrow, \varepsilon_\uparrow, \varepsilon_\downarrow\right). \tag{6.85}$$

Semi-empirical hyper-GGAs include widely used hybrid functionals such as B3LYP [149], B3PW91 [148], and PBE0 [150], in which the contributions of Hartree-Fock and GGA exchange are fixed.

Jacob's ladder's fifth and final rung uses all Kohn-Sham orbitals, both occupied and unoccupied. The Random Phase Approximation [151] operates at this level.

### 6.4.1 HYBRID FUNCTIONAL CAM-B3LYP

Hybrid functionals improve the approximation of the exchange and correlation (XC) energy component of the total energy of the electron system, compared to LSD and GGA, which account

only for electron density (the 1st and 2nd rungs of Jacob's Ladder).

Hybrid functionals enhance the overall energy estimation by using electron density and individual electronic wave functions to compute the total energy. The exchange part of the XC energy is calculated more or less accurately from electronic wave functions and is introduced with different weights with LSD or GGA energy. This improvement comes at a computational cost of 10-100 times higher compared to LSD or GGA.

Next, we consider the hybrid functional CAM-B3LYP applied in this work [152], which belongs to the fourth rung of the Jacob above's ladder.

Let us describe the B3LYP component of the functional. It is also a hybrid functional of exact exchange with LSDA and GGA correlation terms, proposed by Becke [148]:

$$\mathrm{E_{xc}} = (1 - \mathrm{a_0})\, \mathrm{E_x^{LSDA}} + \mathrm{a_0 E_x^{HF}} + \mathrm{a_x \Delta E_x^{B88}} + \mathrm{E_c^{LSDA}} + \mathrm{a_c \Delta E_c^{PW91}}, \qquad (6.86)$$

where $\Delta\mathrm{E_x^{B88}}$ is Becke's gradient correction for the exchange functional, and $\Delta\mathrm{E_c^{PW91}}$ is the Perdew-Wang gradient correction for the correlation functional [143]. The functional coefficients were determined based on the heats of formation of small molecules, with the values set as follows: $\mathrm{a_0} = 0.2$, $\mathrm{a_x} = 0.72$, and $\mathrm{a_c} = 0.81$. Specifically, only energies at a point were considered for parameter fitting, with no considerations for geometries or frequencies. Despite its success in many applications, the B3LYP functional was unsuitable in some cases: 1) polarizability of long chains, 2) excitation using time-dependent DFT for Rydberg states, 3) charge-transfer excitations [153–156]. The problem was that at long distances, the exchange potential behaved as $-0.2r^{-1}$ instead of the exact $-r^{-1}$. In [157], this problem was resolved by introducing the Ewald splitter for $r_{12}^{-1}$ as

$$\frac{1}{r_{12}} = \frac{1 - \mathrm{erf}\,(\mu r_{12})}{r_{12}} + \frac{\mathrm{erf}\,(\mu r_{12})}{r_{12}}. \qquad (6.87)$$

The first term accounts for short-range interactions, and the second is for long-range interactions. It is crucial to remember that the long-range-corrected (LC) functional scheme [158, 159] incorporates the DFT exchange interaction within the short-range interaction. In contrast, the Hartree-Fock exchange integral defines the long-range orbital-orbital interaction through an additional term.

In the work where the CAM-B3LYP functional was introduced [152], formula 6.87 with two

parameters $\alpha$ and $\beta$ was generalized to

$$\frac{1}{r_{12}} = \frac{1 - [\alpha + \beta \operatorname{erf}(\mu r_{12})]}{r_{12}} + \frac{\alpha + \beta \operatorname{erf}(\mu r_{12})}{r_{12}}, \quad (6.88)$$

where the conditions $0 \leq \alpha + \beta \leq 1, 0 \leq \alpha \leq 1$, and $0 \leq \beta \leq 1$ are met. The abbreviation CAM stands for the Coulomb-attenuating method, indicating the modification of the Coulomb interaction correction with increasing inter-electron distance. The flexibility of the functional provided by the parameters $\alpha$ and $\beta$ allows the assessment of the contribution of Hartree-Fock (HF) exchange in the short-range region and the DFT part in the long-range region. For instance, with $\alpha = 0.0$ and $\beta = 1.0$, we obtain the LC functional, and with $\alpha = 0.2$ and $\beta = 0.0$, we reproduce the B3LYP functional.

The ability to adjust the contributions from DFT and HF allowed the optimization of coefficients $\alpha = 0.19$ and $\beta = 0.46$ [152], enabling the description of charge-transfer excitations and providing additional impetus for the development of hybrid functionals.

The use of the CAM-B3LYP functional for absorption spectra calculations, including modeling the shape of the band, is presented in works [160, 161], including on a group of conjugated polymers in [162].

## 6.5 BASIS SETS

### 6.5.1 CLASSIFICATION OF BASIS SETS

When it comes to non-empirical quantum chemical calculations, basis sets can be organized into different categories based on various criteria. One common way to classify them is by the number of independent basis functions used to characterize the motion of electrons and form an orbital [163].

Minimal basis sets are those in which each electron in an isolated atom, i.e., its one-electron function-orbital, is described by only one independent basis function. Such a function may be a Slater-type function, acting in this case as STO. In turn, STO can be described by a linear combination of GTF.

For example, for a carbon atom, a second-period element, the minimal basis set contains five basis functions. In this case, the independent basis function is the atomic orbital. In a minimal

basis set, each of these orbitals will be represented by a single basis function. The minimal basis set in this example contains two 5-type basis functions (1s and 2s) and one set ( $2p_x, 2p_y, 2p_z$ ) of p-type functions. Each basis function is approximated by its group of Gaussian functions. Therefore, it is designated as the [251p] basis set.

Note that the notation [251p] signifies that the 1s orbital is represented by a combination of 2 Gaussian functions, the 2s orbital is represented by a combination of 5 Gaussian functions, and each of the 2p orbitals is represented by a single Gaussian function.

Another type of minimal basis set uses N Gaussian-type functions to describe one STO and is denoted as STO-NG. The resulting set of coefficients for decomposing STO into GTF and the exponent values of GTF are normalized to a unit value of the STO exponent. When approximating a STO using multiple GTF, we need to calculate coefficients that effectively replicate the shape of the STO. These coefficients ensure that the combination of GTFs closely resembles the STO. Both Slater orbitals and GTFs have decay parameters that govern the rate of decay as the function moves away from the atomic nucleus. To accurately represent the STO, the exponents of the GTFs are adjusted (normalized) so that the combined GTFs maintain the decay characteristics of the original STO.

When attempting to approximate a Slater-type 1s orbital (STO-1s) using 3 Gaussian functions (STO-3G), the approach involves selecting 3 GTFs with varying decay parameters to replicate the shape of the STO orbital. Coefficients are then calculated for each GTF to achieve a weighted sum that closely resembles the STO orbital. Finally, the decay parameters of the GTFs are adjusted to ensure that the combined functions accurately capture the exponential decay characteristics of the original STO.

The use of minimal basis sets is prevalent in the description of multi-electron systems and the representation of molecular geometries. They are particularly advantageous in the computation of large molecular systems and those incorporating heavy element atoms due to their efficient use of computational resources. However, minimal basis sets exhibit limitations in adequately portraying energy characteristics [164]. This deficiency stems from their inability to adapt to the varying atomic environment within a molecule, resulting in a lack of flexibility in accounting for orbital polarization and relaxation.

### 6.5.2 DOUBLE-EXPONENTIAL BASIS SETS

Double-exponential (Double Zeta - DZ) or split basis sets describe each type of electron with two independent functions. One of the functions for which the probability density of finding an electron of this type is closer to the atomic nucleus is called the inner (or contracted) function, and the other, for which the probability density is farther from the nucleus, is the outer (diffuse) function [163]. Such a set contains 10 independent functions or five split orbitals for a second-period element atom.

**Table 1** – *DZ basis set for a second-period element atom.*

| Orbital: | $\psi_1$ | $\psi_2$ | $\psi_3$ | $\psi_4$ | $\psi_5$ |
|---|---|---|---|---|---|
| Independent functions: | $1s', 1s''$ | $2s', 2s''$ | $2p_x', 2p_x''$ | $2p_y', 2p_y''$ | $2p_z', 2p_z''$ |

Each orbital is represented by a linear combination of two basis functions (BF). The first electron, for example, is a linear combination of the inner (1 s') and outer (1 s") basis functions:

$$\psi_1 = c_1 \left(1s'\right) + c_2 \left(1s''\right).$$

The coefficients $c_1$ and $c_2$ are determined by minimizing the atom's electronic energy. Therefore, the orbital in a DZ basis set exhibits some flexibility concerning its size. This is achieved using the variational principle by varying the relative contribution of the inner and outer BFs to the orbital, which has an intermediate position between the basis functions.

The described sets provide a more precise description of the geometric structure, electronic distribution, and molecular properties compared to minimal basis sets. Nevertheless, there is still room for improvement in the energetic characteristics, even when considering electronic correlation [165]. This is due to incomplete accounting for orbital relaxation and the omission of polarization effects. In summary, double-exponential basis sets are adequate for providing a qualitative description of multi-electron systems.

Basis sets that use two independent functions to describe the motion of only valence electrons are widely used [166, 167]. For inner electron shells, a minimal basis set is retained, leading to savings in computer resources. These basis sets are called valence-split (Split-Valence - SV or Double Zeta Valence - DZP). They include sets, using the notation, like $M - NP$G. For

example, for second-period elements, each inner orbital is described by one function - a linear combination of $M$ Gaussian functions, while valence 2s- and 2p-orbitals are represented by two sets of independent functions consisting of $NP$ Gaussian functions, but with different values of the orbital exponents and contraction coefficients. For example, the $6-31G$ basis set describes each inner (1s) orbital with six GTFs, the valence 2s orbital with three different and grouped GTFs with one set of grouping coefficients and one GTF with another exponent value, each valence 2p orbital with the same three GTFs as for the 2s-electron but with a different set of grouping coefficients, and one GTF as for the 2s-electron. This basis set for carbon can be denoted as: [3s, 2p], or (631,31).

### 6.5.3 EXTENDED BASIS SETS

These extended basis sets consist of three independent functions for each type of electron - triple-exponential (Triple Zeta - TZ), quadruple-exponential (Quadruple Zeta - QZ), and so on [163].

As with split basis sets, there are valence-extended basis sets in which only the valence electrons are described by three or more independent functions. An example of such a set is the $6-311G$ basis set, where each valence electron is described by three functions, approximated by three, one, and one Gaussian functions.

Using extended basis sets allows for orbital relaxation without optimizing the parameters of the basis functions and achieves this more entirely as the set expands. Such basis sets can be used to obtain quantitatively suitable results on the electronic structure of multi-electron systems. This is because the additional basis functions provide more flexibility in capturing variations in the shape and energy of the orbitals.

### 6.5.4 POLARIZATION AND DIFFUSE FUNCTIONS

It is essential to include additional polarization functions for valence electrons in basis sets to account for changes in the shape of a basis orbital during chemical bond formation. These polarization functions have higher orbital quantum numbers compared to valence electron functions. For instance, a p-function is used as a polarization function for s-electrons, a d-function for p-electrons, along with others. Thus, the polarization functions for H, B, S, and Fe atoms are

1p, 2d, 3d, and 3f, respectively. The presence of a polarization function in a basis set is indicated by an asterisk ("*") or by specifying the type of polarization function in parentheses. Widely used basis sets of this type include, for example, the $6-31G*$ and $6-31G**$ basis sets. One asterisk means adding a polarization $d$-GTF to the $s$- or $p$-elements of the second or third period, and two asterisks mean adding a $p$-GTF to hydrogen and helium basis functions in addition. These sets can be denoted differently: $6-31(p,d)$ and $6-311(p,d)$, or $(631, 31, 1)$ and $(6311, 311, 1)$ for a second-period element, or $(31, 1)$ and $(311, 1)$ for hydrogen.

Polarization functions cannot be obtained from isolated atom calculations using the Hartree-Fock method, as they are unoccupied by electrons and thus virtual. They do not affect Hartree-Fock energy but influence the correlation energy of multi-electron atoms. However, polarization functions significantly affect the energy of molecules, allowing for the correct description of chemical bonding. Basis sets with polarization functions are the minor basis sets acceptable for accounting for electronic correlation energy and calculating the energetic effects of chemical reactions.

To describe the motion of an electron in regions far from the nucleus, which becomes essential, for example, when considering anions, excited states of atoms, and long-range intermolecular interaction forces, the behavior of valence orbitals at large distances from the nucleus must be corrected. This is achieved by introducing diffuse functions with the same symmetry as valence electron functions but with much smaller exponent values. As a result, at large distances, the diffuse function has a greater value than the valence function and more accurately describes the electron's behavior. Adding diffuse functions affects the calculated values of electron affinity, intermolecular interaction energy, and other characteristics of molecules determined by long-range atomic interactions. The presence of diffuse functions in a basis set is indicated by the symbol "+". For example, the $6-31++G$ basis set includes diffuse functions for second-period elements and hydrogen. The $6-31++G*$ basis set, also denoted as $6-31++G(d,p)$, simultaneously includes both diffuse and polarization functions for all atoms of the chemical elements of both periods. This last basis set for a second-period element can be denoted as $(6311, 3dp)$.

## 6.6 CORRELATION-CONSISTENT BASIS SETS

Correlation-consistent basis sets are attractive for highly accurate calculations and calculations of weakly bound states. By composition, the sets are extended, including the description of each orbital with two (DZ), three (TZ), four (QZ), five (5Z), and six (6Z) independent functions. In addition, they contain several polarization and diffuse functions.

Calculating electron affinity in atomic and molecular systems is challenging in quantum chemistry. The Hartree-Fock method with limited configuration interaction is insufficient due to the higher correlation energy of anions compared to atoms. To accurately determine electron affinity, extensive electron correlation calculations and more configurations are needed. Often, the basis set for anions is derived from one optimized for the neutral atom state [168]. Suitable for this purpose are correlation-consistent (cc - correlation-consistent) valence basis sets with polarization functions (p - polarization) on all atoms: double-zeta (cc-pVDZ), triple-zeta (cc-pVTZ), and quadruple-zeta (cc-pVQZ). Then, with additional diffuse functions optimized for atomic anions, the primary basis is slightly increased (aug - augmented). Optimization is performed using the Hartree-Fock method with single and double excitation configuration interaction of the anion. Such basis sets are called augmented correlation-consistent polarized valence multi-zeta basis sets and are denoted as aug-cc-pVDZ, aug-cc-pVTZ, and aug-cc-pVQZ. The basis sets for second-period elements are relatively large, consisting of 9, 14, and 20 shells, respectively.

In this work, the Gaussian computational chemistry program was used for the time-dependent density functional theory (TDDFT) simulations. TDDFT provides insights into the HOMO–LUMO orbitals involved in the absorption and emission energies. In our analysis of organic compounds, we utilize the B3LYP and CAM-B3LYP functional; $6-311$+G(d,p) and $6-31$+G(d,p) basis set for accurate simulations. We used the polarizable continuum model (PCM) to model solvation effects. The PCM is widely used in computational chemistry to efficiently model solvation effects by treating the solvent as a polarizable continuum. The following chapters will detail the results of the simulations and experiments for spectroscopic analysis.

# SPECTROSCOPIC PROPERTIES OF PY-RES

T HE STUDY of photochemical and spectroscopic properties of conjugated organic molecules is a long-standing issue, being widely exploited in the design of chemical sensors and electro-optical devices [169, 170]. More specifically, the demand for specific probes for environmental contaminants and other organic targets makes the synthesis of highly conjugated organic materials a timely topic, with a particular emphasis on the functionalization of $\pi$-conjugated monomers with fluorescent moieties [171–173]. In most cases, the primary strategy consists of promoting the secondary attachment of a chromophore into the polymeric backbone [174–177], thus avoiding the overlapping between the frontier orbitals of the monomer and chromophore. Such a synthetic procedure tends to preserve the spectroscopic properties of the chromophore, including its sensitivity to environmental conditions like solvent polarity [176, 177], pH [178], temperature [179], and medium composition [170]. In this context, the use of pyrrole derivatives has attracted remarkable attention, as the electropolymerization of pyrrole has become a robust method to obtain stable conducting polymeric films with similar spectroscopic properties of the monomers [174, 176, 180]. Consequently, fluorescent and electrochemical properties of pyrrole derivatives have been successfully used in different applications, including the biosensing of DNA hybridization [174, 181], the potential conductive conduits for nerve regeneration [182, 183], and the active probe in biomaging [184, 185].

Recently, several studies have exploited the fluorescent properties of resorufin derivatives to develop chemical and biological sensors [186–190]. A prominent example is the use of resorufin derivatives as chemical sensors for aliphatic thiol compounds found in biological systems [191–193], as the deficit or abundance of such compounds may be associated with several diseases [193]. Combining the resorufin and 7-diethylcoumarin to obtain a single-molecule fluorescence probe, Zhang and co-workers have successfully distinguished different reactive sulfur species in living cells [191]. Similarly, the affinity of a resorufin derivative to the fibrillar amyloid $\beta$ has been used to identify cerebrovascular amyloid deposits over neuritic plates, thus opening the

possibility of a precise and non-invasive diagnostic of cerebral amyloid angiopathy in live patients [194]. As the resorufin fluorescence is strongly affected by redox reactions, compounds based on this chromophore have been used in the detection of metallic ions [187] and the identification of corrosion processes [190]. Besides, resorufin emission is sensitive to environmental conditions, such as surfactant concentration [195], temperature [196], and medium polarity [197, 198].

The study presents the synthesis and spectral analysis of a new pyrrole derivative with a resorufin label. 3-(N-pyrrolyl)propyl resorufin (PY-RES) was synthesized using resorufin as a starting material [199]. The fluorescence properties of PY-RES are examined in solvents with different polarities, revealing a strong influence of the medium polarity on its fluorescence spectrum, characterized by excitation-dependent emission. The study also investigates the thermal effects on PY-RES emission and confirmed the occurrence of typical thermal-quenching. Additionally, a detailed computational analysis of PY-RES using time-dependent density functional theory (TDDFT) providesinsights into the HOMO-LUMO orbitals involved in the absorption and emission energies. Moreover, the possibility of using PY-RES photoluminescence to develop a ratiometric sensor for detecting ethanol adulteration with methanol is also analyzed.

## 7.1 MATERIALS AND METHODS

### 7.1.1 MATERIALS AND SYNTHESIS

All the chemical reagents and solvents were purchased from Sigma-Aldrich/Merck. The solvents used in the synthesis were previously treated and distilled. The $^1$H and $^{13}$C NMR spectra were recorded in a Bruker spectrometer operating at frequencies of 400 MHz and 100 MHz, respectively, using $CDCl_3$ as solvent. Infrared (IR) spectra were acquired on a Shimadzu IR PRESTIGE–21 device, using attenuated total reflection Fourier transformed infrared spectroscopy (ATR-FTIR) technique. High resolution mass spectra (HRMS) were acquired using a Q-Exactive mass spectrometer (ThermoScientific), with H-ESI source (ThermoScientific), operating in positive mode under the following conditions: full scan m/z 230-450, spray voltage 4.0 - 5.0 kV, flow 20 $\mu$L/min, sheath gas 12, auxiliary gas 0 to 2, capillary temperature 300 °C, auxiliary gas temperature 37 °C, slens 50.

## 7.1.2 SYNTHESIS OF 3-(N-PYRROLYL)PROPYL RESORUFIN (PY-RES)

1-(3-bromopropyl)pyrrole (3) and 1-(3-iodopropyl)pyrrole (4) were prepared according to procedures reported in the literature [199]. In a 50 mL round-bottom flask, 234.98 mg (1 mmol) of 1-(3-iodopropyl)pyrrole (4), 235.15 mg (1 mmol) of resorufin sodium salt (5), and 15 mL of dimethylformamide (DMF) were added. The system was kept in an argon atmosphere and at room temperature for about 24 hours. At the end, 30 mL of ethyl acetate was added, and the system was washed with distilled water (10 x 20 mL) and 10% sodium bicarbonate solution (NaHCO$_3$) (3 x 20 mL). The organic phase was dried with anhydrous Na$_2$SO$_4$ and concentrated on a rotary evaporator. A red solid in 50% yield was obtained after purification on a silica gel column chromatography using hexane/acetate (1:1) as eluent. Scheme 1. M.p. 159.5-160.2 °C; HRMS (ESI (+)): calculated for C$_{19}$H$_{16}$N$_2$O$_3$H [M + H] m/z: 321.12; found m/z: 321.122. $^1$H NMR (400 MHz, CDCl$_3$), $\delta$ (ppm): 7.70 (d, J = 8.8 Hz, 1H); 7.42 (d, J = 9.7 Hz, 1H); 6.92 (dd, J = 8.9 and J = 2.6 Hz, 1H); 6.83 (dd, J = 9.8 and 1.9 Hz, 1H); 6.76 (d, J = 2.5, 1H); 6.64 (t, J = 1.9 Hz, 2H); 6.32 (d, J = 1.9 Hz, 1H), 6.15 (t, J = 1.9 Hz, 2H), 4.13 (t, , J = 6.6 Hz, 2H); 3.96 (t, J = 5.8 Hz, 2H) ; 2.27 (t, , J = 6.2 Hz, 2H). $^{13}$C NMR (100 MHz), $\delta$ (ppm): 186.4; 162.7; 149.8; 145.7; 145.6; 134.7; 134.2; 131.7; 128.5; 126.0; 120.6; 113.9; 108.5; 106.7; 100.6; 65.3; 45.6; 30.9. FT-IR (ATR) (cm$^{-1}$): 3057 ($\nu$ C-H, aromatic); 2929 and 2875 ($\nu$ C-H, aliphatic); 1693 ($\nu$ C=O, carbonyl ketone); 1604, 1504 and 1446 ($\nu$ C=C, aromatic); 1261 and 1099 ($\nu$ O-C-O, ether); 1211 ($\nu$ C-N, pyrrole); 1232 ($\nu$ C-N, dimetylamine); 858 ($\delta$ C-H aromatic); 725 ($\delta$ C-H pyrrole).

## 7.1.3 UV-VIS SPECTROSCOPY

All UV-Vis absorption spectra were acquired using a USB2000 spectrometer (Ocean Optics) with a DH2000 light source (Ocean Optics). The PY-RES was dissolved in the concentration of 0.1 mM for all solvents. The emission spectra were recorded on a spectrofluorimeter NanoLog TM (HORIBA), with a Xenon lamp (CW 450 W) as the excitation source and a photomultiplier detector (model R928P), chosen for its high sensitivity and fast response time, using the diffraction grating Horiba with 600 grooves/mm and blaze at 1000 nm.

### 7.1.4 THEORETICAL CALCULATION DETAILS

Theoretical calculations of electronic properties of PY-RES focused on the Frontier molecular orbitals (Highest Occupied Molecular Orbital - HOMO and the Lowest Unoccupied Molecular Orbital - LUMO) and the vertical absorption and emission energies in a solvent environment. The quantum calculations were performed using Density Functional Theory (DFT) for the equilibrium properties in the ground state and Time-Dependent Density Functional Theory (TD-DFT) for the absorption and emission energies, both utilizing the -(N-pyrrolyl)propyl resorufin (PY-RES) functional [200–202], which includes long-range and dispersion corrections, and the 6-311+G(d,p) basis set. Polar and apolar solvents were considered, being modeled using the integral equation formalism version of the polarizable continuum model (IEF-PCM)[203]. The PCM demonstrates high accuracy in modeling the solvent effects on the absorption and emission energies of solvated molecules when considering aprotic solvents [177, 204, 205], as shown in this study. The absorption and emission energies were calculated using the State-Specific approach [202], and all QM calculations were performed with the Gaussian 09 software package [206].

## 7.2 RESULTS AND DISCUSSION

**Figure 22** – *Schematic representation of the synthetic route used to prepare the 3-(N-pyrrolyl)propyl resorufin (PYRES) compound.*
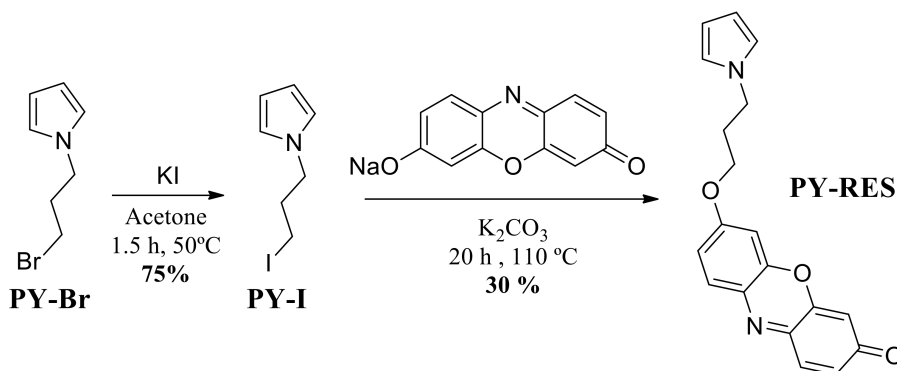
**Figure 23** – *Absorption spectra of PY-RES in solvents with distinct polarities: heptane (solid black line) and acetonitrile (dashed red line). Vertical dotted lines correspond to the theoretical predictions for the absorption wavelengths using the TD-DFT method. One can note that a blue shift takes place in the high energy bands when PY-RES is dispersed in polar solvent, while a red shift is observed in low energy bands.*
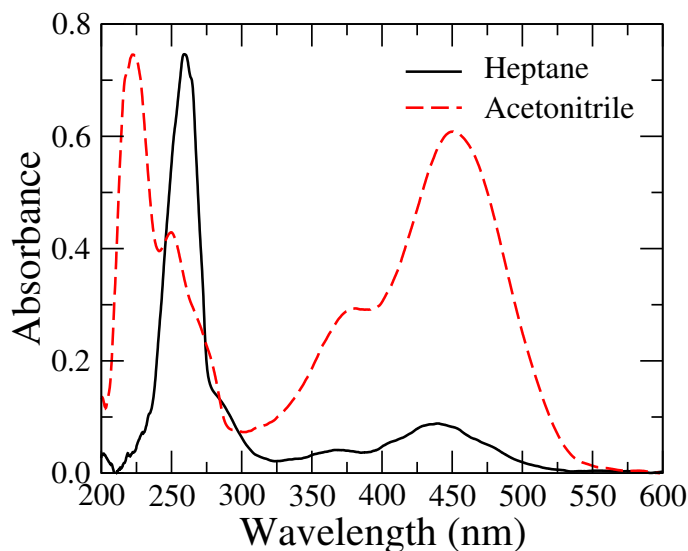


### 7.2.1 SYNTHESIS

The synthetic route to obtain PY-RES was divided into three steps. The first step involves a Clauson-Kaas condensation, while the second is a halide exchange. The third step was the esterification, as shown in Fig. 22. 1-(3-bromopropyl)pyrrole was prepared by condensation of the 3-bromopropylamine hydrobromide with 2,5-dimethoxytetrahydrofuran, in glacial acetic acid/sodium acetate buffer solution (pH = 5.0). 1-(3-iodopropyl)pyrrole was prepared by the halide exchange reaction between 3 and NaI, being necessary due to the nucleophilic substitution reaction between 1-(3-bromopropyl)pyrrole and resorufin sodium salt gave low yields. Better results were obtained by replacing bromine with iodine through a halide exchange reaction [199]. The nucleophilic substitution in the synthetic procedure increases the PY-RES yield. The molecular structure of the PY-RES was confirmed by $^1$H and $^{13}$C NMR (Supplementary Material, Figs. S1 and S2), HRMS (Supplementary Material, Fig. S3) and FTIR (Supplementary Material, Fig. S4) analyses.

Fig. 23 displays the absorption spectra of PY-RES in aprotic solvents with varying polarities. In heptane, PY-RES exhibits multiple absorption bands across different regions of the electromagnetic spectrum. Specifically, such compound presents a strong absorption band centered at

**Figure 24** *– Frontier molecular orbitals (MOs) of PY-RES in (a) heptane and (b) acetronitrile, corresponding to HOMO-3, HOMO-1, HOMO, and LUMO levels. The red arrows represent the molecular orbitals involved in the vertical electronic transitions, with the solid red arrow representing the major contributing orbital.*
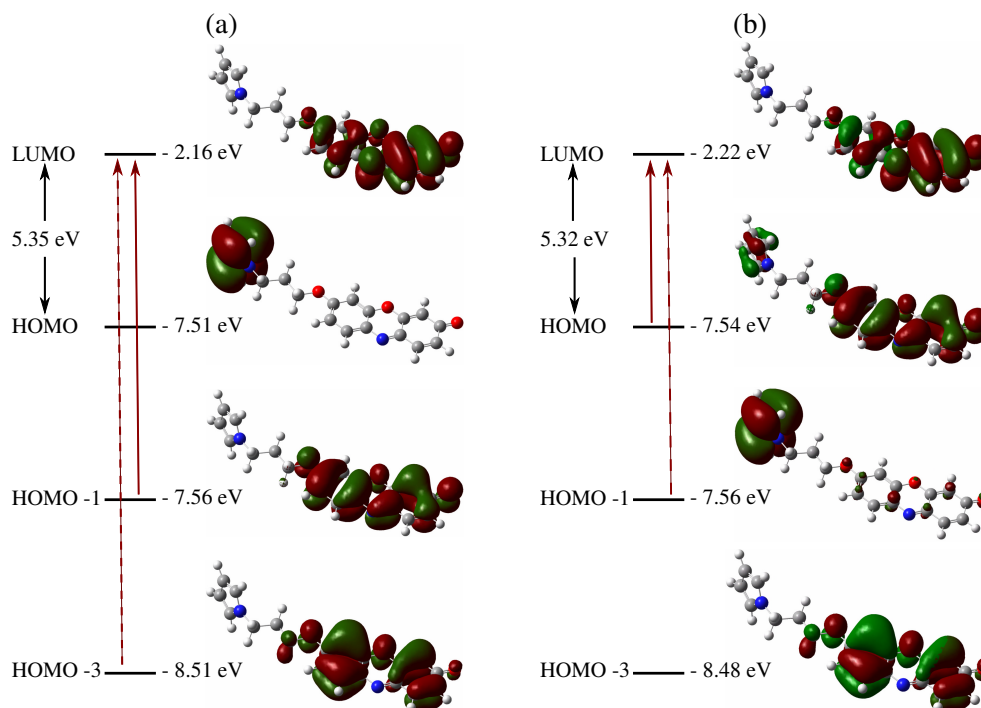
260 nm, corresponding to the high-energy $\pi \rightarrow \pi*$ transitions of pyrrole group [207]. Besides, three weak bands are centered at 285, 367, and 442 nm, being assigned as $\pi \rightarrow \pi*$ and $n \rightarrow \pi^*$ transitions of resorufin moiety [198]. In particular, the absorption peak at $\lambda_g = 442$ nm is associated with the low energy $\pi \rightarrow \pi^*$ transitions from the ground state, $S_0$, to a locally excited state, $L_a$, without a significant charge transfer. A notable change in the absorption spectrum occurs when PY-RES is dispersed in a polar solvent. A significant blue shift is observed in the absorption band assigned to the pyrrole group, now positioned at 220 nm in acetonitrile. A similar blue shift occurs for the band at 285 nm, indicating an enhancement in the energy gap between the electronic states involved in the $\pi \rightarrow \pi*$ transitions. A distinct scenario is verified for the low-energy transitions associated with resorufin moiety, where the absorption bands at 379 and 452 nm characterize a moderate red shift. In addition to the red shift, such bands become more pronounced in the polar solvent, thus indicating an increase in the transition probabilities. The red shift and absorbance enhancement of the low energy absorption band suggests that a moderate intramolecular charge transfer may occur in PY-RES upon photoexcitation, favored in polar solvents.

Fig. 24 presents the frontier orbitals involved in PY-RES electronic transitions. The HOMO and LUMO levels were computed by density functional theory at the CAM-B3LYP/6-311+G(d,p) level, considering PY-RES dispersed in heptane and acetonitrile. For PY-RES dispersed in heptane, TD-DFT simulations reveal that the vertical electronic transition is not a typical HOMO-LUMO transition, involving HOMO-1 and HOMO-3 levels. The theoretical calculations estimate an absorption peak at 393 nm, with an oscillator strength of 0.78, with the formation of a locally excited state. Although such a TD-DFT result is shifted compared to the experimental one ($\lambda_g = 442$ nm), it captures the main features of electronic transitions in PY-RES dispersed in an apolar solvent. For PY-RES dispersed in acetonitrile, TD-DFT calculations show that vertical electronic transition is a typical HOMO-LUMO transition, also involving the HOMO-1 level. Furthermore, the absorption peak is estimated at 431 nm, with an oscillator strength of 1.10. The simulations show that the polar solvent favors an electronic transition through a charge transfer mechanism. Again, the TD-DFT calculations reproduce the primary behavior of PY-RES dispersed in a polar solvent.

Fig. 25 shows the emission spectra of PY-RES dispersed in apolar and polar solvents, considering photoexcitation at different wavelengths. In all cases, the fluorescence intensities were normalized by the emission peak at $\lambda_{em} = 498$ nm. When dispersed in toluene, PY-RES presents a broad emission spectrum upon photoexcitation at $\lambda_{exc} = 405$ nm, with two identifiable peaks at $\lambda_{em} = 498$ nm and $\lambda_{em} = 515$ nm, as depicted in Fig. 25(a). As the photoexcitation energy is reduced, the emission intensity of PY-RES gradually decreases, with no significant changes in the spectral density. A distinct scenario is verified when PY-RES is dispersed in the polar solvent, as demonstrated in Fig. 25(b). For $\lambda_{exc} = 405$ nm, the PY-RES fluorescence in acetonitrile is characterized by peaks at $\lambda_{em} = 498$ nm and $\lambda_{em} = 515$ nm, exhibiting a similar spectral distribution to that in toluene. However, when the excitation wavelength increases, a substantial modification occurs in the PY-RES fluorescence, displaying new emission bands centered at $\lambda_{em} = 550$ nm and $\lambda_{em} = 600$ nm. Additionally, the enhancement in the excitation wavelength leads to a suppression of the original emission bands. Such results indicate that PY-RES photoluminescence is associated with distinct excited states exhibiting different charge distributions.

The impact of solvent polarity on PY-RES photoluminescence is shown in Fig. 26(a), considering a photoexcitation at $\lambda_{exc} = 450$ nm. A substantial modification in the PY-RES fluorescence

**Figure 25** – *Emission spectra of PY-RES in (a) toluene and (b) acetonitrile, considering different photoexcitations: $\lambda_{exc} = 405$ nm (solid black lines), $\lambda_{exc} = 450$ nm (dashed red lines), and $\lambda_{exc} = 488$ nm (dashed-dotted blue lines). Notice the spectral distribution of PY-RES emission is strongly affected by the solvent polarity, indicating the occurrence of different excited states upon photoexcitation.*
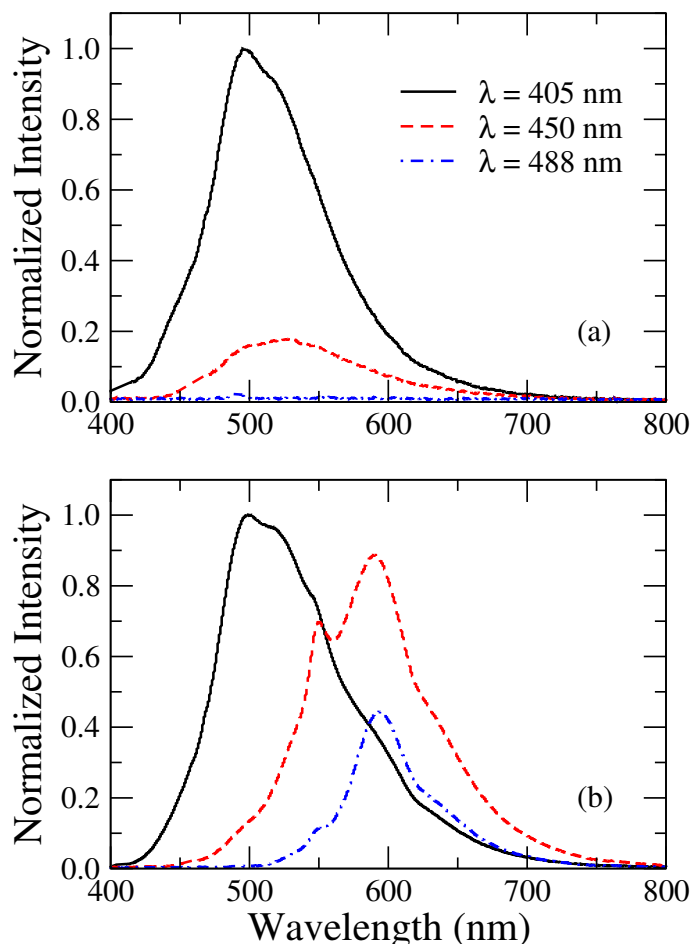


is observed as the solvent polarity increases, characterized by a significant red shift ($\Delta\lambda_{emi} \sim 100$ nm) and a notable change in the spectral distribution. Such results suggest that different electronic states are involved in the photoluminescence mechanism of PY-RES, depending on the solvent polarity. In nonpolar hydrocarbon solvents, such a compound displays a broad emission with strongly overlapped bands. In contrast, the PY-RES fluorescence spectra show two distinct narrow peaks in polar solvents. Despite a gradual red shift in the lower energy emission band, the higher energy band remains centered at 549 nm as the solvent polarity increases. Additionally, the relative emission intensity between the two bands changes, with the lower energy band becoming the predominant one in highly polar solvents. When dispersed in acetonitrile, PY-RES exhibits a similar fluorescence to resorufin in protic polar solvents [208–210] but features a more significant Stokes shift compared to the sodium salt of resorufin. A study by Yu and Berg has

**Figure 26** – *(a) Normalized spectra of PY-RES fluorescence in different solvents: heptane (solid black line), toluene (dashed red line), ethyl acetate (dotted blue line), acetone (dashed-dotted green line), and acetonitrile (solid orange line). The samples were photoexcited at 450 nm. Notice that the spectral distribution of PY-RES is strongly affected by the solvent polarity, indicating that PY-RES photoluminescence involves excited states with distinct charge distributions. (b)PY-RES Stokes shift as a function of the solvent polarity parameter $E_T^N$. The dashed red line represents the linear fit of Stokes shift, with a regression slope $m = 5662~cm^{-1}$ and correlation coefficient $R = 0.92$.*
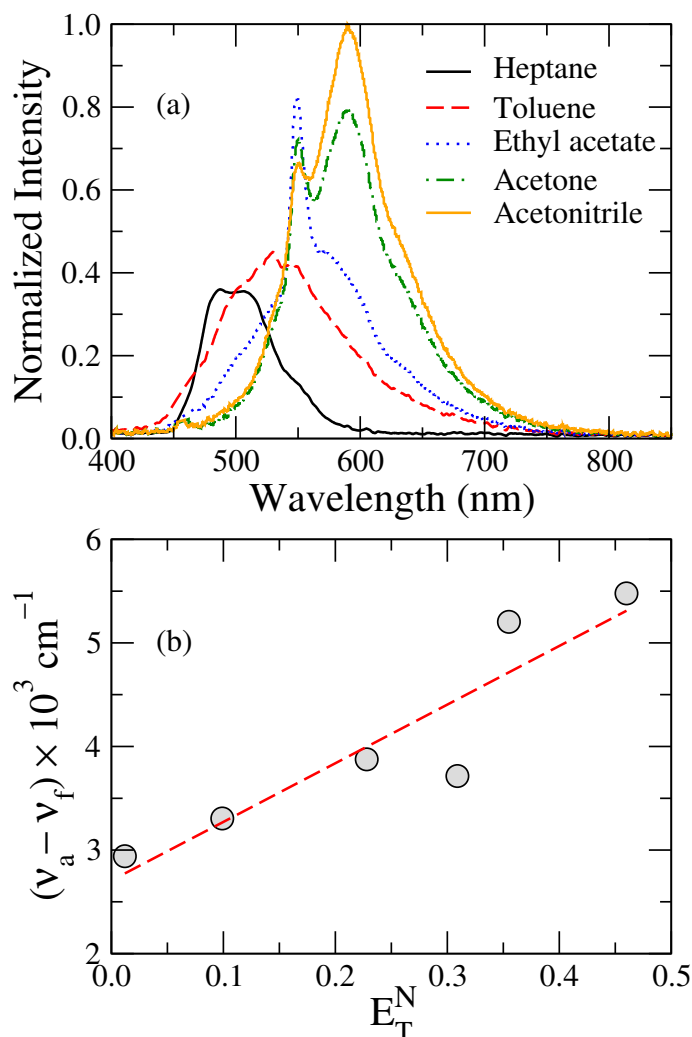


shown that the sodium salt of resorufin may have a Stokes shift of up to $467~cm^{-1}$, which is significantly below the $5252~cm^{-1}$ observed for PY-RES in acetonitrile [208]. The experimental and theoretical results for the absorption and fluorescence parameters of PY-RES in different solvents are summarized in Table 1.

Considering the Stokes shift of PY-RES dispersed in different solvents, it is straightforward to estimate the variation of molecular dipole moment upon photoexcitation [211]. Using the empirical polarity parameter $E_T^N$ introduced by Reichardt [1, 212], the relation between the

**Table 2** – *Solvents parameters and solvatochromic data of PY-RES: $\epsilon$ represents the solvent dielectric constant, and $E_T^N$ is the Reichardt solvent parameter [1]. $\lambda_g$ ($\nu_g$) and $\lambda_f$ ($\nu_f$) are the absorption and fluorescence peak wavelengths (wavenumbers), respectively. The emission peaks were acquired upon photoexcitation at 450 nm. The Stokes shift is defined as ($\nu_g - \nu_f$). $\lambda_g^{Th}$ and $\lambda_f^{Th}$ are the absorption and fluorescence peak wavelengths obtained from TD-DFT calculations, while ($\nu_g - \nu_f$)$^{Th}$ is the theoretical Stokes shift.*

| Solvent | $\epsilon$ | $E_T^N$ | $\lambda_g$ (nm) | $\lambda_g^{Th}$ (nm) | $\lambda_f$ (nm) | $\lambda_f^{Th}$ (nm) | ($\nu_g - \nu_f$) (cm$^{-1}$) | ($\nu_g - \nu_f$)$^{Th}$ (cm$^{-1}$) |
|---|---|---|---|---|---|---|---|---|
| Heptane | 1.92 | 0.012 | 442 | 384 | 508 | 474 | 2940 | 4945 |
| Toluene | 2.36 | 0.099 | 451 | 398 | 530 | 474 | 3305 | 4029 |
| Ethyl acetate | 6.02 | 0.228 | 452 | 399 | 548 | 476 | 3876 | 4055 |
| Dichloromethane | 8.93 | 0.309 | 456 | 402 | 549 | 475 | 3715 | 3823 |
| Acetone | 21.01 | 0.355 | 452 | 401 | 588 | 475 | 5117 | 3884 |
| Acetonitrile | 36.64 | 0.460 | 451 | 432 | 591 | 475 | 5252 | 2095 |

Stokes shift and the change of molecular dipole moment is given by:

$$\nu_g - \nu_f = 11307.6 \left[ \left( \frac{\delta\mu}{\delta\mu_B} \right)^2 \left( \frac{a_B}{a} \right)^3 \right] E_T^N + constant \quad . \tag{7.1}$$

$\nu_g$ and $\nu_f$ represent the absorption and fluorescence maximum wavenumbers in cm$^{-1}$. $\delta\mu_B = 9$ D represents the dipole moment change of betaine dye upon excitation, while $a_B = 6.2$ Å is the Onsager cavity radius of this dye [1]. $\delta\mu$ and $a$ stand for the variation of the dipole moment and the Onsager cavity radius of the PY-RES molecule, respectively. Fig. 26(b) shows the dependence of the PY-RES Stokes shift on the polarity parameter $E_T^N$, where a linear regression (dashed red line) can be used to estimate the variation in the dipole moment of PY-RES molecules upon photoexcitation, as follows:

$$\delta\mu = \sqrt{ \frac{\delta\mu_B^2 \times m \times a^3}{11307.6 cm^{-1} \times a_B^3} } \quad . \tag{7.2}$$

As the molar mass ($M_m = 320.34$ g/mol) and the density ($\rho_P = 1.10$ g/cm$^3$) can be used to compute $a = 4.87$ Å, it leads to an estimate of $\delta\mu = 4.57$ D for PY-RES molecule upon photoexcitation at 450 nm. This value agrees with the theoretical estimate for sodium salt of resorufin [210].

Fig. 27 shows the temperature dependence of PY-RES fluorescence under photoexcitation at 405 nm, considering dichloromethane and acetonitrile as carrier solvents. The thermal effects on PY-RES fluorescence were investigated using a temperature-controlled oven within the accuracy of $0.1°$C. The samples were heated in a small temperature range between 25 °C and 40 °C to avoid solvent evaporation and the subsequent enhancement of PY-RES concentration. The temperature of each PY-RES solution was varied in steps $5.0°$C, at a rate of $0.5°$C/min. The PY-RES fluorescence is gradually quenched in both solvents as the temperature is enhanced

**Figure 27** – *Temperature dependence of PY-RES fluorescence in (a) dichloromethane and (b) acetonitrile: $T = 25°C$ (solid black lines), $T = 30°C$ (dashed red lines), $T = 35°C$ (dotted blue lines), and $T = 40°C$ (dashed-dotted green lines). Notice that emission intensity gradually decreases as the temperature is increased. The insets show the linear relation between peak intensity, $I_p(T)$, and the sample temperature, $T$. Dashed red lines represent the linear regressions using the expressions $I_p(T) = I_0 + \Gamma \cdot T$, with $\Gamma = -0.030 \pm 0.001°C^{-1}$ in dichloromethane and $\Gamma = -0.014 \pm 0.001°C^{-1}$ in acetonitrile.*
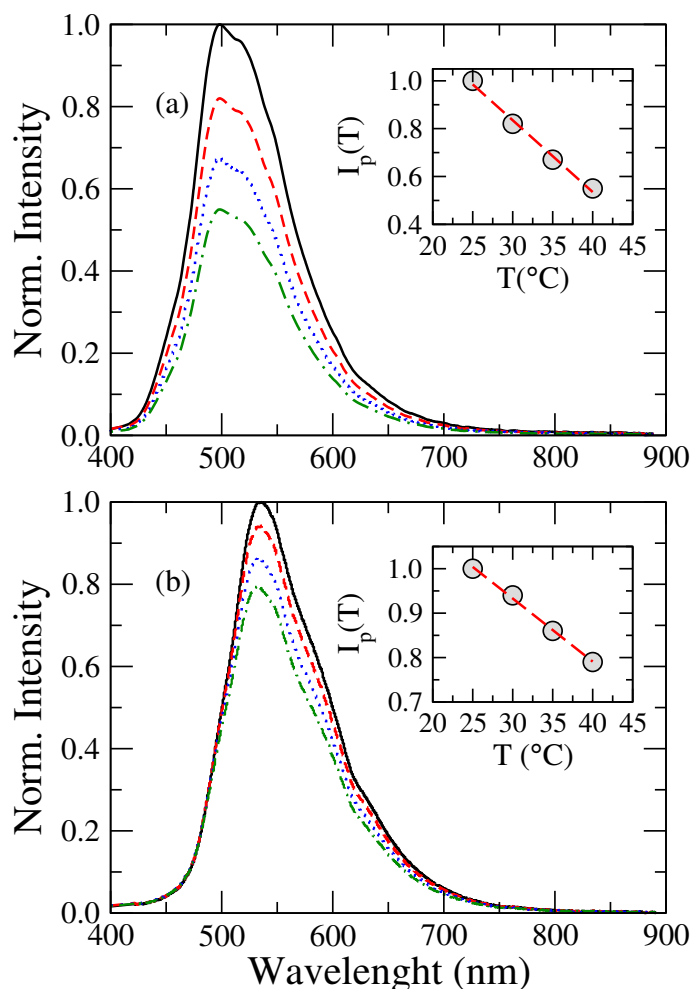


without changing the spectral distribution. However, the reduction in the emission intensity seems to be more pronounced in dichloromethane. As the electronic transitions involve a charge transfer in a polar medium, the excited state is stabilized in a polar solvent, and the non-radiative process becomes less pronounced in high polar solvents. The absence of thermochromic effects indicates that the energy gap between excited and fundamental states is not affected by the sample temperature in the small range investigated. Additionally, the peak intensity exhibits a linear dependence on the sample temperature, obeying the relation $I_p(T) = I_0 + \Gamma \cdot T$. Here, $\Gamma$ is the thermal reduction rate of the emission intensity, with $\Gamma = -0.030 \pm 0.001°C^{-1}$ in dichloromethane and $\Gamma = -0.014 \pm 0.001°C^{-1}$ in acetonitrile.

**Figure 28** – *(a) Fluorescence spectra of PY-RES dispersed in ethanol-methanol solutions, for different volumetric fraction of methanol: $\varphi_v = 0\%$ (solid black line), $\varphi_v = 5\%$ (dashed red line), $\varphi_v = 10\%$ (dotted blue line), and $\varphi_v = 20$ (dashed-dotted greenk line). The addition of small volume of methanol leads to a pronounced change in the spectral distribution of PY-RES emission. (b) $I_{552}/I_{607}$ ratio of PY-RES emission as function of methanol volumetric fraction. Photographs of PY-RES under 450 nm laser excitation, for $\varphi_v = 0\%$ (green emission) and $\varphi_v = 80$ (magenta emission).*
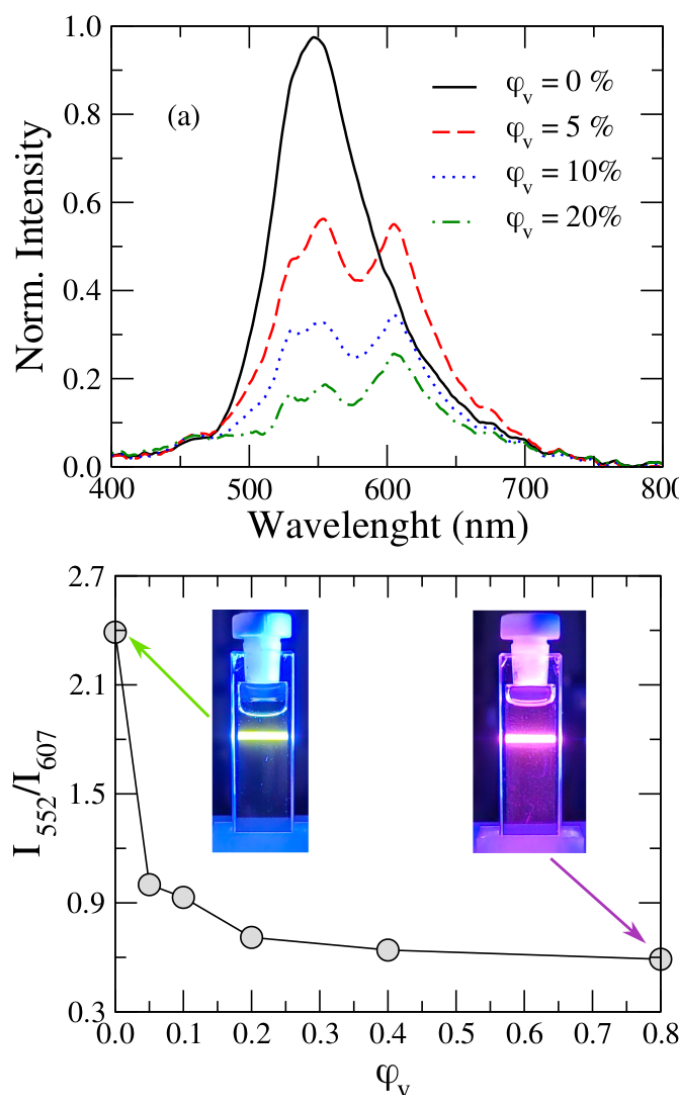


As the PY-RES emission strongly depends on the solvent polarity, such a compound may be a suitable physicochemical probe for detecting solvent adulteration. In particular, alcohol adulteration with methanol is a constant concern in many developing countries, as methanol represents a health risk to either humans or animal species [213]. Such compound promotes irreversible tissue damage when inhaled, ingested, or absorbed by the skin [213]. Envisaging the application of PY-RES as a fluorimetric sensor of ethanol adulteration, Fig. 28(a) displays the fluorescence spectra of PY-RES dispersed in ethanol, considering different volume fractions

of methanol, $\varphi_v$. All samples were photoexcited at 450 nm. When dispersed in pristine ethanol ($\varphi_v = 0\%$, PY-RES exhibits a broad emission band centered at 547 nm. As a small volume of methanol is added to the PY-RES solution $\varphi_v = 5\%$, a pronounced modification in the emission spectrum is noticed, which presents two well-defined emission bands centered at 552 nm and 607 nm. The intensity relation between these two bands is gradually modified as the methanol concentration is enhanced in the PY-RES solution. Such a result opens the possibility of using the PY-RES emission spectrum as a ratiometric sensor of alcohol adulteration with methanol. Fig. 28(b) shows the intensity ratio $I_{552}/I_{607}$ of PY-RES emission as a function of methanol fraction. Here, $I_{552}$ and $I_{607}$ are the emission intensities of PY-RES at 552 nm and 607 nm, respectively. $I_{552}/I_{607}$ decreases monotonically as the methanol fraction is enhanced, with the PY-RES fluorescence changing from green to magenta.

# SPECTROSCOPIC PROPERTIES OF MONOCARBONYL CURCUMIN

CURCUMIN'S ((1E,6E)-1,7-bis(4-hydroxy-3-methoxyphenyl)-1,6-heptadiene-3,5-dione) chemical structure comprises three main components: two aromatic rings, each bearing hydroxy and methoxy groups, connected by a seven-carbon chain that includes a $\beta$-diketone moiety [214, 215]. Curcumin and the related curcuminoid family, which constitute the yellow pigments in the spice turmeric, has been reported to be anticarcinogenic, anti-inflammatory and antioxidant [216–220].

Extensive steady-state fluorescence spectroscopic studies of curcumin have been conducted in various organic solvents, micro-heterogeneous systems, and bio-mimetic environments [214, 221, 222]. These investigations have revealed that curcumin's fluorescence spectrum, maximum emission wavelength, and fluorescence quantum yield are highly sensitive to the solvent's properties. Depending on the solvent used, the Stokes shift has shown significant variation, ranging from 2000 to 6000 cm$^{-1}$.

Efforts have been made to modify and enhance curcumin's pharmacological and pharmacokinetic properties. Recent studies are focused on the application of Monocarbonyl curcumin, in which the two carbonyl groups of curcumin are reduced to one, for the treatment of cancer [223–225]. The photophysical properties of curcumin analogs are widely exploited using absorption and fluorescence studies in various solvents [226, 227] since the changes in absorption and fluorescence properties with different solvents have provided valuable insights into curcumin's interactions with proteins like liposomes and human albumin [228]. In this way, new dyes with long stoke shifts have been studied, such as human serum albumin (HSA) labeled with a BODIPY dye. Traditional BODIPY dyes have minor to moderate Stokes shifts (15-70 nm), which limits their effectiveness in some applications. However, the BODIPY with significant Stokes shifts (80– 114 nm) has been studied.

In this study, we have shown how various solvents influence the electronic absorption and flu-

orescence spectra of Monocarbonyl curcumin, *(1E,4E)-1,5-bis(4-(dimethylamino)phenyl)penta-1,4-dien-3-ona*, labeled as CCM. Computational analysis of monocarbonyl curcumin analogs was performed to supplement the experimentally determined values. We perform a detailed computational analysis of aminocarbonyl curcumin using time-dependent density functional theory (TDDFT), thus supplying information about the HOMO-LUMO orbitals and the solvent effects on the vertical absorption and emission energies. Our results show that the fluorescence spectrum of mocarbonyl curcumin is strongly affected by the polarity of the solvent. Figure 29 shows the molecular structure of the Monocarbonyl curcumin.

**Figure 29** – *Ball-and-stick model of the molecular structure of CCM, with carbon, oxygen, and nitrogen atoms colored gray, red, and blue, respectively. The structure is optimized using the B3LYP functional.*
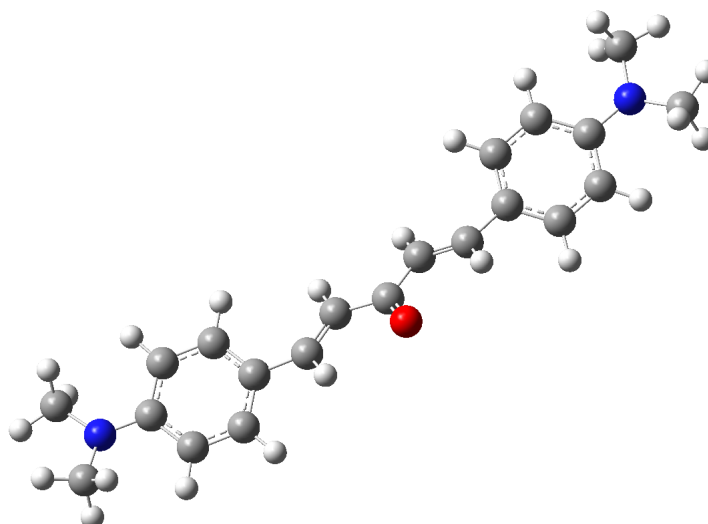


## 8.1 SYNTHESIS

A methodology inspired by ALSANTALI [229] synthesized the CCM product. The process involved adding 96.0 mg (2.4 mmol) of NaOH and 2 mL of ethanol to a 25 mL flask and stirring until NaOH was completely dissolved. Subsequently, 74.08 mg (1.0 mmol) of acetone and 298.38 mg (2.0 mmol) of 4-(dimethylamino)benzaldehyde were introduced into the system, which was then stirred at room temperature for 20 hours. We added distilled water to help precipitate the yellow solid and filtered the resulting mixture through a Buchner funnel. The final compound was obtained in a 73.5% yield and displayed satisfactory purity. Figure 30 outlines the synthesis

process.

**Figure 30** – *Schematic representation of the synthetic route used to prepare the (1E,4E)-1,5-bis(4-(dimethylamine)phenyl)pentyl-1,4-dien-3-ona (CCM).*
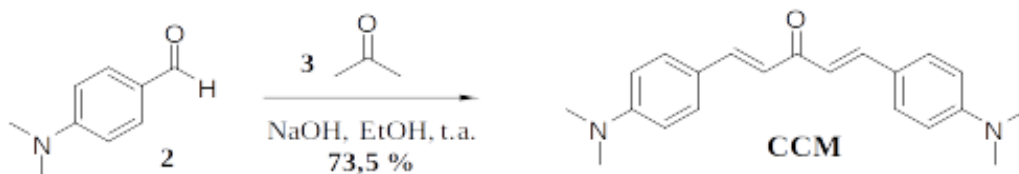


In this chapter, the focus was on the examination of the optical properties of the *(1E,4E)-1,5-bis(4-(dimethylamine)phenyl)pentyl-1,4-dien-3-ona*, labeled as CCM, synthesized by Jamilly Eli da Silva Rodrigues from the Chemistry Department of the Federal University of Alagoas. In particular, the fluorescence and light absorption phenomena in monocarbonyl curcumin were investigated, considering dispersion in apolar, polar, and protic solvents. To examine the absorption energies in CCM dissolved in methanol, TD-DFT and B3LYP were employed.

## 8.2 MONOCARBONYL EMISSION AND ABSORPTION SPECTRUM

The monocarbonyl curcumin exhibited significant fluorescence upon UV light excitation, with a strong dependence on the solvent polarity, as shown in Fig. 31. A CCM fluorescence changes from blue to red as the solvent polarity incriases, indicating a rich phenomenology associated with charge transfer in this compound.

Dielectric constant and the Reichardt normalized polarity scale, $E_T^N$, of solvents used to dilute solutions of monocarbonyl curcumin are summarized in Table 7. As the $E_T^N$ parameter includes the effect associated with the formation of hydrogen bonds and the mechanism of intramolecular charge transfer, such a parameter allows us to reasonably describe the microenvironment of molecular dipoles in solution, rather than the other bulk polarity functions based on the refractive indices and dielectric permittivities of solvents.

**Figure 31** – *Representantive images of CCM dispersed in solvents with different polarities: (a) toluene, (b) ethyl acetate, (c) acetonitrile, and (d) aniline. The images were captured for the sample under UV light.*
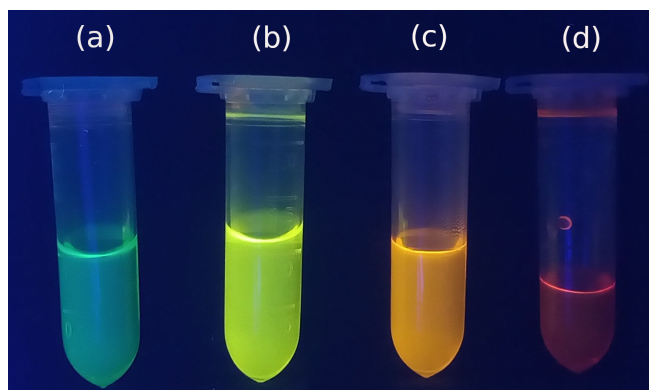


**Table 3** – *Solvent parameters: $\varepsilon$ is the solvent dielectric constant and $E_{\mathrm{T}}^{\mathrm{N}}$ is the Reichardt solvent parameter.*

| Solvent | $\varepsilon$ | $E_{\mathrm{T}}^{\mathrm{N}}$ |
|---|---|---|
| Heptane | 1.92 | 0.012 |
| Toluene | 2.4 | 0.099 |
| Ethyl acetate | 6 | 0.228 |
| Aniline | 7.06 | 0.420 |
| Acetonitrile | 36.64 | 0.460 |
| Methanol | 32.6 | 0.762 |

Absorption spectra of the monocarbonyl curcumin were recorded in various solvents varying from non-polar to polar at room temperature. Our study recorded the absorption spectrum in solvents with dielectric constants varying from 1.92 to 32.6. The compound exhibits two prominent absorption bands centered at 251 and 399nm in heptane, usually denoted as bands I and II, respectively. In most CCM compounds, band I occurs in the 430-460 nm range, while band II occurs in the 250-285nm range.

Heteroatoms tend to induce a bathochromic shift of absorption bands, which has been seen in the absorption spectrum of CCM. The absorption band II can attributed to $\pi \to \pi^*$ electronic transition, involving an electronic delocalization along the cyclic groups. Band I in the absorption spectrum corresponds to the $n \to \pi^*$ transition involving the non-bonding electrons of nitrogen atoms in the dimethylamine group. The location value of each band associated with the solvent is shown in the table 4.

Figure 32 – *UV–Vis absorption spectra of the Monocarbonyl curcumin in different solvents: heptane (solid black line), acetonitrile (dashed red line), and methanol (dasha-dotted blue line).*
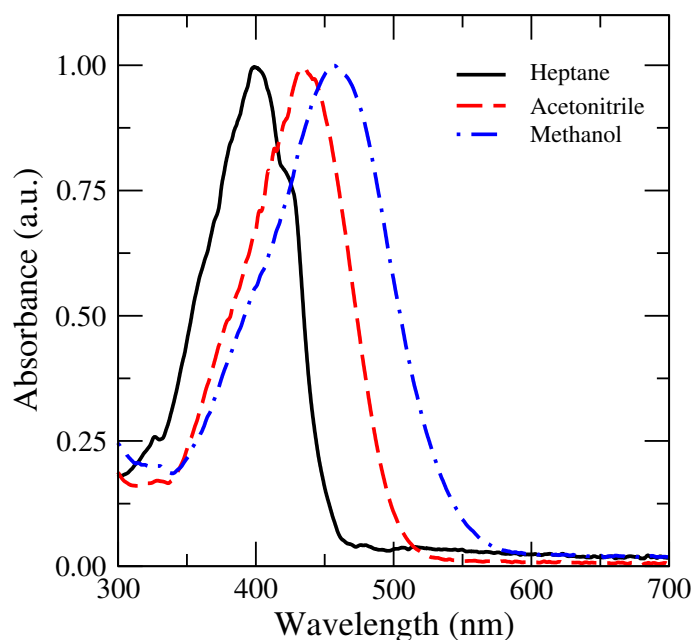


Table 4 – *Wavelength of main absorption peak $\lambda_{abs}$ for Monocarbonyl curcumin in various solvents.*

| Solvent | $\lambda_{abs}^I$ | $\lambda_{abs}^{II}$ |
|---|---|---|
| Heptane | 399 nm | 251 nm |
| Toluene | 430 nm | 281 nm |
| Ethyl acetate | 431 nm | 257 nm |
| Aniline | 453 nm | – |
| Acetonitrile | 398 nm | 259 nm |
| Methanol | 458 nm | 281nm |

We can observe the bathochromic shift in the absorption maxima, $\lambda_{abs}^I$, of monocarbonyl curcumin in various solvents. In non-polar solvents like heptane, the absorption maximum for band I is at 399 nm. As solvent polarity increases, such as in toluene (430 nm), ethyl acetate (431 nm), and aniline (453 nm), the $\lambda_{abs}^I$, the wavelength of absorption peak progressively shifts to longer wavelengths, reaching 458 nm in methanol.

Now, let us analyze the impact of solvents on CCM photoluminescence. Figure 33 displays the photoluminescence of CCM when photoexcited at 405, 450, 488, and 532nm. The CCM compound was dispersed in solvents with different polarities. CCM demonstrates a single-band emission in heptane, toluene, and ethyl acetate. In solvents with greater polarity, CCM exhibits a

**Figure 33** – *Emission spectra on excitation at 405 nm (violet line), 450 nm (blue line), 488 nm (turquoise line), and 532 nm (green line) of the Monocarbonyl curcumin in a solvent with different polarities: (a) heptane, (b) toluene, (c) ethyl acetate, (d) aniline, (e) acetonitrile, and (f) methanol.*
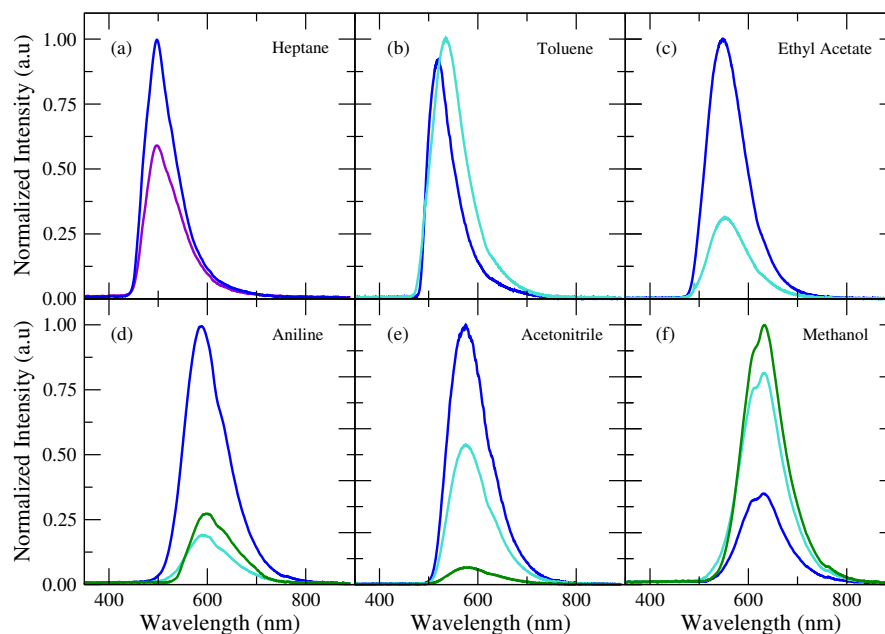


dual emission band.

The Kasha-Vavilov rule states that the emission spectrum and photochemical quantum yield are independent of excitation wavelength [230]. Figure 33 shows that the Monocarbonyl curcumin in various solvents is agreeable to the Kasha-Vavilov rule. We can observe that the shape of the curve remains constant, changing the intensity. Fig. 34 shows that CCM exhibits a broad emission in methanol and aniline. Upon evaluating the absorption peak at 453 nm, the Stokes shift is around 145 nm in aniline. The widths of the fluorescence spectra also increase considerably with the solvent polarity and hydrogen bond–donating or – accepting ability of the solvents. The molecule's steady-state absorption and fluorescence characteristics suggest that the $S_1$ state has a large intramolecular charge transfer character [231].

The presence of a dimethylamine group in the molecule is fundamental to the observed phenomenon. To better understand the phenomenon of this high Stokes shift, we performed a simulation of curcumin in methanol using the B3LYP functional and the 6-31+G(d,p) basis. Figure 35 shows the computational results.

Figure 35 (a) represents the optimization of the geometry in methanol. Figure 35 (b) gives the charge density distribution in the molecule ($e/Bohr^3$). Figure 35 (c) describes the HOMO-

**Figure 34** – *Normalized absorption (black)/emission (red) spectra of Monocarbonyl curcumin in aniline (a) and methanol (b) on excitation at 532 nm. It should be noted that Stokes shifts were calculated from both absorbance and emission maxima wavelengths.*
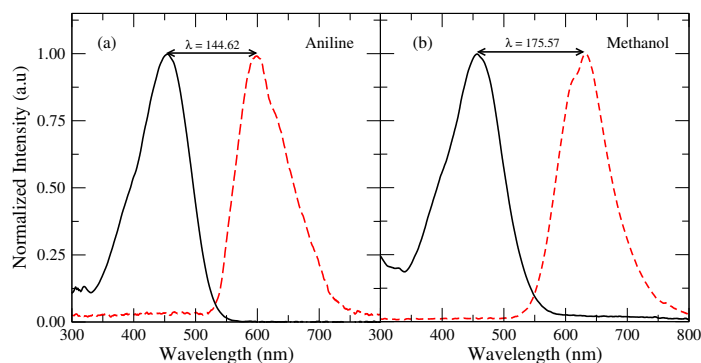


**Figure 35** – *The simulation utilized the B3LYP functional to analyze monocarbonyl curcumin in methanol as the solvent, employing PCM.*
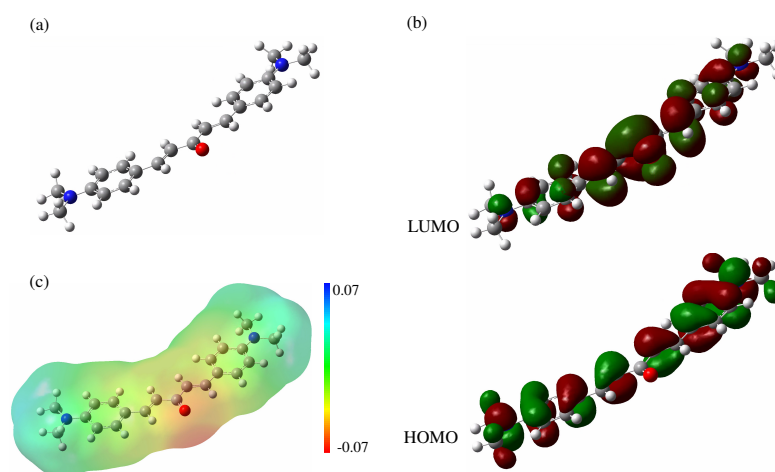


LUMO transition. the ground state to first excited state absorption is at 484nm computed via the Corrected linear-response approach. The simulation assigns the interval 280–300 nm to the band related to $\pi \rightarrow \pi^*$ . The spectrum of CCM can be assigned with the help of the calculated molecular orbitals, which are displayed in Figure 36.

A common feature of the lowest-energy transitions is that they all involve the LUMO as the unoccupied orbital. The excitations to LUMO + 1 start at relatively high energies. The LUMO can be considered the $\pi^*$ orbital of the whole molecule. From the figure 36, we can see the contribution of the dimethylamine group in the $n \rightarrow \pi^*$ transition. Figure 36 (b) shows the contribution of the carbonyl, benzene rings, and conjugated double bonds in the $\pi \rightarrow \pi^*$

**Figure 36** – *Contour plots of the MOs for CCM in methanol for assign (a) $n \rightarrow \pi^*$ and (b) $\pi \rightarrow \pi^*$ transition.*
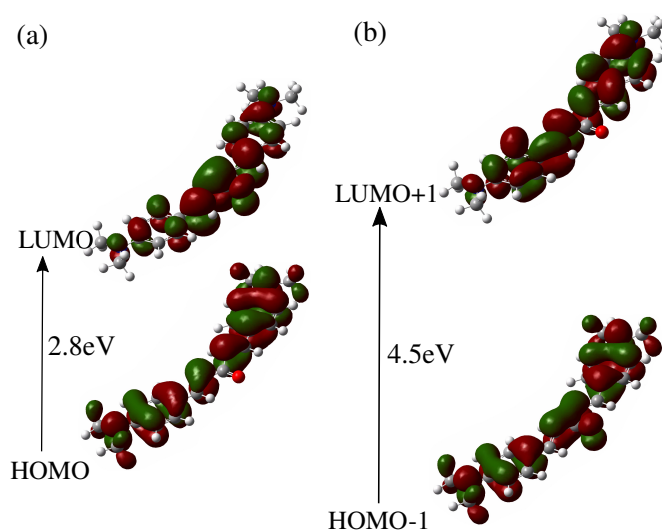


**Table 5** – *Calculated electronic transition (E, in eV) and oscillator strengths for CCM in methanol at PCM-TDDFT, using B3LYP/6-31G+(d,p).*

| Assign | $\lambda$ | $f$ | Composition | E |
|---|---|---|---|---|
| $n - \pi^*$ | 497 nm | 1.65 | HOMO–LUMO (0.99) | 2.81 |
| $\pi - \pi^*$ | 297 nm | 0.30 | HOMO-1–LUMO+1 (0.57) | 4.55 |
|  |  |  | HOMO-4–LUMO (0.22) | 4.76 |
|  |  |  | HOMO-5–LUMO (0.09) | 4.78 |
|  |  |  | HOMO–LUMO+2 (0.09) | 4.74 |
| $\pi - \pi^*$ | 284 nm | 0.15 | HOMO-5–LUMO (0.56) | 4.78 |
|  |  |  | HOMO-1–LUMO+3 (0.03) | 5.08 |
|  |  |  | HOMO–LUMO+2 (0.38) | 4.74 |

transition, highlighting the most significant contribution coming from conjugated double bonds.

The first excited singlet of Monocarbonyl curcumin is state 1, which can be assigned to the weak band at 2.81 eV (band I), which has contribution from orbitals HOMO and LUMO. Band II would be described as a mixture of the carbonyl group, benzene rings, and conjugated double bonds. In fact, by the calculations, none of the occupied MOs can be visualized as a 'clean' orbital of the carbonyl group or benzene (Figure 36 and Table 5).

We performed a deconvolution of the emission spectrum into two Gaussians to study the system's behavior in terms of dual emission and lifetime. The result follows in the figure 37. The areas under curves 1, labeled as G1, and 2, labeled as G2, are proportional to the number

**Figure 37** – *The spectral deconvolution of the emission spectra on excitation at 450 nm of CCM in in (a) methanol (top panel) and (b) acetonitrile (bottom panel).*
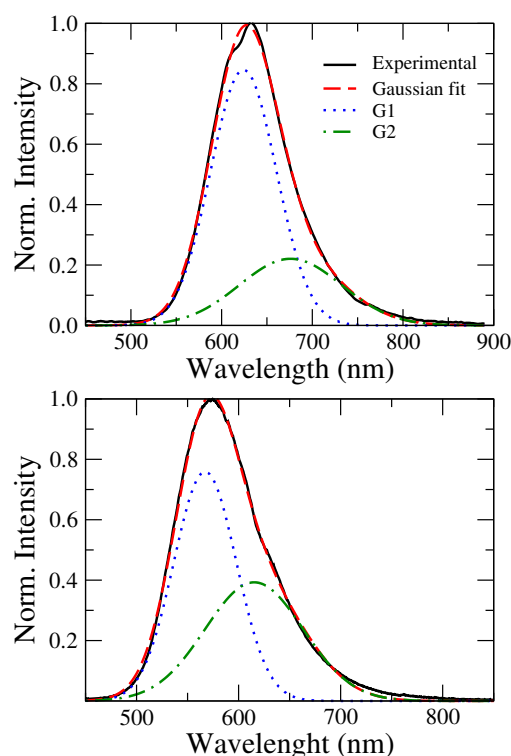


of molecules emitted from these excited states [43, 44], showing in table 6. Thus, the fraction of molecules that decay from 2 can be calculated as $A_2/A_T$, where $A_T$ is the total area under the fluorescence spectrum, $A_T = A_2 + A_1$ [43, 44]. The equation calculated the fraction of each excited state decay:

$$f_i = \frac{\alpha_i \tau_i}{\sum \alpha_i \tau_i}.$$

**Table 6** – *Spectral decomposition into Gaussians of Monocarbonyl curcumin in methanol, acetonitrile and aniline.*

| Solvents | Spectrum decomposition into Gaussian | |
|---|---|---|
| | $A_1/A_T$ | $A_2/A_T$ |
| Methanol | 0.71 | 0.29 |
| Acetonitrile | 0.55 | 0.45 |
| Aniline | 0.45 | 0.55 |

In both cases, the samples were photoexcited at 454 nm. As noted, the transient intensities exhibit a double exponential relaxation in both solvents, with the fluorescence lifetime presenting a strong dependence on the solvent polarity. In apolar solvent, the average lifetime is 0.3 ns,

**Figure 38** – *Fluorescence lifetime measurements of Monocarbonyl curcumin in acetonitrile ( black line) and toluene (blue line), upon photoexcitation at 454nm. The dashed lines are the best fitting curves using the expression $I(t) = a_1 * \exp(-t/\tau_1) + a_2 * \exp(-t/\tau_2)$*
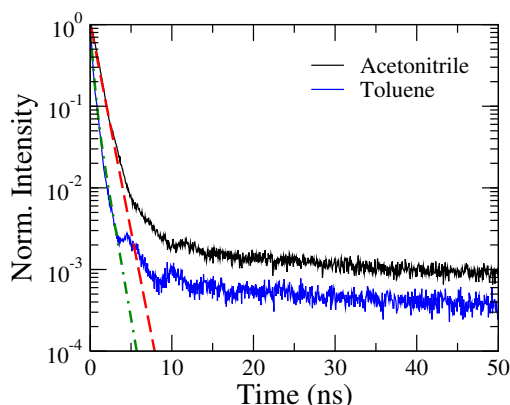


while the average lifetime of the excited state is $1.0$ ns in acetonitrile.

Figures 39 show the CCM emission spectra for different temperatures. The intensity of the emission decreases with increasing temperature, as is usual in fluorescence, but the shape of the curve remains constant. In our observations, we noticed a smaller decrease in emission when using acetonitrile as the solvent. This is because acetonitrile has a higher polarity, resulting in stronger solvent-solute interactions due to its high dipole moment. As a result, we were able to discern the influence of solvent polarity on emission sensitivity when exposed to changes in temperature.

**Figure 39** – *Steady-state fluorescence of Monocarbonyl curcumin in (a) acetonitrile and (b) toluene at different temperatures on excitation at 450 nm. A significant decrease in the fluorescence intensity is observed as the sample temperature is raised.*
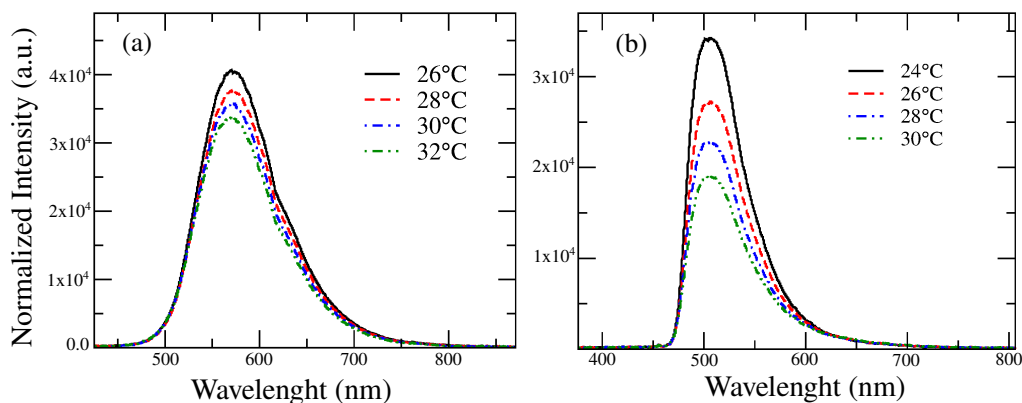
# UV-VIS SPECTROSCOPY OF CHALCONOID A COMPOUND

FLAVONOIDS are a vast group of prevalent plant secondary metabolites present in vascular plants such as ferns, conifers, and flowering plants [232, 233]. These natural compounds are typically classified into various categories based on their molecular structures, including chalcones, flavones, flavanones, flavanols, and anthocyanidins. Approximately 4000 types of flavonoids have been identified, many of which are vivid pigments that provide a range of yellow, red, and blue hues in flowers, fruits, and leaves [234, 235]. In addition to their role in plant coloration, flavonoids offer several pharmacological benefits, anticancer, anti-inflammatory, and anti-allergic. They are recognized as potent antioxidants, metal chelators, and free radical scavengers [232]. Both natural and synthetic flavonoids are of significant interest in the development of new therapeutic agents for various diseases and are generally considered non-toxic since they are widely present in the human diet [236–238]

Chalcones, natural phenols derived from chalcone (*(2E)-1,3-Diphenylprop-2-en-1-one*), represent one of the primary classes of flavonoids, found extensively in vegetables, fruits, tea, and soy [239]. Historical therapeutic applications of chalcones can be traced back to the ancient use of plants and herbs for treating different medical conditions [239, 240]. Recent studies have documented a broad range of significant pharmacological activities of chalcones, including antiproliferative, antioxidant, anti-inflammatory, and anticancer effects [241–244].

Kostanecki and Tambor were the first to synthesize a series of natural chromophoric products comprising $\alpha, \beta$-Unsaturated carbonyl bridge and termed them "chalcone" [245]. Chalcones are biologically active polyphenolic natural products. They serve as the natural precursors of flavonoids and isoflavonoids in higher plants [246]. At a chemical structural level, these phenolic compounds present two aromatic rings joined by a three-carbon $\alpha, \beta$-dihydroxy carbonyl system. Unlike other members of the flavonoids family, chalcones do not contain a heterocyclic *C* ring.

Chalcones play a vital role as precursors in the biosynthesis of flavones and flavanones.

They are usually synthesized from acetophenones and benzaldehydes via the Claisen-Schmidt condensation using a base in a polar solvent [247]. More advanced synthetic methods have been reported, such as the palladium-mediated Suzuki coupling between cinnamoyl chloride and phenylboronic acids [248, 249] and the carbonylative Heck coupling with aryl halides and styrenes in the presence of carbon monoxide [250, 251]. There is growing interest in the potential of chalcone derivatives from academia and industry. Their promising biological profiles and ease of synthetic manipulation have motivated the development of a series of novel chalcone-based compounds with diverse protective activities in single molecules. Chalcone derivatives' medicinal chemistry and therapeutic relevance are well-documented, with many reports highlighting the importance of the $\alpha, \beta$-Unsaturated carbonyl moiety in drug-target interactions and biological activity. [252–254].

**Figure 40** – *Optimized molecular structure of
(E)-1-(4-aminofenil)-3-(4-(dimetilamino)fenil)prop-2-en-1-ona using CAM-B3LYP functional.*
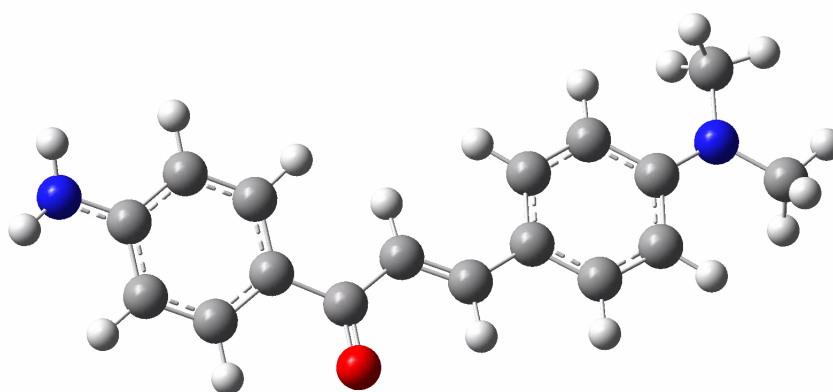


In this chapter, the focus was on the examination of the optical and electrochemical properties of a chalconoid compound,(E)-1-(4-aminophenyl)-3-(4-(dimethylamine)phenyl)prop-2-en-1-ona, labeled as CCN, synthesized by Luís Paulo from the Chemistry Department of the Federal University of Alagoas. These properties were explored through UV–vis absorption and fluorescence spectroscopy of their solutions in various solvents. Figure 40 illustrates the molecular structure of the chalconoid. TD-DFT and CAM-B3LYP were the tools to study the absorption energies in chalconoids embedded in acetonitrile and heptane.

## 9.1 SPECTROSCOPIC PROPERTIES

The optical properties of the synthesized chalconoid compound were studied using UV-vis spectroscopy. The CCN was dispersed in solvents with different polarities: heptane, toluene, dichloromethane, ethyl acetate, and acetonitrile. Fig.41 shows images of CCN solutions upon photoexcitation using a UV lamp, where a polarity-dependent fluorescence can be verified.

**Figure 41** – *Representantive images of chalconoid compound (CCN) dispersed in solvents with different polarities: a) ethyl acetate, (b) acetone, (c) dichloromethane, and (d) acetonitrile. The images were captured for the sample under room (top panel) and UV (bottom panel) light.*
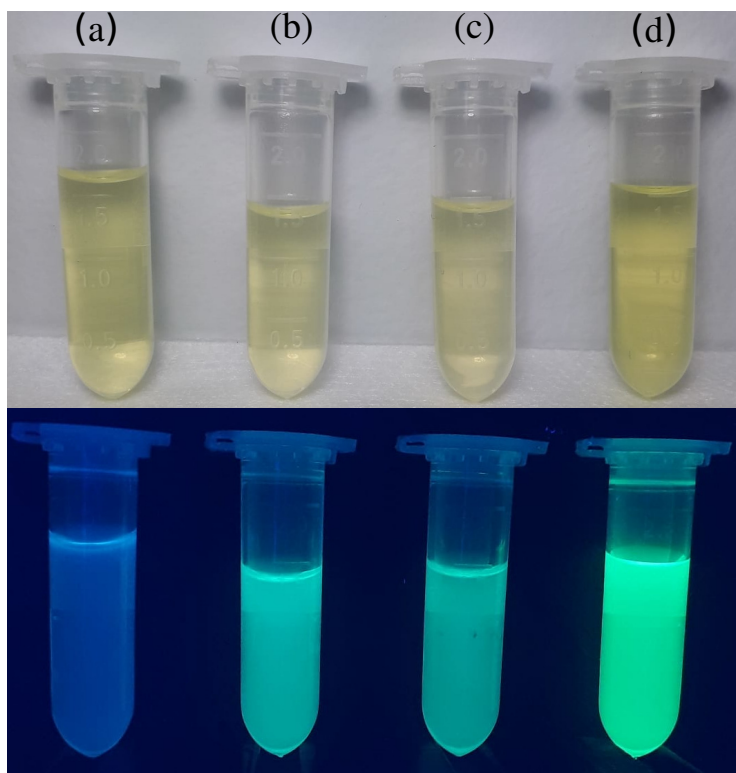


The absorption spectrum of the chalconoid is presented in Fig. 42, considering apolar and polar solvents. The compound exhibits two prominent absorption bands centered at 327 and 385 nm in heptane, usually denoted as bands I and II, respectively. In most chalconoid compounds, band I occurs in the 340-390 nm range, while band II occurs in the 220-270 nm range [255]. However, heteroatoms tend to induce a bathochromic shift of absorption bands, as observed in the CCN absorption spectrum. The absorption band centered at 327 nm can be attributed to a $\pi \rightarrow \pi^*$ electronic transition [256], involving an electronic delocalization along the cyclic

groups. The band I centered at 385 is associated with a $n \to \pi^*$ electronic transition involving the non-bonding electrons of nitrogen atoms in the dimethylamine group. For CCN dispersed in acetonitrile, a slight bathochromic shift in band I is observed, now placed at 399 nm. On the other hand, no shift in band II is observed as the solvent polarity increases. Table 7 summarizes the absorption data of CNN in different solvents.

**Figure 42** – *Absorption spectra of CCN chalconoid dispersed in a solvent with different polarities: heptane (solid black line) and acetonitrile (dashed red line). A small red shift is observed in the low energy band when CCN is dispersed in a polar environment.*
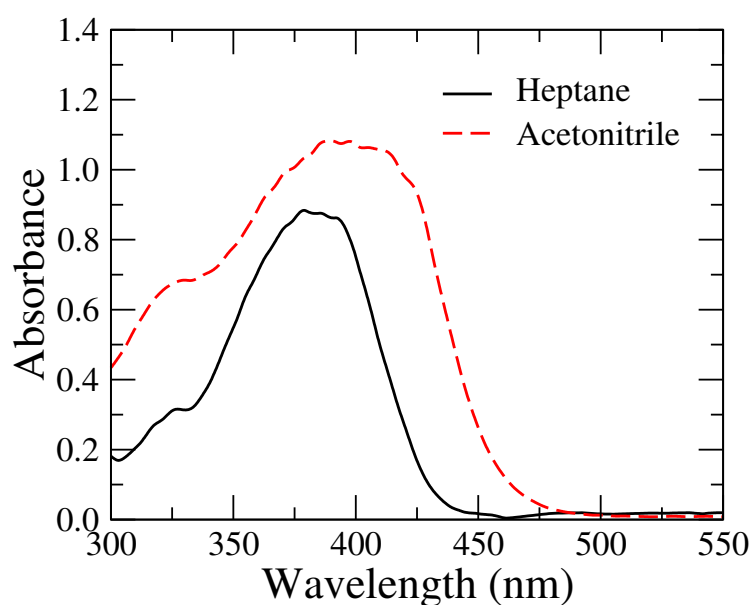


**Table 7** – *Location of the absorption peak $\lambda_{abs}$ for chalcone in various solvents.*

| Solvent | $\lambda_{abs}^{I}$ | $\lambda_{abs}^{II}$ |
|---|---|---|
| Heptane | 385 nm | 327 nm |
| Toluene | 392nm | 281 nm |
| Dichloromethane | 402 nm | 278 nm |
| Ethyl acetate | 391 nm | 249 nm |
| Acetonitrile | 399 nm | 246 nm |

Envisaging a better understanding and characterization of electronic transitions occurring in the CCN compound, theoretical calculations were performed using the TD-DFT approach. More specifically, frontier orbitals of CCN in acetonitrile and heptane were computed using CAM-B3LYP functional and the 6311+G(d,p) basis set. The solvent polarity was considered

using the State Specific PCM (Polarizable Continuum Model) calculations. The Linear Response method also estimates the low energy absorption band. The results are shown in the table 8. Although the LR method provides good results, state-specific PCM provides results that agree with the experimental findings.

**Table 8** – *Theoretical calculations of the absorption peak (band I) of CCN using Linear-Response Approach and State-Specific Solvation Correction.*

| Solvent | Linear-Response Approach | State-Specific Solvation Correction |
|---------|--------------------------|-------------------------------------|
| Acetonitrile | 365 nm | 395 nm |
| Heptane | 349nm | 362 nm |

Figure 43 displays the frontier orbitals for CCN, considering acetonitrile and heptane as solvents. Again, HOMO and LUMO levels were calculated TD-DFT at the CAM-B3LYP/6-311+G(d,p) level. For CCN in heptane, the electronic transition is a typical HOMO-LUMO transition, with an energy gap of 5.6 eV. In particular, TD-DFT simulations estimate that absorption band I is centered at 349 nm, with an oscillator strength of 1.29. The TD-DFT result for CCN in heptane is a few nanometers shifted about the experimental result ($\lambda_g^{exp} = 377$ nm). Considering the CCN dispersed in acetonitrile, the theoretical simulations also describe the band I as a HOMO-LUMO transition at 385 nm, with an oscillator strength of 1.47 and an energy gap of 5.4 eV. It is important to emphasize that The TD-DFT simulations reveal a pronounced intramolecular charge transfer occurs in CCN upon photoexcitation, involving the delocalization of non-nonbonding electrons in dimethylamine moiety attached in the aromatic ring.

Now, let us analyze the effects of solvents on CCCN photoluminescence. Fig. 44 shows the photoluminescence of CCN under photoexcitation at 454 nm. The chalconoid compound was dispersed in solvents with different polarities. CCN exhibits a broad emission in heptane with a single band centered at 563 nm. Considering the absorption peak at 377 nm, the Stokes shift is around 177 nm (8763 cm$^{-1}$). The fluorescence intensity increases significantly for CNN dispersed in acetonitrile, characterized by a single band centered at 537 nm. In this case, a hypsochromic shift occurs in the emission spectrum of CCN as the solvent polarity increases. Such a behavior is typical of compounds presenting a $n \rightarrow \pi^*$ electronic transition and a subsequent intramolecular charge transfer. As the absorption peak is 399 nm, the Stokes shift for CCN in acetonitrile is 138 nm (6441 cm$^{-1}$). The Stokes shift of CCH in different solvents is

**Figure 43** – *Frontier molecular orbitals (MOs) of CCN in (a) heptane and (b) acetonitrile, corresponding to HOMO-3, HOMO-1, HOMO, and LUMO levels.*
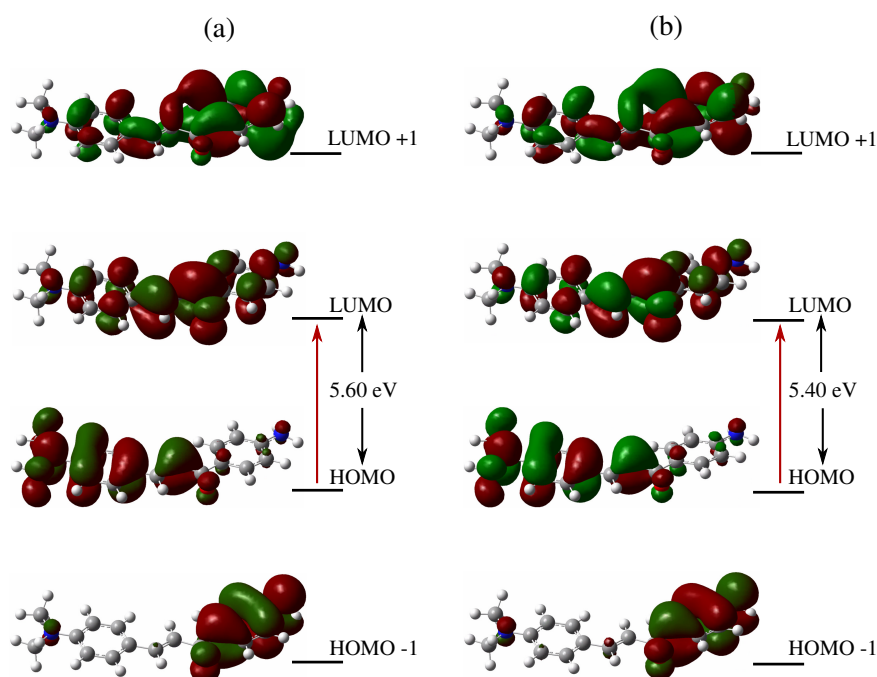


summarized in Table 9.

**Table 9** – *Stokes shift for chalcone in various solvents.*

| Solvent | $\lambda_{SS}$ |
| --- | --- |
| Heptane | 177nm |
| Toluene | 173 nm |
| Dichloromethane | 127nm |
| Acetonitrile | 138 nm |

The temperature dependence of CCN fluorescence is shown in Fig. 45(a), under photoexcitation at 450 nm. The sample temperature varied between 20 °C and 40 °C, corresponding to the interval of many biological applications. Acetonitrile was used as the carrier solvent. As the temperature increases, a pronounced reduction in the CCN emission intensity is observed without a significant change in the spectral distribution. However, the wavelength of CCN emission peak ($\lambda_p$) is slightly altered when environmental temperature increases, with $\lambda_p = 518$ nm at $T = 20°$C changing to $\lambda_p = 528$ nm at $T = 40°$C. Such a small thermochromic effect indicates that the gap energy between singlet excited and fundamental states is sensitive to the environmental conditions. More specifically, this result suggests that the molecular geometry is slightly

modified when the temperature is enhanced. These results agree with previous studies, where Ab Initio simulations verified that a small change in the energy gap occurs when chalconoid molecules are torsioned [256].

Fig. 45(b) presents the variation of the CCN emission intensity at the peak wavelength when the solvent temperature is varied. As one can observe, the emission intensity decreases monotonically as the solvent temperature increases, exhibiting an exponential dependence given by:

$$I(\lambda_p, T) = I_0 + I_1 e^{-\left(\frac{T-T_0}{\bar{T}}\right)} \quad , \tag{9.1}$$

where $I_0$ and $I_1$ are normalized residual and thermal intensity coefficients, $T_0$ is the reference temperature ($T_0 = 20°C$), and $\bar{T}$ defines the temperature range where the emission intensity decreases significantly. Using such an equation to fit the experimental data, we obtain $\bar{T} = 5.09°C$, $I_0 = 0.50$ and $I_1 = 0.53$, with correlation coefficient $R^2 = 0.998$ and $\chi^2 = 0.001$.

In order to investigate the solvation effects on the fluorescence kinetics of CCN, Fig. 46 shows the transient intensity of CCN emission. The time evolution of fluorescence intensities was measured at 575 nm for toluene and 537 nm for CCN dispersed at acetonitrile. In both cases, the samples were photoexcited at 454 nm. As noted, the transient intensities exhibit a

**Figure 45** – *(a) Normalized emission spectra of CCN in acetonitrile, considering different environmental temperatures: $T = 20°C$ (solid black line), $T = 26°C$ (dashed red line), $T = 32°C$ (dashed-dotted green line). (b) variation of CCN emission intensity at the peak wavelength as a function of the solvent temperature.*
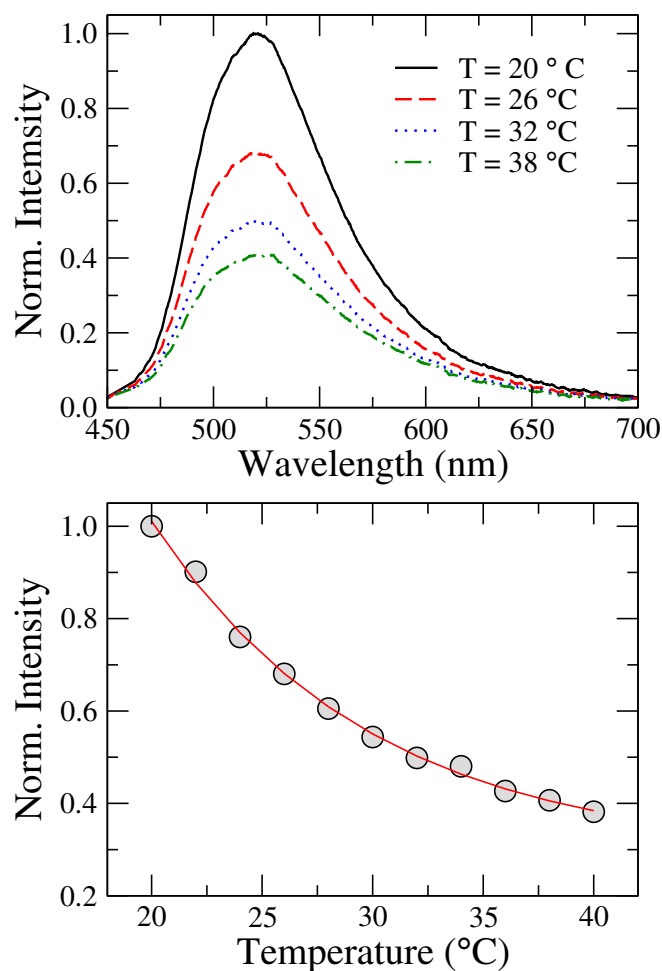


double exponential relaxation in both solvents, with the fluorescence lifetime presenting a strong dependence on the solvent polarity. More specifically, CCN presents a faster relaxation in the polar solvent than in the apolar solvent, reinforcing the polar nature of the excited state due to charge transfer. In apolar solvent, the average lifetime is $2.4$ ns, while the average lifetime of the excited state is $1.2$ ns in acetonitrile.

**Figure 46** – *Normalized transient intensity of CCN fluorescence for solvents with distinct polarities: toluene (black line) and acetonitrile (blue line). The dashed lines are the best fitting curves using the expression $I(t) = a_1 * \exp(-t/\tau_1) + a_2 * \exp(-t/\tau_2)$.*
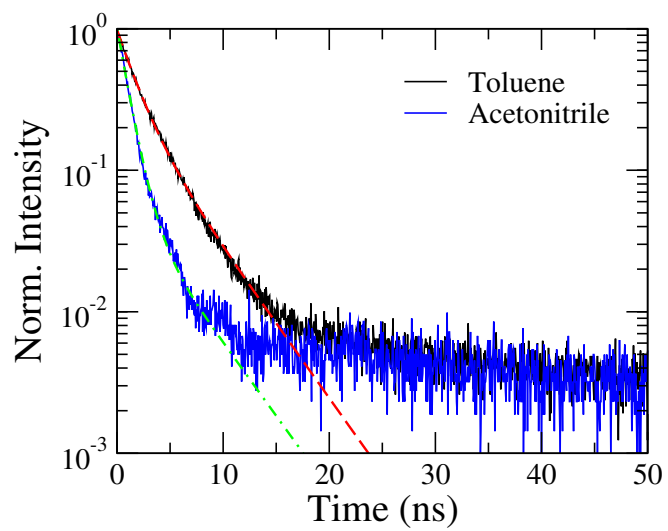
# CONCLUSION

The results reveal the significant influence of solvent polarity on the luminescence of PY-RES, evidenced by a sharp redshift and the modification in the spectral distribution as solvent polarity increases. This observation suggests the participation of different electronic states in the PY-RES emission mechanism, depending on the solvent medium. In nonpolar solvents, such as hydrocarbons, PY-RES exhibits a broad emission with strongly overlapping bands, while in polar solvents, two distinct emission bands are observed, with the lower energy band becoming predominant in highly polar media.

The dependence of the Stokes shift on solvent polarity was analyzed and correlated with the variation of the molecular dipole moment of PY-RES upon photoexcitation. The estimate of a variation of 4.57 D in the dipole moment, obtained through linear regression based on experimental and theoretical parameters, agrees with the literature for similar compounds, such as the sodium salt of resorufin. Furthermore, the thermochromatic study of PY-RES revealed a reduction in emission intensity with increasing temperature, which was more pronounced in less polar solvents such as dichloromethane. The absence of change in the spectral distribution indicates that temperature variation does not significantly alter the energy gap between the excited and ground states in a temperature range of 25 to 40 °C.

The sensitivity of PY-RES to solvent polarity highlights its potential as a physicochemical probe for detecting adulteration in solvents, such as in the mixture of ethanol and methanol. The ratiometric behavior of PY-RES emission against different volume fractions of methanol illustrates its applicability as a fluorescent sensor for detecting alcohol adulteration, with a change in emission color from green to magenta as the methanol concentration increases.

In this study, we investigated how different solvents influence the electronic absorption and fluorescence spectra of monocarbonyl curcumin *(1E,4E)-1,5-bis(4-(dimethylamino)phenyl)penta-1,4-dien-3-one (CCM)*. We complemented the experimental values with computational analyses, providing information on HOMO-LUMO orbitals and the effects of the solvent on the vertical

absorption and emission energies.

The results indicate that the solvent's polarity strongly affects the fluorescence spectrum of curcumin monocarbonyl. The absorption maxima of CCM ranged from 400 nm to 460 nm, depending on the polarity of the solvent. A bathochromic (red) shift in the absorption maxima was observed as the solvent polarity increased, reaching a maximum value of 458 nm in methanol, which has a high dielectric constant. Computer simulations performed for CCM in methanol using the B3LYP functional revealed that the HOMO-LUMO spacing in curcumin monocarbonyl occurs at 2.8 eV, with a theoretical absorption peak at 484 nm, close to the experimental value in methanol. In addition, the $\pi \rightarrow \pi^*$ transition was identified at 297 nm and $n \rightarrow \pi^*$ at 497, confirming the experimentally observed behavior. In the emission spectrum, CCM compound showed a high Stokes shift in methanol (175.6 nm), which increased with solvent polarity. This evidences the solvent environment's significant influence on the excited molecule's charge distribution.

The spectral decomposition into Gaussian components showed that the dual emission intensity distribution between two excited states was solvent-dependent, with variable proportions between acetonitrile, methanol and aniline, but with constant spectral shapes, which is in agreement with the Kasha-Vavilov rule. Finally, fluorescence studies at different temperatures indicated that the emission intensity decreases with increasing temperature while the spectrum's shape remains constant. This suggests that solvent-solute interactions, influenced by solvent polarity, play a crucial role in the stability of the emissive properties of curcumin monocarbonyl under different thermal conditions.

This study not only elucidates the photochemical and photophysical behavior of curcumin monocarbonyl in different solvents, but also underscores the impact of intermolecular interactions on its optical properties. These findings open up the potential use of this molecule as an environment-sensitive probe for applications in analytical chemistry and fluorescent materials, inspiring further research and development in these fields.

Finaly, this study conducted an in-depth analysis of the optical and electrochemical properties of the chalconoid *(E)-1-(4-aminophenyl)-3-(4-(dimethylamino)phenyl)prop-2-en-1-one*. The investigation encompassed both spectroscopic experiments and theoretical calculations, providing a comprehensive understanding of the compound's behavior in different solvent environments.

The UV-vis spectroscopy results revealed two leading absorption bands attributed to the

$\pi \rightarrow \pi^*$ and $n \rightarrow \pi^*$ transitions, whose locations varied significantly according to the solvent used. A bathochromic shift in the absorption bands was observed, especially in less polar solvents such as heptane and toluene, indicating the solvent environment's influence on the chalconoid's molecular interactions.

Using the CAM-B3LYP functional and the 6-311+G(d,p) basis set, theoretical analysis corroborated the experimental data and allowed a deeper understanding of the electronic transitions involved. The HOMO-LUMO transition, with an energy gap of 5,406 eV in acetonitrile, was consistently associated with the $\pi \rightarrow \pi^*$ transition, while the $n \rightarrow \pi^*$ transition presented a gap of 6.5 eV. The comparison between the solvatochromism calculations by Linear-Response Approach and State-Specific Solvation Correction indicated that the latter method accurately describes the interaction between the solute and the solvent, especially in acetonitrile.

The fluorescence of the chalconoid, when excited at 454 nm, demonstrated a significant Stokes shift in nonpolar solvents, such as heptane and toluene, reinforcing the influence of the solvent environment on the emissive properties of the compound. This behavior underscores the potential of chalcones in optoelectronic applications, inspiring hope for future advancements in these field.

# Bibliography

[1] Reichardt C, Welton T. Solvents and Solvent Effects in Organic Chemistry. 2011. Citado na pág. 18, 102, 103.

[2] Higashi Y, Kiyonaka S, Hamachi I. Fluorescent probes for sensing and imaging within specific cellular organelles. Accounts of Chemical Research. 2016;49(11):2459-67. Citado na pág. 19.

[3] Qian X, Lin W. Fluorescent Chemosensors: The Past, Present and Future. Sensors. 2017;17(12):2774.

[4] Demchenko AP. Introduction to Fluorescence Sensing. Springer Science Business Media; 2008.

[5] New EJ. Molecular Fluorescent Sensors for Cellular Studies. John Wiley Sons; 2022. Citado na pág. 19.

[6] Zhu H, Fan J, Du J. Fluorescent probes for sensing and imaging within specific cellular organelles. Accounts of Chemical Research. 2016;49(10):2115-26. Citado na pág. 19.

[7] Erdmann RS, Weiss S. Fluorescence imaging of single molecules and nanostructures for genomic, proteomic, and cellular biophysical applications. Annual Review of Analytical Chemistry. 2015;8(1):89-109.

[8] Xu W, Zeng Z, Jiang JH, Chang YT, Yuan L. Discriminating nucleic acids with fluorescent small molecules. Chemical Society Reviews. 2016;45(10):3039-51.

[9] Liu Y, Zhou J, Wang L. Fluorescent probes for environmental sensing and cellular imaging. Chemical Communications. 2017;53(9):1483-502. Citado na pág. 19.

[10] Wu D, Sedgwick AC, Gunnlaugsson T, Akkaya EU, Yoon J, James TD. Fluorescent chemosensors: the past, present and future. Chemical Society Reviews. 2017;46(23):7105-23. Citado na pág. 19.

[11] Grimm JB, English BP, Chen J, Slaughter JP, Zhang Z, Revyakin A, et al. A general method to improve fluorophores for live-cell and single-molecule microscopy. Nature Methods. 2015;12(3):244-50.

[12] Jiang S, Cakmak FP, Yoon J. Recent advances in the development of chromeno[2,3-b] pyrrole-based organic fluorophores. Dyes and Pigments. 2020;174:108008. Citado na pág. 19.

[13] Newton I. Opticks: or, A Treatise of the Reflexions, Refractions, Inflexions and Colours of Light. Independent science publisher; 1704. Citado na pág. 19.

[14] Young T. The Bakerian Lecture: Experiments and Calculations Relative to Physical Optics. Philosophical Transactions of the Royal Society of London. 1804;94:1-16. Citado na pág. 19.

[15] Maxwell JC. VIII. A dynamical theory of the electromagnetic field. Philos Trans R Soc Lond. 1865 dec;155(0):459-512. Citado na pág. 19.

[16] Planck M. On the Theory of the Energy Distribution Law of the Normal Spectrum. Annalen der Physik. 1900. Citado na pág. 19.

[17] Zur Elektrodynamik bewegter K{orper Citado na pág. 20.
, author = Einstein, A, journal = Ann. Phys., publisher = Wiley, volume = 322, number = 10, pages = 891–921, year = 1905,.

[18] Lopez-Garcia M, Fonseca L. Photovoltaic Effect in Solar Cells. Energy Procedia. 2019;158:1568-73. Citado na pág. 20.

[19] Kato H, Kamada K. X-ray detectors based on the photoelectric effect. Journal of Instrumentation. 2017;12(01):C01048. Citado na pág. 20.

[20] Saleem M, Rehman MA, Akhtar J, Butt MA, Khawaja EE. Review of Photoelectric Effect and its Applications in Optical Sensors. Journal of Nanoelectronics and Optoelectronics. 2019;14(5):566-74. Citado na pág. 20.

[21] Schrödinger E. Quantization as a Problem of Proper Values, Part II. Annalen der Physik. 1926;385(13):437-90. Citado na pág. 20.

[22] Hecht E. Optics. 5th ed. New York: Pearson; 2017. Citado na pág. 20, 44.

[23] Almeida CES, Kuplich TM, de Oliveira CP, Santos TT, de Mello JF, Oliveira G. Variation of the spectral signature of remote sensing data from land and water surfaces by the angle of incidence of solar radiation. Applied Optics. 2017;56(35):9723-33. Citado na pág. 20.

[24] Chen H, Li H, Liu Y, Zhou F, Li H, Zhang X. Design of high-performance grating couplers for silicon-on-insulator-based photonic integrated circuits. Applied optics. 2018;57(3):509-14. Citado na pág. 20.

[25] Valeur B, Berberan-Santos MN. A Brief History of Fluorescence and Phosphorescence before the Emergence of Quantum Theory. Journal of Chemical Education. 2011 06;88:731-8. Citado na pág. 20, 21.

[26] BRASLAVSKY SE. Glossary of terms used in photochemistry, 3rd edition (IUPAC Recommendations 2006). Research Triangle Park, Nc Iupac; 2007. Citado na pág. 20.

[27] Haüy RJ. Traité de minéralogie; 1822. Citado na pág. 21.

[28] Valeur B, Berberan-Santos MN. A brief history of fluorescence and phosphorescence before the emergence of quantum theory. Journal of Chemical Education. 2012;89(6):731-8. Citado na pág. 21, 22.

[29] Harris E. The Immune System: A Personal Odyssey. 1st ed. Elsevier; 2013. Citado na pág. 22.

[30] Lakowicz JR. Principles of Fluorescence Spectroscopy. 3rd ed. New York: Springer; 2006. Citado na pág. 22, 38, 41, 43, 51, 52.

[31] Kuhn A, Winterhalter K. Emission de la lumière par une èspèce nouvelle de méduse. Comptes rendus de l'Académie des Sciences. 1949;228:963-5. Citado na pág. 22.

[32] Haddock SH, Dunn CW. Bioluminescence spectra of shallow and deep-sea gelatinous zooplankton: ctenophores, medusae and siphonophores. Marine Biology. 2005;146(2):949-57. Citado na pág. 23.

[33] Culture GA. Alarm Jellyfish; 2023. Acesso em: 04 de março de 2023. Disponível em: https://artsandculture.google.com/asset/alarm-jellyfish/tAEURl4fmTScfw?hl=en. Citado na pág. 23.

[34] Roth MS, Deheyn DD. Fluorescent proteins and in vivo imaging in reef corals. Marine Biotechnology. 2007;9:577-83. Citado na pág. 24.

[35] Salih A, Larkum A, Cox G, Kühl M, Hoegh-Guldberg O. Fluorescent pigments in corals are photoprotective. Nature. 2000;408:850-3. Citado na pág. 24.

[36] Xin Y, Liu Y, Li J. Probing the Molecular Mechanism of the Interaction between Bovine Serum Albumin and Oleuropein by Fluorescence Spectroscopy. Journal of Agricultural and Food Chemistry. 2020;68(41):11212-20. Citado na pág. 24.

[37] Wang Y, Kang Q, Liu Y, Liu L, Zhang J, Huang W, et al. An enzyme-free signal amplification assay for ultrasensitive detection of protein based on a fluorescence resonance energy transfer strategy. Analytica Chimica Acta. 2016 feb;907:146-52. Available from: https://doi.org/10.1016/j.aca.2015.12.024.

[38] Cao X, Luo J, Zhao L, Ren J, Hao Z, Chen Q, et al. The Anthocyanin Compound of Purple Sweet Potato Color Attenuates Hepatic Lipid Accumulation through the Insulin Signaling Pathway in HepG2 Cells. Biochemistry. 2019;58(45):4492-500.

[39] Pan H, Zhang J, He D, Wang H, Wang Y, Chen R, et al. Deep-Red Fluorescent Probe for Imaging Lysosomal pH Fluctuation in Live Cells, Tissues, and Zebrafish. Analytical Chemistry. 2016;88(3):1917-23.

[40] Chowdhury S, Chandra P. Fluorescence-based techniques to investigate protein interactions in living cells: a concise review. Methods and Applications in Fluorescence. 2019;7(1):012001. Citado na pág. 24.

[41] Miolo G. Light in Forensic Science. European Society for Photobiology; 2018. Citado na pág. 24.

[42] Rout B. A Miniaturized Therapeutic Chromophore for Multiple Metal Pollutant Sensing, Pathological Metal Diagnosis and Logical Computing. Scientific Reports. 2016 06;6. Citado na pág. 24.

[43] Vequi-Suplicy CC, Coutinho K, Lamy MT. New Insights on the Fluorescent Emission Spectra of Prodan and Laurdan. Journal of Fluorescence. 2015 03;25:621-9. Citado na pág. 25, 115.

[44] Vequi-Suplicy CC, Orozco-González Y, Lamy MT, Canuto S, Coutinho K. A new interpretation of the absorption and the dual fluorescence of Prodan in solution. Journal of Chemical Physics. 2020 12;153. Citado na pág. 25, 115.

[45] Bhattacharya B, Jana B, Bose D, Chattopadhyay N. Multiple emissions of benzil at room temperature and 77 K and their assignments from <i>ab initio</i> quantum chemical calculations. The Journal of Chemical Physics. 2011 01;134. Citado na pág. 25.

[46] Thomson JJ. XL. Cathode Rays. The London, Edinburgh, and Dublin Philosophical Magazine and Journal of Science. 1897 10;44:293-316. Citado na pág. 28.

[47] Nagaoka H. LV. <i>Kinetics of a system of particles illustrating the line and the band spectrum and the phenomena of radioactivity</i>. The London, Edinburgh, and Dublin Philosophical Magazine and Journal of Science. 1904 05;7:445-55. Citado na pág. 28.

[48] Rutherford E. LXXIX. The scattering of and particles by matter and the structure of the atom. The London, Edinburgh, and Dublin Philosophical Magazine and Journal of Science. 1911 05;21:669-88. Citado na pág. 28.

[49] Bohr N. I. On the constitution of atoms and molecules. The London, Edinburgh, and Dublin Philosophical Magazine and Journal of Science. 1913 07;26:1-25. Citado na pág. 28.

[50] Mulliken RS. Electronic Structures of Polyatomic Molecules and Valence. Physical Review. 1932 04;40:55-62. Citado na pág. 28.

[51] Mulliken RS. Electronic Structures of Polyatomic Molecules and Valence. II. General Considerations. Physical Review. 1932 07;41:49-71. Citado na pág. 28.

[52] Griffiths DJ. Introduction to quantum mechanics. Cambridge University Press; 2017. Citado na pág. 28.

[53] Ratner MA, Schatz GC. Introduction to quantum mechanics in chemistry. Prentice Hall; 2001.

[54] Feynman RP. The Feynman Lectures On Physics, The Definitive Edition Volume 1, 2/E. Pearson Education India; 2008. Citado na pág. 28.

[55] Atkins PW, Paula JD. Atkins' Physical chemistry. Oxford University Press; 2014. Citado na pág. 29.

[56] Bais S. The Equations. Amsterdam University Press; 2005. Citado na pág. 29.

[57] Frenkel D, Smit B. Understanding molecular simulation : from algorithms to applications. Academic Press; 2002. Citado na pág. 29.

[58] Atkins P, de Paula J. Physical Chemistry. 11th ed. Oxford University Press; 2018. Citado na pág. 29, 41, 45, 47, 50.

[59] Vautherin D, Brink DM. Hartree-Fock Calculations with Skyrme's Interaction. I. Spherical Nuclei. Physical Review C. 1972 03;5:626-47. Citado na pág. 29.

[60] Levitus M. Mathematical Methods in Chemistry. Springer-Verlag; 2005. Citado na pág. 29.

[61] Lamoureux G, Ogilvie J. ORBITALS IN GENERAL CHEMISTRY, PART II: MATHE-MATICAL REALITIES. Química Nova. 2020. Citado na pág. 29.

[62] Szabo A, Ostlund NS. Modern Quantum Chemistry: Introduction to Advanced Electronic Structure Theory. Courier Corporation; 1996. Citado na pág. 29, 61, 65, 71, 72, 73, 76.

[63] Autschbach J. Hydrogen like Atoms. Oxford University Press eBooks. 2020 12:328-39. Available from: https://academic.oup.com/book/43692/chapter-abstract/367014453?redirectedFrom=fulltext&login=false. Citado na pág. 29.

[64] Hydrogen like atom;. Available from: https://www.chemeurope.com/en/encyclopedia/Hydrogen-like_atom.html. Citado na pág. 29.

[65] Slater JC. Atomic Shielding Constants. Physical Review. 1930 07;36:57-64. Citado na pág. 30.

[66] Slater orbital - Knowino;. Available from: https://www.theochem.ru.nl/~pwormer/Knowino/knowino.org/wiki/Slater_orbital.html. Citado na pág. 30.

[67] Mcquarrie DA. Quantum chemistry. University Science Books; 2008. Citado na pág. 30.

[68] Vieira VM. Estudo das Propriedades Espectroscopicas de Moléculas Orgânicas em Solução Utilizando a Combinação do Modelo Contínuo PCM e o Metodo Sequencial QM/MM. Instituto de Física - UFAL; 2010. Citado na pág. 31, 66, 72, 73, 75, 77, 78, 81, 84, 85.

[69] Rauk A. Orbital Interaction Theory of Organic Chemistry. John Wiley Sons; 2004. Citado na pág. 32.

[70] Jorgensen W. The Organic Chemist's Book of Orbitals. Elsevier; 2012. Citado na pág. 32, 33, 34.

[71] Angarov V, Kozuch S. On the $\sigma$, $\pi$ and $\delta$ hole interactions: A molecular orbital overview. New Journal of Chemistry. 2018;42(2):1413-22. Citado na pág. 33.

[72] Gates C. Molecular Orbital Theory — Overview Application;. Available from: https://www.expii.com/t/molecular-orbital-theory-overview-application-8363. Citado na pág. 33.

[73] University MRS. 1. Overlapping AO must have close energies.;. Available from: https://studfile.net/preview/9870453/page:9/. Citado na pág. 34.

[74] Eames E. MO diagrams for Diatomic Molecules;. Available from: http://www.graylark.com/eve/MO-homodiatomics.html. Citado na pág. 34, 35.

[75] McHale JL. Molecular Spectroscopy. Upper Saddle River, NJ: Prentice Hall; 1999. Citado na pág. 36.

[76] Reichardt C. Solvatochromic dyes as solvent polarity indicators. Chemical Reviews. 2003;103:4145-76. Citado na pág. 38.

[77] Vogler EA, Quinn JR, Swager TM. Dyes in Liquid Crystals: Effects of Dye Structure on Order and Electronic Properties. Chemistry of Materials. 2008;20:848-55.

[78] Matsumoto K, Maruyama T, Nishide H, Kimura M, Maeda K, Aida T. Chromophore-functionalized dendrons: Solubility control and self-assembly. Macromolecules. 2004;37:3731-7. Citado na pág. 38.

[79] Asplund M, Grevesse N, Sauval AJ, Scott P. The chemical composition of the Sun. Annual Review of Astronomy and Astrophysics. 2009;47:481-522. Citado na pág. 39.

[80] Pavia DL, Lampman GM, Kriz GS, Vyvyan JA. Introduction to Spectroscopy. 5th ed. Stamford, CT: Cengage Learning; 2014. Citado na pág. 39, 48.

[81] Ojeda J, Dittrich M. Fourier Transform Infrared Spectroscopy for Molecular Analysis of Microbial Cells. Methods in molecular biology (Clifton, NJ). 2012 04;881:187-211. Citado na pág. 40.

[82] Skoog DA, Holler FJ, Crouch SR. Principles of Instrumental Analysis. Cengage Learning; 2017. Citado na pág. 41.

[83] Schwille P, Enderlein J, Haustein T. Fluorescence correlation spectroscopy: exploring the structure and dynamics of molecules. Nature methods. 2005;2(10):717-26. Citado na pág. 43.

[84] Kokate RK, Harle SM, Jadhav SM. Fluorescence: A Powerful Tool for the Detection of Biomolecules. Advanced Materials Letters. 2015;6(12):1001-5. Citado na pág. 43.

[85] Li J, Nomura H, Nakamura M, et al. White Organic Light-Emitting Diodes Based on Thermally Activated Delayed Fluorescence Emitters. Advanced Materials. 2013;25(27):3701-5.

[86] Harada M, Kuroki S, Itoh K, et al. Quantitative Imaging of Intracellular O2 Concentration in a Small Tissue-Like Sample Based on the Phosphorescence Lifetime of Pd(II) Mesoporphyrin IX. Analytical Chemistry. 2016;88(5):2675-81.

[87] Chen S, Zhou J, Zhao X, et al. A Red Phosphorescent Probe for Two-Photon Imaging of Hypochlorous Acid in Live Cells and Tissues. Analytical Chemistry. 2017;89(9):5018-24.

[88] Wojciechowski RJ, Law ALJ, Fernández JJ, et al. In vivo quantification of oxygen gradients and tumour hypoxia using 19F magnetic resonance imaging and spectroscopy. Magnetic Resonance Materials in Physics, Biology and Medicine. 2017;30(6):527-41. Citado na pág. 43.

[89] Richmond A. Handbook of Microalgal Culture. Blackwell Science; 2004. This unit is called an Einstein (E = 6.023×1023 quanta). Citado na pág. 44.

[90] McCree KJ. Photosynthetically Active Radiation. Springer; 1981. In photobiology, a mole (Avogadro's number, 6.022×1023) of photons is commonly referred to as an einstein (E).

[91] Incoll LD, Long SP, Ashmore MA. SI units in publications in plant science. Commentaries in Plant Science. 1981;2:83-96. Citado na pág. 44.

[92] Herzberg G. Molecular Spectra and Molecular Structure: I. Spectra of Diatomic Molecules. Krieger Publishing Company; 1989. Citado na pág. 45.

[93] Clague AD, Jones AC. The use of gas-phase UV spectra in the 168-330-nm wavelength region for analytical purposes. 1. Qualitative measurements. Analytical Chemistry. 1981;53(3):425-30. Citado na pág. 45.

[94] Levine IN. Physical Chemistry. 6th ed. McGraw-Hill Education; 2013. Citado na pág. 45.

[95] Becker J, Hegelich BM, Jung D, Karsch L, Kiefer D, Klimo O, et al. Optical spectroscopy of laser-produced plasmas for standoff isotopic analysis. Journal of Analytical Atomic Spectrometry. 2016;31(2):405-12. Citado na pág. 46.

[96] Franck J, Condon EU. The Franck-Condon principle and its application to crystals. Journal of Chemical Physics. 1926;1(4):850-7. Citado na pág. 47.

[97] Atkins PW, Friedman RS. Molecular Quantum Mechanics. 5th ed. New York, NY: Oxford University Press; 2010. Citado na pág. 47.

[98] Chemistry L. The Effect of Conjugation on max; 2021. Accesso: 08 de abril de 2023. Available from: https://chem.libretexts.org/Bookshelves/Organic_Chemistry/. Citado na pág. 47, 48.

[99] Hollas JM. Modern Spectroscopy. 4th ed. Chichester, England: John Wiley & Sons; 2004. Citado na pág. 48.

[100] Jameson DM. Introduction to Fluorescence. CRC Press; 2014. Citado na pág. 49.

[101] Almokhtar M, Smith RJ, Shukla M. Fluorescence intensity and lifetime detection beyond the shot-noise limit using lock-in detection and intensified CCD camera. Journal of fluorescence. 2019;29(2):431-41. Citado na pág. 50.

[102] Moore EG, Weissleder R. Fluorescence quantum yield measurements in the presence of upconversion via energy transfer. Journal of the American Chemical Society. 2012;134(3):1310-3.

[103] Zheng H, Ou Z. A simple and efficient approach to calculate the quantum yield of fluorescence resonance energy transfer in solution. Journal of Chemical Education. 2018;95(7):1255-61.

[104] Isaacson M, McHale K. Monte Carlo simulations of fluorescence from multiple dipole emitters in an optical trap. Journal of biomedical optics. 2013;18(2):025005. Citado na pág. 50.

[105] Eiring P. Super-resolution microscopy of plasma membrane receptors; 2021. Citado na pág. 51.

[106] Sowoidnich K, Kochan K, Baranska M, Schulz H. Spectroscopic Methods for Analysis of Food Safety and Quality. Applied Spectroscopy Reviews. 2017;52(8):723-49. Citado na pág. 54.

[107] Revin DG, Dmitrieva TV, Romanovskaya VE. Infrared Spectroscopy in the Detection and Identification of Microorganisms: A Review. Applied Spectroscopy Reviews. 2018;53(7):581-604.

[108] Ferreira TDD, Marques AS, Lima SC, Neto MMM. Ultraviolet–Visible and Fluorescence Spectroscopy in the Characterization of Aquatic Dissolved Organic Matter: An Overview. Water (Switzerland). 2020;12(1):189. Citado na pág. 54.

[109] Li G, Feng D, Zhou HC. Applications of UV–Vis absorption spectroscopy in the characterization of metal–organic frameworks. Coordination Chemistry Reviews. 2019;378:204-27. Citado na pág. 54.

[110] Sokolov VV, Mokrushina GV, Galkina AV. UV–vis absorption spectroscopy in organic synthesis. Russian Chemical Reviews. 2018;87(2):140-68.

[111] Kumar A, Dutta K, Kondaiah C, Chakraborty S. UV-visible spectroscopy-based determination of the binding constant of cucurbituril with small organic guest molecules in aqueous solutions. Journal of Photochemistry and Photobiology A: Chemistry. 2021;402:112851. Citado na pág. 54.

[112] Liu Z, Feng X, Sun Y, Yang G, Zhang T. A new approach to infrared and Raman spectroscopy for monitoring the reaction process of organic synthesis in situ. RSC Advances. 2017;7(42):26447-55. Citado na pág. 54.

[113] Krasnoshchekov SV, Yudina TV, Aleksandrovsky AS, Solovyev AA, Popov AK. Detection of optical vortices by Raman spectroscopy: An implementation via a radial gradient filter. Spectrochimica Acta Part A: Molecular and Biomolecular Spectroscopy. 2019;213:191-5.

[114] Wu J, Ma Y, Wang B, Zhang W, Chen Z, Chen H, et al. Microstructural changes of biochar during anaerobic digestion determined by FTIR and Raman spectroscopy. Journal of Environmental Sciences. 2021;101:177-87. Citado na pág. 54.

[115] W. Absorbance Detection; 2019. Available from: https://www.wpiinc.com/blog/post/absorbance-detection. Citado na pág. 55.

[116] Lakowicz JR. Principles of fluorescence spectroscopy; 2006. Citado na pág. 56.

[117] Installation and Operation Manual - USB2000+ Fiber Optic Spectrometer;. Citado na pág. 57.

[118] ;. Citado na pág. 58.

[119] Valeur B, Berberan-Santos MN. Molecular Fluorescence: Principles and Applications, Second Edition; 2012. Citado na pág. 58, 60.

[120] Barrows J, Smith P. Computational modeling in applied physics. Journal of Applied Physics. 2016;120(3):035101. Citado na pág. 61.

[121] LeVeque RJ. Finite volume methods for hyperbolic problems. Cambridge Texts in Applied Mathematics. 2007;31.

[122] Holgate S, Jones P. Climate modeling and simulation: An introduction. Journal of Climate. 2012;25(20):641-51.

[123] Aluru S, Sulakhe D. Computational methods in systems biology. Annual Review of Biophysics. 2015;44:5-25.

[124] Liu G. Meshfree methods: moving beyond the finite element method. CRC Computational Mechanics and Applied Analysis Series. 2014;2. Citado na pág. 61.

[125] Parr RG, Yang W. Density-functional theory of atoms and molecules. Oxford University Press; 1989. Citado na pág. 62, 78.

[126] Burke K. Perspective on density functional theory. The Journal of Chemical Physics. 2012;136(15):150901. Citado na pág. 62, 78.

[127] Born M, Oppenheimer R. Zur Quantentheorie der Molekeln. Annalen der Physik. 1927;389(20):457-84. Available from: https://onlinelibrary.wiley.com/doi/abs/10.1002/andp.19273892002. Citado na pág. 63.

[128] Jensen F. Introduction to Computational Chemistry. 2nd ed. Chichester, England: John Wiley & Sons; 2007. Citado na pág. 70.

[129] Helgaker T, Jørgensen P, Olsen J. Molecular Electronic-Structure Theory. John Wiley & Sons; 2014. Citado na pág. 72.

[130] Helgaker T, Jørgensen P, Olsen J. Molecular Electronic-Structure Theory. Chemical reviews. 2000;100(10):4157-206. Citado na pág. 72.

[131] Møller C, Plesset MS. Note on an Approximation Treatment for Many-Electron Systems. Physical Review. 1934;46(7):618-22. Citado na pág. 73.

[132] Helgaker T, Watson M, Handy NC. Basis-set convergence of correlated calculations on Ne, N2, and H2O. Chemical Physics Letters. 2000;332(3-4):603-9. Citado na pág. 73.

[133] Hohenberg P, Kohn W. Inhomogeneous electron gas. Physical Review. 1964;136(3B):B864-71. Citado na pág. 78, 79.

[134] Becke AD. Density-functional thermochemistry. III. The role of exact exchange. The Journal of Chemical Physics. 1993;98(7):5648-52. Citado na pág. 78.

[135] Cohen AJ, Mori-S'anchez P, Yang W. Insights into current limitations of density functional theory. Science. 2008;321(5890):792-4. Citado na pág. 78.

[136] Becke AD. Density-functional exchange-energy approximation with correct asymptotic behavior. Physical Review A. 1988;38(6):3098-100. Citado na pág. 78, 85.

[137] Cramer CJ. Essentials of Computational Chemistry: Theories and Models. 2nd ed. Wiley; 2016. Citado na pág. 78.

[138] Kohn W, Sham L. Self-consistent equations including exchange and correlation effects. Physical Review. 1965;140(4A):A1133. Citado na pág. 80, 85.

[139] Dreizler R, Gross E. Density Functional Theory: An Approach to the Quantum Many-Body Problem. Springer-Verlag Berlin Heidelberg; 1990. Citado na pág. 80.

[140] Martin RM. Electronic Structure: Basic Theory and Practical Methods. Cambridge University Press; 2008. Citado na pág. 82.

[141] Janak JF. Proof that E n i= $\varepsilon$ in density-functional theory. Physical Review B. 1978;18(12):7165. Citado na pág. 82.

[142] Perdew J, Tao J, Kümmel S, Wilson A, Peterson K. Recent Advances in Electron Correlation Methodology. edited by AK Wilson and KA Peterson, ACS Books, Washington, DC. 2004. Citado na pág. 85.

[143] Perdew JP, Burke K, Ernzerhof M. Generalized gradient approximation made simple. Physical review letters. 1996;77(18):3865. Citado na pág. 85, 87.

[144] Langreth DC, Mehl M. Beyond the local-density approximation in calculations of ground-state electronic properties. Physical Review B. 1983;28(4):1809. Citado na pág. 85.

[145] Perdew JP, Chevary JA, Vosko SH, Jackson KA, Pederson MR, Singh DJ, et al. Atoms, molecules, solids, and surfaces: Applications of the generalized gradient approximation for exchange and correlation. Physical review B. 1992;46(11):6671. Citado na pág. 85.

[146] Van Voorhis T, Scuseria GE. A novel form for the exchange-correlation energy functional. The Journal of chemical physics. 1998;109(2):400-10. Citado na pág. 86.

[147] Tao J, Perdew JP, Staroverov VN, Scuseria GE. Climbing the density functional ladder: Nonempirical meta–generalized gradient approximation designed for molecules and solids. Physical review letters. 2003;91(14):146401. Citado na pág. 86.

[148] Becke A. The X3LYP extended density functional for accurate descriptions of nonbond interactions, spin states, and thermochemical properties. Chemical Physics. 1993;98:5648-52. Citado na pág. 86, 87.

[149] Stephens PJ, Devlin FJ, Chabalowski CF, Frisch MJ. Ab initio calculation of vibrational absorption and circular dichroism spectra using density functional force fields. The Journal of physical chemistry. 1994;98(45):11623-7. Citado na pág. 86.

[150] Ernzerhof M, Scuseria GE. Assessment of the Perdew–Burke–Ernzerhof exchange-correlation functional. The Journal of chemical physics. 1999;110(11):5029-36. Citado na pág. 86.

[151] Ren X, Rinke P, Joas C, Scheffler M. Random-phase approximation and its applications in computational chemistry and materials science. Journal of Materials Science. 2012;47:7447-71. Citado na pág. 86.

[152] Yanai T, Tew DP, Handy NC. A new hybrid exchange–correlation functional using the Coulomb-attenuating method (CAM-B3LYP). Chemical physics letters. 2004;393(1-3):51-7. Citado na pág. 87, 88.

[153] Casida ME, Jamorski C, Casida KC, Salahub DR. Molecular excitation energies to high-lying bound states from time-dependent density-functional response theory: Characterization and correction of the time-dependent local density approximation ionization threshold. The Journal of chemical physics. 1998;108(11):4439-49. Citado na pág. 87.

[154] Tozer DJ, Amos RD, Handy NC, Roos BO, Serrano-Andres L. Does density functional theory contribute to the understanding of excited states of unsaturated organic compounds? Molecular physics. 1999;97(7):859-68.

[155] Dreuw A, Weisman JL, Head-Gordon M. Long-range charge-transfer excited states in time-dependent density functional theory require non-local exchange. The Journal of chemical physics. 2003;119(6):2943-6.

[156] Bernasconi L, Sprik M, Hutter J. Time dependent density functional theory study of charge-transfer and intramolecular electronic excitations in acetone–water systems. The Journal of chemical physics. 2003;119(23):12417-31. Citado na pág. 87.

[157] Tawada Y, Tsuneda T, Yanagisawa S, Yanai T, Hirao K. A long-range-corrected time-dependent density functional theory. The Journal of chemical physics. 2004;120(18):8425-33. Citado na pág. 87.

[158] Iikura H, Tsuneda T, Yanai T, Hirao K. A long-range correction scheme for generalized-gradient-approximation exchange functionals. The Journal of Chemical Physics. 2001;115(8):3540-4. Citado na pág. 87.

[159] Seminario JM. Recent developments and applications of modern density functional theory. 1996. Citado na pág. 87.

[160] Charaf-Eddin A, Planchat A, Mennucci B, Adamo C, Jacquemin D. Choosing a functional for computing absorption and fluorescence band shapes with TD-DFT. Journal of chemical theory and computation. 2013;9(6):2749-60. Citado na pág. 88.

[161] Laurent AD, Jacquemin D. TD-DFT benchmarks: a review. International Journal of Quantum Chemistry. 2013;113(17):2019-39. Citado na pág. 88.

[162] Vezie MS, Few S, Meager I, Pieridou G, Dörling B, Ashraf RS, et al. Exploring the origin of high optical absorption in conjugated polymers. Nature materials. 2016;15(7):746-53. Citado na pág. 88.

[163] Huzinaga S, Andzelm J, Radzio-Andzelm E, Sakai Y, Tatewaki H, Klobukowski M. Gaussian basis sets for molecular calculations. Elsevier; 2012. Citado na pág. 88, 90, 91.

[164] Woon DE, Dunning Jr TH. Gaussian basis sets for use in correlated molecular calculations. IV. Calculation of static electrical response properties. The Journal of chemical physics. 1994;100(4):2975-88. Citado na pág. 89.

[165] Kahn K, Bruice TC. Systematic convergence of energies with respect to basis set and treatment of electron correlation: focal-point conformational analysis of methanol. Theoretical Chemistry Accounts. 2004;111:18-24. Citado na pág. 90.

[166] Champagne B, Mosley DH, Vracko M, André JM. Electron-correlation effects on the static longitudinal polarizability of polymeric chains. Physical Review A. 1995;52(1):178. Citado na pág. 90.

[167] Volkov A, Li X, Koritsanszky T, Coppens P. Ab initio quality electrostatic atomic and molecular properties including intermolecular energies from a transferable theoretical pseudoatom databank. The Journal of Physical Chemistry A. 2004;108(19):4283-300. Citado na pág. 90.

[168] Davidson ER, Feller D. Basis set selection for molecular calculations. Chemical Reviews. 1986;86(4):681-96. Citado na pág. 93.

[169] Adhikari B, Majumdar S. Polymers in sensor applications. Prog Polym Sci. 2004;29:699. Citado na pág. 94.

[170] Jain R, Jadon N, Pawaiya A. Polypyrrole based next generation electrochemical sensors and biosensors: A review. Trends Analyt Chem. 2017;97:363. Citado na pág. 94.

[171] Beija M, Charreyrea MT, Martinho JMG. Dye-labelled polymer chains at specific sites: Synthesis by living/controlled polymerization. Prog Polym Sci. 2011;36:568. Citado na pág. 94.

[172] Lee K, Povlich LK, Kim J. Recent advances in fluorescent and colorimetric conjugated polymer-based biosensors. Analyst. 2010;135:2179.

[173] Breul AM, Hager MD, Schubert US. Fluorescent monomers as building blocks for dye labeled polymers: synthesis and application in energy conversion, biolabeling and sensors. Chem Soc Rev. 2013;42:5366. Citado na pág. 94.

[174] Korri-Youssoufi H, Makrouf B. Electrochemical biosensing of DNA hybridization by ferrocenyl groups functionalized polypyrrole. Anal Chem Acta. 2002;469:85. Citado na pág. 94.

[175] Ledwon P, Brzeczek A, Pluczyk S, Jarosz T, Kuznik W, Walczak K, et al. Synthesis and electrochemical properties of novel, donor–acceptor pyrrole derivatives with 1,8-naphthalimide units and their polymers. Electrochim Acta. 2014;128:420.

[176] Almeida AKA, Monteiro MP, Dias JMM, Omena L, da Silva AJC, Tonholo J, et al. Synthesis and spectroscopic characterization of a fluorescent pyrrole derivative containing electron acceptor and donor groups. Spectrochim Acta, Part A. 2014;128:812. Citado na pág. 94.

[177] Pazin WM, Almeida AKA, Manzoni V, Dias JMM, de Abreu ACF, Navarro M, et al. Thermal and solvatochromic effects on the emission properties of a thienyl-based dansyl derivative. RSC Adv. 2020;10:28484. Citado na pág. 94, 97.

[178] Wan X, Liu S. Fluorescent water-soluble responsive polymers site-specifically labeled with FRET dyes possessing pH- and thermo-modulated multicolor fluorescence emissions as dual ratiometric probes. J Mater Chem. 2011;21:10321. Citado na pág. 94.

[179] Pietsch C, Hoogenboom R, Schubert US. PMMA based soluble polymeric temperature sensors based on UCST transition and solvatochromic dyes. Polym Chem. 2010;1:1005. Citado na pág. 94.

[180] Coelho ECS, Nascimento VB, Ribeiro AS, Navarro M. Electrochemical and optical properties of new electrochromic and fluorescent nitrobenzoyl polypyrrole derivatives. Electrochim Acta. 2014;123:441. Citado na pág. 94.

[181] Szunerits S, Bouffier L, Calemczuk R, Corso B, Demeunynck M, Descamps E, et al. Comparison of Different Strategies on DNA Chip Fabrication and DNA-Sensing: Optical and Electrochemical Approaches. Electroanalysis. 2005;17:2001. Citado na pág. 94.

[182] MBR, Dadsetan M, Baltrusaitis J, Knight AM, Ruesink T, EAL, et al. The development of electrically conductive polycaprolactone fumarate–polypyrrole composite materials for nerve regeneration. Biomater. 2010;31:5916. Citado na pág. 94.

[183] Moroder P, Runge MB, Wang H, Ruesink T, Lu L, Spinner RJ, et al. Material properties and electrical stimulation regimens of polycaprolactone fumarate–polypyrrole scaffolds as potential conductive nerve conduits. Acta Biomater. 2011;7:944. Citado na pág. 94.

[184] Lin Q, Yang Y, Ma Y, Zhang R, Wang J, Chen X, et al. Bandgap Engineered Polypyrrole–Polydopamine Hybrid with Intrinsic Raman and Photoacoustic Imaging Contrasts. Nano Lett. 2018;18:7485. Citado na pág. 94.

[185] Song X, Liang C, Gong H, Chen Q, Wang C, Liu Z. Photosensitizer-Conjugated Albumin-Polypyrrole Nanoparticles for Imaging-Guided In Vivo Photodynamic/Photothermal Therapy. Small. 2015;11:3932. Citado na pág. 94.

[186] Shiraishi Y, Yamamoto K, Sumiya S, Hirai T. Selective fluorometric detection of aromatic thiols by a chemosensor containing two electrophilic sites with different local softness. Chem Commun. 2013;49:11680. Citado na pág. 94.

[187] Maity D, Raj A, Karthigeyan D, Kundu TK, Govindaraju T. Reaction-based probes for Co(II) and Cu(I) with dual output modes: fluorescence live cell imaging. RSC Adv. 2013;3:16788. Citado na pág. 95.

[188] Seo YH, Jeon SH, Shim BJ, Shin IS. Electrochemistry and electrochemiluminescence of resorufin dye: Synergetic reductive-oxidation boosted by hydrogen peroxide. Electrochim Acta. 2022;436:141432.

[189] Pei SL, Zhang J, Ge W, Liu C, Sheng R, Zeng L, et al. A resorufin-based fluorescence probe for visualizing biogenic amines in cells and zebrafish. RSC Adv. 2022;12:33870.

[190] Saini A, Messenger H, Kisley L. Fluorophores "Turned-On" by Corrosion Reactions Can Be Detected at the Single-Molecule Level. ACS Appl Mater Interfaces. 2021;13:2000. Citado na pág. 94, 95.

[191] Zhang H, Xu L, Chen W, Huang J, Huang C, Sheng J, et al. Simultaneous Discrimination of Cysteine, Homocysteine, Glutathione, and $H_2S$ in Living Cells through a Multisignal Combination Strategy. Anal Chem. 2019;91:1904. Citado na pág. 94.

[192] Gao X, Li X, Li L, Zhou J, Ma H. A simple fluorescent off-on probe for the discrimination of cysteine from glutathione. Chem Commun. 2015;51:9388.

[193] Ma T, Ding H, Xu H, Lv Y, Liu H, Wang H, et al. Dual-functional probes for sequential thiol and redox homeostasis sensing in live cells. Analyst. 2015;140:322. Citado na pág. 94.

[194] Han BH, Zhou ML, Vellimana AK, Milner E, Kim DH, Greenberg JK, et al. Resorufin analogs preferentially bind cerebrovascular amyloid: potential use as imaging ligands for cerebral amyloid angiopathy. Mol Neurodeg. 2011;6:86. Citado na pág. 95.

[195] Porcal GV, Previtali CM, Bertolotti SG. Photophysics of the phenoxazine dyes resazurin and resorufin in direct and reverse micelles. Dyes Pigm. 2009;80:206. Citado na pág. 95.

[196] Flamigni L, Venuti E, Camaioni N, Barigelletti F. A Spectroscopic Investigation of the Temperature and Solvent Sensitivities of Resorufin. J Chem Soc, Faraday Trans 2. 1989;85:1935. Citado na pág. 95.

[197] Kurnikova MG, Balabai N, Waldeck DH, Coalson RD. Rotational Relaxation in Polar Solvents. Molecular Dynamics Study of Solute-Solvent Interaction. J Am Chem Soc. 1998;120:6121. Citado na pág. 95.

[198] Montejano HA, Gervaldo M, Bertolotti SG. The excited-states quenching of resazurin and resorufin by p-benzoquinones in polar solvents. Dyes Pigm. 2005;64:117. Citado na pág. 95, 99.

[199] Ribeiro AS, A Kanazawa, Navarro NMAF, Moutet JC, Navarro M. Synthesis of (R)-() and (S)-(+)-3-(1-pyrrolyl)propyl- N-(3,5-dinitrobenzoyl)-$\alpha$-phenylglycinate and derivatives. A suitable chiral polymeric phase precursor. Tetrahedron: Asymmetry. 1999;10:3735. Citado na pág. 95, 96, 98.

[200] Peach MJG, Benfield P, Helgaker T, Tozer DJ. Excitation energies in density functional theory: An evaluation and a diagnostic test . J Chem Phys. 2008;128:044118. Citado na pág. 97.

[201] Roy A, Datar A, Kand D, Saha T, Talukdar P. A fluorescent off–on NBD-probe for F$^-$ sensing: theoretical validation and experimental studies. Org Biomol Chem. 2014;12:2143.

[202] Pedone A. Role of solvent on charge transfer in 7-aminocoumarin dyes: New hints from TD-CAM-B3LYP and state specific PCM calculations. J Chem Theory Comput. 2013;9:4087. Citado na pág. 97.

[203] Tomasi J, Mennucci B, Cances E. The IEF version of the PCM solvation method: an overview of a new method addressed to study molecular solutes at the QM ab initio level. J Mol Struct (Theochem). 1999;464:211. Citado na pág. 97.

[204] da Luz de Sousa I, Ximenes VF, de Souza AR, Morgon NH, et al. Solvent-induced Stokes' shift in DCJTB: Experimental and theoretical results. J Mol Struct. 2019;1192:186. Citado na pág. 97.

[205] Liu Y, Xu Q, Liu L, Wang L, He D, Zhuang X, et al. The spectral-shapes of absorption, emission, ECD and CPL of a fluorene-fused [7]helicene: Vibronic effect and solvent inhomogenous broadening. Spectrochim Acta, Part A. 2021;249:119293. Citado na pág. 97.

[206] Frisch MJ, Trucks GW, Schlegel HB, Scuseria GE, Robb MA, Cheeseman JR, et al. Gaussian 09, Revision C.01; 2010. Citado na pág. 97.

[207] Cui Z, Coletta C, Dazzi A, Lefrancois P, Gervais M, Néron S, et al. Radiolytic Method as a Novel Approach for the Synthesis of Nanostructured Conducting Polypyrrole. Langmuir. 2014;30:14086. Citado na pág. 99.

[208] Yu J, Berg M. Resorufin as a probe for the dynamics of solvation by hydrogen bonding. Chem Phys Lett. 1993;208:315. Citado na pág. 101, 102.

[209] Bueno C, Villegas ML, Bertolotti SG, Previtali CM, Neumann MG, Encinas MV. The excited-state interaction of resazurin and resorufin with amines in aqueous solutions. photophysics and photochemical reaction. Photochem Photobiol. 2002;76:385.

[210] Porcal GV, Altamirano MS, Glusko CA, Bertolotti SG, Previtali CM. Photophysical properties of the phenoxazin dyes resazurin and resorufin in soybean lecithin microemulsions. Dyes Pigm. 2011;88:240. Citado na pág. 101, 103.

[211] Lakowicz JR. Principles of Fluorescence Spectroscopy. 3rd ed. Springer; 2006. Citado na pág. 102.

[212] Ravi M, Samanta A, Radhakrishnan TP. Excited state dipole moments from an efficient analysis of solvatochromic stokes shift data. J Phys Chem. 1994;98:9133. Citado na pág. 102.

[213] Nekoukar Z, Zakariaei Z, Taghizadeh F, Musavi F, Banimostafavi ES, Sharifpour A, et al. Methanol poisoning as a new world challenge: A review. Ann Med Surg. 2021;66:102445. Citado na pág. 105.

[214] Priyadarsini KI. Photophysics, photochemistry and photobiology of curcumin: Studies from organic solutions, bio-mimetics and living cells. Journal of Photochemistry and Photobiology C: Photochemistry Reviews. 2009 06;10:81-95. Citado na pág. 107.

[215] Mohammed F, Rashid-Doubell F, Cassidy S, Henari FZ. A comparative study of the spectral, fluorometric properties and photostability of natural curcumin, iron- and boron-complexed curcumin. Spectrochimica Acta Part A: Molecular and Biomolecular Spectroscopy. 2017 08;183:439-50. Citado na pág. 107.

[216] Basnet P, Skalko-Basnet N. Curcumin: An Anti-Inflammatory Molecule from a Curry Spice on the Path to Cancer Treatment. Molecules. 2011 06;16:4567-98. Citado na pág. 107.

[217] Pulido-Moran M, Moreno-Fernandez J, Ramirez-Tortosa C, Ramirez-Tortosa M. Curcumin and Health. Molecules. 2016 02;21:264. Available from: https://www.mdpi.com/1420-3049/21/3/264.

[218] Das KC, Das CK. Curcumin (diferuloylmethane), a singlet oxygen ((1)O(2)) quencher. Biochemical and Biophysical Research Communications. 2002 07;295:62–66. Available from: https://pubmed.ncbi.nlm.nih.gov/12083767/.

[219] Funk JL, Frye JB, Oyarzo JN, Kuscuoglu N, Wilson J, McCaffrey G, et al. Efficacy and mechanism of action of turmeric supplements in the treatment of experimental arthritis. Arthritis and rheumatism. 2006;54:3452-64. Available from: https://www.ncbi.nlm.nih.gov/pubmed/17075840.

[220] Zeng L, Yang T, Yang K, Yu G, Li J, Xiang W, et al. Efficacy and Safety of Curcumin and Curcuma longa Extract in the Treatment of Arthritis: A Systematic Review and Meta-Analysis of Randomized Controlled Trial. Frontiers in Immunology. 2022 07;13. Citado na pág. 107.

[221] Chignell CF, Bilski P, Reszka KJ, Motten AG, Sik RH, Dahl TA. Spectral and photochemical properties of curcumin. Photochemistry and Photobiology. 1994 03;59:295–302. Available from: https://pubmed.ncbi.nlm.nih.gov/8016208/. Citado na pág. 107.

[222] Nardo L, Paderno R, Andreoni A, Másson M, Haukvik T, TØnnesen HH. Role of H-bond formation in the photoreactivity of curcumin. Spectroscopy. 2008 01;22:187-98. Citado na pág. 107.

[223] Pantiora P, Furlan V, Matiadis D, Mavroidi B, Perperopoulou F, Papageorgiou AC, et al. Monocarbonyl Curcumin Analogues as Potent Inhibitors against Human Glutathione Transferase P1-1. Antioxidants. 2022 12;12:63. Citado na pág. 107.

[224] Clariano M, Marques V, Vaz JR, Awam S, Afonso MB,  M, et al. Monocarbonyl Analogs of Curcumin with Potential to Treat Colorectal Cancer. Chemistry  Biodiversity. 2023 03;20.

[225] MaruYama T, Yamakoshi H, Iwabuchi Y, Shibata H. Mono-Carbonyl Curcumin Analogs for Cancer Therapy. Biological  pharmaceutical bulletin. 2023 06;46:756-63. Citado na pág. 107.

[226] Lozanovski Z, Stanoeva JP, Bogdanov J. Development of a spectrophotometric method for assessment of the relative reactivity of monocarbonyl analogs of curcumin with 2-

(dimethylamino)ethanethiol. Macedonian Journal of Chemistry and Chemical Engineering. 2023 06;42. Citado na pág. 107.

[227] Rayanal M, Pralhad Pujar P, D S. Studies on Photophysical Properties of Mono-carbonyl Curcumin Analogues: Experimental and Theoretical approach. Oriental Journal of Chemistry. 2018 07;34:2170-9. Citado na pág. 107.

[228] Kunwar A, Barik A, Pandey R, Priyadarsini KI. Transport of liposomal and albumin loaded curcumin to living cells: An absorption and fluorescence spectroscopic study. Biochimica et Biophysica Acta (BBA) - General Subjects. 2006 10;1760:1513-20. Citado na pág. 107.

[229] Alsantali RI, Mughal EU, Naeem N, Alsharif MA, Sadiq A, Ali A, et al. Flavone-based hydrazones as new tyrosinase inhibitors: Synthetic imines with emerging biological potential, SAR, molecular docking and drug-likeness studies. Journal of Molecular Structure. 2022;1251:131933. Citado na pág. 108.

[230] Itoh T. Fluorescence and phosphorescence from higher excited states of organic molecules. Chemical reviews. 2012;112(8):4541-68. Citado na pág. 112.

[231] Effect of Solvent on the Excited-state Photophysical Properties of Curcumin¶. Citado na pág. 112.

[232] Al-Khayri JM, Sahana GR, Nagella P, Joseph BV, Alessa FM, Al-Mssallem MQ. Flavonoids as potential anti-inflammatory molecules: A review. Molecules. 2022;27(9):2901. Citado na pág. 117.

[233] Cheng AX, Zhang X, Han XJ, Zhang YY, Gao S, Liu CJ, et al. Identification of chalcone isomerase in the basal land plants reveals an ancient evolution of enzymatic cyclization activity for synthesis of flavonoids. New Phytologist. 2018;217(2):909-24. Citado na pág. 117.

[234] Li S, Yang Y, Yu J, Zhou H, Hou Z, Wang X. Molecular and metabolic insights into purplish leaf coloration through the investigation of two mulberry (Morus alba) genotypes. BMC Plant Biology. 2024;24(1):61. Citado na pág. 117.

[235] Manetas Y. Why some leaves are anthocyanic and why most anthocyanic leaves are red? Flora-Morphology, Distribution, Functional Ecology of Plants. 2006;201(3):163-77. Citado na pág. 117.

[236] Wang HK. The therapeutic potential of flavonoids. Expert opinion on investigational drugs. 2000;9(9):2103-19. Citado na pág. 117.

[237] Swetha TK, Priya A, Pandian SK. Flavonoids for therapeutic applications. Plant metabolites: Methods, applications and prospects. 2020:347-78.

[238] Brandi ML. Flavonoids: biochemical effects and therapeutic applications. Bone and mineral. 1992;19:S3-S14. Citado na pág. 117.

[239] Rammohan A, Reddy JS, Sravya G, Rao CN, Zyryanov GV. Chalcone synthesis, properties and medicinal applications: a review. Environmental Chemistry Letters. 2020;18:433-58. Citado na pág. 117.

[240] Rozmer Z, Perjési P. Naturally occurring chalcones and their biological activities. Phytochemistry reviews. 2016;15:87-120. Citado na pág. 117.

[241] Karthikeyan C, SH Narayana Moorthy N, Ramasamy S, Vanam U, Manivannan E, Karunagaran D, et al. Advances in chalcones with anticancer activities. Recent patents on anti-cancer drug discovery. 2015;10(1):97-115. Citado na pág. 117.

[242] Mahapatra DK, Bharti SK, Asati V. Anti-cancer chalcones: Structural and molecular target perspectives. European journal of medicinal chemistry. 2015;98:69-114.

[243] Kumar V, Dhawan S, Girase PS, Awolade P, Shinde SR, Karpoormath R, et al. Recent advances in chalcone-based anticancer heterocycles: A structural and molecular target perspective. Current Medicinal Chemistry. 2021;28(33):6805-45.

[244] Michalkova R, Mirossay L, Gazdova M, Kello M, Mojzis J. Molecular mechanisms of antiproliferative effects of natural chalcones. Cancers. 2021;13(11):2730. Citado na pág. 117.

[245] v Kostanecki S, Tambor J. Ueber die sechs isomeren Monooxybenzalacetophenone (Monooxychalkone). Berichte der deutschen chemischen Gesellschaft. 1899;32(2):1921-6. Citado na pág. 117.

[246] Rudrapal M, Khan J, Dukhyil AAB, Alarousy RMII, Attah EI, Sharma T, et al. Chalcone scaffolds, bioprecursors of flavonoids: Chemistry, bioactivities, and pharmacokinetics. Molecules. 2021;26(23):7177. Citado na pág. 117.

[247] Sibat AS. Synthesis and antibacterial activity of 4'-methoxy-5, 7-dimethoxyflavanone & 2, 4-(4-butylphenyl)-5, 7-dimethoxychroman-4-one. 2023. Citado na pág. 118.

[248] Rullah K, Mohd Aluwi MFF, Yamin BM, Juan JC, Wai LK. Palladium-catalysed cross-coupling reactions for the synthesis of chalcones. Asian Journal of Organic Chemistry. 2019;8(8):1174-93. Citado na pág. 118.

[249] Sain S, Jain S, Srivastava M, Vishwakarma R, Dwivedi J. Application of palladium-catalyzed cross-coupling reactions in organic synthesis. Current Organic Synthesis. 2019;16(8):1105-42. Citado na pág. 118.

[250] Shen C, Wu XF. Palladium-Catalyzed Carbonylative Multicomponent Reactions. Chemistry-A European Journal. 2017;23(13). Citado na pág. 118.

[251] Urbán B, Papp M, Skoda-Földes R. Carbonylation of aryl halides in the presence of heterogeneous catalysts. Current Green Chemistry. 2019;6(2):78-95. Citado na pág. 118.

[252] D Jandial D, A Blair C, Zhang S, S Krill L, Zhang YB, Zi X. Molecular targeted approaches to cancer therapy and prevention using chalcones. Current cancer drug targets. 2014;14(2):181-200. Citado na pág. 118.

[253] Mahapatra DK, Bharti SK, Asati V. Chalcone scaffolds as anti-infective agents: Structural and molecular target perspectives. European journal of medicinal chemistry. 2015;101:496-524.

[254] Kar Mahapatra D, Asati V, Bharti SK. An updated patent review of therapeutic applications of chalcone derivatives (2014-present). Expert opinion on therapeutic patents. 2019;29(5):385-406. Citado na pág. 118.

[255] Aksöz BE, Ertan R. Spectral properties of chalcones II. Fabad J Pharm Sci. 2012;37(4):205-16. Citado na pág. 119.

[256] Xue Y, Gong X. The conformational, electronic and spectral properties of chalcones: A density functional theory study. Journal of Molecular Structure: THEOCHEM. 2009;901(1-3):226-31. Citado na pág. 119, 123.

# THE AVERAGE VALUE OF ONE-ELECTRON AND TWO-ELECTRON

## OPERATORS

From the equations (6.18) and (6.20), since the electrons are indistinguishable, it is observed that the expected value of the operator $\mathcal{O}_1$ is:

$$\langle \psi \,|\mathcal{O}_1|\, \psi \rangle = \left\langle \psi \left| \sum_{i=1}^{n} h(i) \right| \psi \right\rangle \tag{A.1}$$

Applying the operator $h(i)$ to the Hartree-Fock wave function:

$$\langle \psi \,|\mathcal{O}_1|\, \psi \rangle = \frac{1}{n!} \sum_{i=1}^{n} \sum_{k=1}^{n!} \sum_{j=1}^{n!} (-1)^{p_k}(-1)^{p_j}$$
$$\times \left\langle \widehat{\mathcal{P}}_k \left\{ \chi_1(1)\chi_2(2)\ldots\chi_n(n) \right\} |h(i)| \widehat{\mathcal{P}}_j \left\{ \chi_1(1)\chi_2(2)\ldots\chi_n(n) \right\} \right\rangle \tag{A.2}$$

However, we can observe that all terms are equivalent due to the symmetry of the permuted wave functions[1]. Therefore, we can express the expected value in terms of a single index $i$ and multiply it by the number of particles $n$, as the contributions are the same. Thus, the expression for the expected value of the operator $\mathcal{O}_1$ is:

$$\langle \psi \,|\mathcal{O}_1|\, \psi \rangle = n\frac{1}{n!} \sum_{k=1}^{n!} \sum_{j=1}^{n!} (-1)^{p_k}(-1)^{p_j}$$
$$\times \left\langle \widehat{\mathcal{P}}_k \left\{ \chi_1(1)\chi_2(2)\ldots\chi_n(n) \right\} |h(1)| \widehat{\mathcal{P}}_j \left\{ \chi_1(1)\chi_2(2)\ldots\chi_n(n) \right\} \right\rangle \tag{A.3}$$

Here, all terms contribute to the expected value, and the expression has been simplified using the symmetry of the permuted wave functions. Thus,

---

[1]Particles that obey Fermi-Dirac statistics (such as electrons, protons, and neutrons) are called fermions and their permuted wave functions are antisymmetric. This means that when two particles are exchanged, the overall wave function changes sign.

$$\langle \psi \, |\mathcal{O}_1| \, \psi \rangle = n\langle \psi | h(1) | \psi \rangle = \frac{1}{(n-1)!} \sum_{i=1}^{n!} \sum_{j=1}^{n!} (-1)^{p_i} (-1)^{p_j}$$

$$\times \left\langle \widehat{\mathcal{P}}_i \left\{ \chi_1(1)\chi_2(2) \ldots \chi_n(n) \right\} | h(1) | \widehat{\mathcal{P}}_j \left\{ \chi_1(1)\chi_2(2) \ldots \chi_n(n) \right\} \right\rangle$$

(A.4)

In the above summations, only the terms with $i = j$ will remain, because if $\widehat{\mathcal{P}}_i \neq \widehat{\mathcal{P}}_j$, the electrons $2, 3, \ldots, n$ will occupy different positions in the permutations and the integrals over their positions will consequently be zero. In fact, to show that only the terms with $i = j$ contribute to the above sum, let us consider two permutations $\hat{\mathcal{P}}_i$ and $\hat{\mathcal{P}}_j$, where $i \neq j$. This means that at least two electrons occupy different positions in the two permutations, say, without loss of generality, that they are electrons $k$ and $l$, with $k < l$. Then, we can write:

$$\hat{\mathcal{P}}_i \left\{ \chi_1(1)\chi_2(2) \ldots \chi_k(k) \ldots \chi_l(l) \ldots \chi_n(n) \right\} = \left\{ \chi_1(i_1)\, \chi_2(i_2) \ldots \chi_k(i_l) \ldots \chi_l(i_k) \ldots \chi_n(i_n) \right\}$$

(A.5)

where $i_1, i_2, \ldots, i_n$ is a permutation of the indices $1, 2, \ldots, n$ that differs from the permutation $1, 2, \ldots, n$ of the initial configuration only in the positions of the electrons $k$ and $l$. Similarly, we can write:

$$\hat{\mathcal{P}}_j \left\{ \chi_1(1)\chi_2(2) \ldots \chi_k(k) \ldots \chi_l(l) \ldots \chi_n(n) \right\} = \left\{ \chi_1(j_1)\, \chi_2(j_2) \ldots \chi_k(j_l) \ldots \chi_l(j_k) \ldots \chi_n(j_n) \right\}$$

(A.6)

where $j_1, j_2, \ldots, j_n$ is a permutation of the indices $1, 2, \ldots, n$ that differs from the permutation $1, 2, \ldots, n$ of the initial configuration only in the positions of the electrons $k$ and $l$.

Considering the integral:

$$\left\langle \hat{\mathcal{P}}_i \left\{ \chi_1(1)\chi_2(2) \ldots \chi_k(k) \ldots \chi_l(l) \ldots \chi_n(n) \right\} | h(1) | \hat{\mathcal{P}}_j \left\{ \chi_1(1)\chi_2(2) \ldots \chi_k(k) \ldots \chi_l(l) \ldots \chi_n(n) \right\} \right\rangle$$

(A.7)

When $i \neq j$, the positions occupied by electrons $k$ and $l$ are different in the two permutations, which implies that the coordinates of these electrons are different in the two wave functions.

Therefore, the integral over all the coordinates of the electrons of two integrands with different wave functions due to the exchange of two electrons, by symmetry, must be zero.

As a consequence, only the permutations that keep the electrons $k$ and $l$ in their corresponding positions in the original permutation (i.e., those for which $i = j$) contribute to the sum. Thus,

$$\int d\mathbf{r}_1 d\mathbf{r}_2 \ldots d\mathbf{r_n} \psi^* \left( \mathbf{r}_{\alpha_{1,i}}, \mathbf{r}_{\alpha_{2,i}}, \ldots, \mathbf{r}_{\alpha_{n,i}} \right) h(1) \psi \left( \mathbf{r}_{\alpha_{1,j}}, \mathbf{r}_{\alpha_{2j}}, \ldots, \mathbf{r}_{\alpha_{n,j}} \right) = 0 \quad \text{for } i \neq j \quad \text{(A.8)}$$

This means that, in the original equation for $\langle \psi | \mathcal{O}_1 | \psi \rangle$, the terms with $i \neq j$ are zero, and we can rewrite the equation as:

$$\langle \psi | \mathcal{O}_1 | \psi \rangle = \frac{1}{(n-1)!} \sum_{i=1}^{n!} \left\langle \hat{\mathcal{P}}_i \left\{ \chi_1(1)\chi_2(2) \ldots \chi_n(n) \right\} | h(1) | \hat{\mathcal{P}}_i \left\{ \chi_1(1)\chi_2(2) \ldots \chi_n(n) \right\} \right\rangle$$
$$\text{(A.9)}$$

In this case, the Hartree-Fock wave function reduces to:

$$\langle \psi | \mathcal{O}_1 | \psi \rangle = \left\langle \psi \left| \sum_{i=1}^{n} h(i) \right| \psi \right\rangle = n \langle \psi | h(1) | \psi \rangle \qquad \text{(A.10)}$$

This is a crucial result because it shows that the expectation value of a single-particle operator in the Hartree-Fock approximation can be evaluated using the single-particle wave functions (orbitals) rather than the full $n$-particle wave function. Thus, it provides a significant simplification for calculating expectation values in many-body systems. The same argument can be applied to the operator $\mathcal{O}_2$ and its expectation value is similarly obtained.

# VARIATIONAL PRINCIPLE AND THE PROPERTIES OF

# HERMITIAN MATRICES

Theorem 1 (Variational Theorem). Given a normalized wave function, $\Phi$, the expected value of the Hamiltonian operator in this state is greater than or equal to the exact ground state energy.

The functional to be minimized is given by the expression (6.21), with the restriction that the states are orthonormal, that is,

$$\langle \alpha \mid \beta \rangle - \delta_{\alpha\beta} = 0 \tag{B.1}$$

where $\delta_{\alpha\beta}$ is the Kronecker delta. This problem can be solved using the technique of Lagrange multipliers, which consists of minimizing the new functional:

$$\mathcal{L} = E - \sum_{\alpha,\beta} \varepsilon_{\alpha\beta} \left( \langle \alpha \mid \beta \rangle - \delta_{\alpha\beta} \right) \tag{B.2}$$

where $\varepsilon_{\alpha\beta}$ are the Lagrange multipliers. These multipliers are elements of a Hermitian matrix, since, as $E$ is real, it is imposed that $\mathcal{L}$ is real.

It is important to highlight some properties of Hermitian matrices. A matrix $A$ is Hermitian if and only if $A = A^\dagger$, where $A^\dagger$ is the adjoint matrix of $A$. The adjoint matrix of $A$ is the transpose and complex conjugate of $A$. Therefore, the elements of a Hermitian matrix satisfy the condition:

$$A_{\alpha\beta} = A_{\beta\alpha}^* \tag{B.3}$$

where $A_{\alpha\beta}$ is the matrix element at position $(\alpha, \beta)$ and $A_{\beta\alpha}^*$ is the complex conjugate of the element at position $(\beta, \alpha)$. And, since the Lagrange multipliers $\varepsilon_{\alpha\beta}$ form this type of matrix, we can write:

$$\varepsilon_{\alpha\beta} = \varepsilon_{\beta\alpha}^* \tag{B.4}$$

This is the condition that must be satisfied by the Lagrange multipliers $\varepsilon_{\alpha\beta}$ to form a

Hermitian matrix. Note that it is square and has dimensions equal to the number of states we are considering. Additionally, the diagonal elements of the Hermitian matrix are real, as $\varepsilon_{\alpha\alpha} = \varepsilon_{\alpha\alpha}^*$, implying that the imaginary part must be zero.

The main interest is to calculate a small variation $\delta\mathcal{L}$, such that each state undergoes a small variation $\delta$. Thus, considering only the linear terms, we obtain

$$\delta\mathcal{L} = \delta E - \sum_{\alpha,\beta} \varepsilon_{\alpha\beta}(\langle \delta\alpha \mid \beta \rangle + \langle \alpha \mid \delta\beta \rangle) \tag{B.5}$$

To calculate the variation $\delta\mathcal{L}$, we must first observe that the variation $\delta E$ can be obtained from:

$$\delta E = \delta\langle\psi|\widehat{\mathbf{H}}|\psi\rangle = \sum_{\alpha=1}^{n} \delta\langle\alpha|h|\alpha\rangle + \frac{1}{2}\sum_{\alpha,\beta} \delta\langle\alpha\beta|\alpha\beta\rangle \tag{B.6}$$

Now, let's calculate the variation of the constraint $\delta(\langle \alpha \mid \beta \rangle - \delta_{\alpha\beta})$. Since $\delta_{\alpha\beta}$ does not depend on $\psi$, the variation is simply:

$$\delta(\langle \alpha \mid \beta \rangle - \delta_{\alpha\beta}) = \delta\langle \alpha \mid \beta \rangle \tag{B.7}$$

Then, the variation $\delta\mathcal{L}$ can be written as:

$$\delta\mathcal{L} = \delta E - \sum_{\alpha,\beta} \varepsilon_{\alpha\beta}\delta(\langle \alpha \mid \beta \rangle - \delta_{\alpha\beta}) \tag{B.8}$$

Substituting the variation $\delta(\langle \alpha \mid \beta \rangle - \delta_{\alpha\beta})$ into the equation above, we obtain:

$$\delta\mathcal{L} = \delta E - \sum_{\alpha,\beta} \varepsilon_{\alpha\beta}\delta\langle \alpha \mid \beta \rangle \tag{B.9}$$

Note that $\delta\langle \alpha \mid \beta \rangle$ can be decomposed into two parts:

$$\delta\langle \alpha \mid \beta \rangle = \langle \delta\alpha \mid \beta \rangle + \langle \alpha \mid \delta\beta \rangle \tag{B.10}$$

Substituting this expression into the equation for $\delta\mathcal{L}$, we obtain:

$$\delta\mathcal{L} = \delta E - \sum_{\alpha,\beta} \varepsilon_{\alpha\beta}(\langle \delta\alpha \mid \beta \rangle + \langle \alpha \mid \delta\beta \rangle) \tag{B.11}$$

Thus, considering only the linear terms, the variation $\delta\mathcal{L}$ is given by the above expression. Let's expand $\delta E$ using the expression for $E(\psi)$, (6.21). Thus,

$$\delta E = \delta\langle\psi|\widehat{\mathbf{H}}|\psi\rangle = \delta\left[\sum_{\alpha=1}^{n}\langle\alpha|h|\alpha\rangle + \frac{1}{2}\sum_{\alpha,\beta}\langle\alpha\beta|\alpha\beta\rangle\right] \tag{B.12}$$

First, let's expand the term $\delta\langle\alpha|h|\alpha\rangle$:

$$\delta\langle\alpha|h|\alpha\rangle = \langle\delta\alpha|h|\alpha\rangle + \langle\alpha|h|\delta\alpha\rangle \tag{B.13}$$

Next, let's expand the term $\delta\langle\alpha\beta|\alpha\beta\rangle$:

$$\delta\langle\alpha\beta|\alpha\beta\rangle = \langle\delta\alpha\beta|\alpha\beta\rangle + \langle\alpha\beta|\delta\alpha\beta\rangle - \langle\delta\alpha\beta|\beta\alpha\rangle - \langle\alpha\beta|\delta\beta\alpha\rangle \tag{B.14}$$

Substituting these expansions into the expression for $\delta E$, we obtain:

$$\delta E = \sum_{\alpha=1}^{n}(\langle\delta\alpha|h|\alpha\rangle + \langle\alpha|h|\delta\alpha\rangle) + \sum_{\alpha,\beta}\{((\langle\delta\alpha\beta \mid \alpha\beta\rangle + \langle\alpha\beta \mid \delta\alpha\beta\rangle)$$
$$- (\langle\delta\alpha\beta \mid \beta\alpha\rangle + \langle\alpha\beta \mid \delta\beta\alpha\rangle)\} \tag{B.15}$$

Substituting (B.15) into (B.12) and rearranging the terms, we find the expression

$$\delta\mathcal{L} = \sum_{\alpha}\langle\delta\alpha|h|\alpha\rangle + \sum_{\alpha,\beta}(\langle\delta\alpha\beta \mid \alpha\beta\rangle - \langle\delta\alpha\beta \mid \beta\alpha\rangle) - \sum_{\alpha,\beta}\varepsilon_{\alpha\beta}\langle\delta\alpha \mid \beta\rangle + \mathcal{CC} \tag{B.16}$$

# DERIVATION OF THE ENERGY VARIATION

Consider the variation of $\tilde{E} \equiv \tilde{E}[\rho]$ with respect to $n_i$,

$$\frac{\partial \tilde{E}}{\partial n_i} = t_i + \sum_{j \neq i} n_j \frac{\partial t_j}{\partial n_i} + \int v(\mathbf{r}) \frac{\partial \rho(\mathbf{r})}{\partial n_i} d^3\mathbf{r} + \iint \frac{\partial \rho(\mathbf{r})}{\partial n_i} \frac{\rho(\mathbf{r}')}{|\mathbf{r} - \mathbf{r}'|} d^3\mathbf{r} d^3\mathbf{r}' + \int \frac{\delta E_{xc}}{\delta \rho} \frac{\partial \rho}{\partial n_i} d^3\mathbf{r} \quad \text{(C.1)}$$

where, using (6.68), it can be obtained

$$\frac{\partial \tilde{E}}{\partial n_i} = t_i + \sum_{j \neq i} n_j \frac{\partial t_j}{\partial n_i} + \int v(\mathbf{r}) \frac{\partial \rho(\mathbf{r})}{\partial n_i} d^3\mathbf{r} + \iint \frac{\partial \rho(\mathbf{r})}{\partial n_i} \frac{\rho(\mathbf{r}')}{|\mathbf{r} - \mathbf{r}'|} d^3\mathbf{r} d^3\mathbf{r}' + \int \frac{\delta E_{xc}}{\delta \rho} \frac{\partial \rho}{\partial n_i} d^3\mathbf{r} \quad \text{(C.2)}$$

By substituting equation (6.68) into the external potential integral, we have:

$$\int v(\mathbf{r}) \frac{\partial \rho(\mathbf{r})}{\partial n_i} d^3\mathbf{r} = \int v^{KS}(\mathbf{r}) \frac{\partial \rho(\mathbf{r})}{\partial n_i} d^3\mathbf{r} - \int \frac{\rho(\mathbf{r}')}{|\mathbf{r} - \mathbf{r}'|} \frac{\partial \rho(\mathbf{r})}{\partial n_i} d^3\mathbf{r} d^3\mathbf{r}' - \int \frac{\delta E_{xc}}{\delta \rho} \frac{\partial \rho}{\partial n_i} d^3\mathbf{r} \quad \text{(C.3)}$$

Substituting this expression into equation (C.2), we have:

$$\frac{\partial \tilde{E}}{\partial n_i} = t_i + \sum_{j \neq i} n_j \frac{\partial t_j}{\partial n_i} + \int v^{KS} \frac{\partial \rho}{\partial n_i} d^3\mathbf{r} - \int \frac{\rho(\mathbf{r}')}{|\mathbf{r} - \mathbf{r}'|} \frac{\partial \rho(\mathbf{r})}{\partial n_i} d^3\mathbf{r} d^3\mathbf{r}' - \int \frac{\delta E_{xc}}{\delta \rho} \frac{\partial \rho}{\partial n_i} d^3\mathbf{r} \quad \text{(C.4)}$$

Therefore, the final expression is:

$$\frac{\partial \tilde{E}}{\partial n_i} = t_i + \sum_{j \neq i} n_j \frac{\partial t_j}{\partial n_i} + \int v^{KS} \frac{\partial \rho}{\partial n_i} d^3\mathbf{r} \quad \text{(C.5)}$$

From equation (6.68), we have:

$$\frac{\partial v^{KS}}{\partial n_i} = \frac{\partial}{\partial n_i} \left( v(\mathbf{r}) + \int \frac{\rho(\mathbf{r}')}{|\mathbf{r} - \mathbf{r}'|} d^3\mathbf{r}' + v_{xc}[\rho] \right)$$
$$= \int \frac{\partial \rho(\mathbf{r}')}{\partial n_i} \frac{1}{|\mathbf{r} - \mathbf{r}'|} d^3\mathbf{r}' + \frac{\delta v_{xc}}{\delta \rho} \frac{\partial \rho}{\partial n_i} \tag{C.6}$$

Substituting into the expression for $\frac{\partial \tilde{E}}{\partial n_i}$, we have:

$$\frac{\partial \tilde{E}}{\partial n_i} = t_i + \sum_{j \neq i} n_j \frac{\partial t_j}{\partial n_i} + \int \left( v^{KS} - \int \frac{\partial \rho(\mathbf{r}')}{\partial n_i} \frac{1}{|\mathbf{r} - \mathbf{r}'|} d^3\mathbf{r}' - \frac{\delta v_{xc}}{\delta \rho} \frac{\partial \rho}{\partial n_i} \right) \frac{\partial \rho}{\partial n_i} d^3\mathbf{r}$$
$$+ \iint \frac{\partial \rho(\mathbf{r})}{\partial n_i} \frac{\rho(\mathbf{r}')}{|\mathbf{r} - \mathbf{r}'|} d^3\mathbf{r} d^3\mathbf{r}' + \int \frac{\delta E_{xc}}{\delta \rho} \frac{\partial \rho}{\partial n_i} d^3\mathbf{r}$$
$$= t_i + \sum_{j \neq i} n_j \frac{\partial t_j}{\partial n_i} + \int v^{KS} \frac{\partial \rho}{\partial n_i} d^3\mathbf{r} - \iint \frac{\partial \rho(\mathbf{r})}{\partial n_i} \frac{\rho(\mathbf{r}')}{|\mathbf{r} - \mathbf{r}'|} d^3\mathbf{r}' d^3\mathbf{r} \tag{C.7}$$
$$+ \int \frac{\delta v_{xc}}{\delta \rho} \frac{\partial \rho}{\partial n_i} \frac{\partial \rho}{\partial n_i} d^3\mathbf{r} + \int \frac{\delta E_{xc}}{\delta \rho} \frac{\partial \rho}{\partial n_i} d^3\mathbf{r}$$

Note that in the second equality we used the definition of $v^{KS}$ given in (6.68) and the previously obtained expression for $\frac{\partial v^{KS}}{\partial n_i}$.

We can write the above expression more compactly as:

$$\frac{\partial \tilde{E}}{\partial n_i} = t_i + \sum_j n_j \frac{\partial t_j}{\partial n_i} + \int \frac{\delta E_{xc}}{\delta \rho} \frac{\partial \rho}{\partial n_i} d^3\mathbf{r} + \int v^{KS}(\mathbf{r}) \frac{\partial \rho}{\partial n_i} d^3\mathbf{r} \tag{C.8}$$

$$+ \int \frac{\delta v_{xc}}{\delta \rho(\mathbf{r})} \frac{\partial \rho(\mathbf{r})}{\partial n_i} d^3\mathbf{r} - \iint \frac{\rho(\mathbf{r}')}{|\mathbf{r} - \mathbf{r}'|} \frac{\partial \rho(\mathbf{r})}{\partial n_i} d^3\mathbf{r} d^3\mathbf{r}'. \tag{C.9}$$

$$\frac{\partial \tilde{E}}{\partial n_i} = t_i + \sum_{j \neq i} n_j \frac{\partial t_j}{\partial n_i} + \int v^{KS} \frac{\partial \rho}{\partial n_i} d^3\mathbf{r} \tag{C.10}$$

From equation (6.72), one obtains

$$\frac{\partial t_j}{\partial n_i} = \int \frac{\partial \psi_j^*}{\partial n_i} \left( -\frac{1}{2} \nabla^2 \right) \psi_j d^3\mathbf{r} + \mathcal{CC} \tag{C.11}$$

where $\mathcal{CC}$ denotes the complex conjugate. Therefore, using expression (6.72) and the fact that $\partial \rho(\mathbf{r})/\partial n_i = |\psi_i(\mathbf{r})|^2 + \sum_{j \neq i} n_j \partial |\psi_j(\mathbf{r})|^2 /\partial n_i$, expression (C.10) can be rewritten as

$$\frac{\partial \tilde{E}}{\partial n_i} = \varepsilon_i - \int \psi_i^* \left( v^{KS}[\rho] \right) \psi_i d^3\mathbf{r} + \sum_{j\neq i} n_j \left[ \int \frac{\partial \psi_j^*}{\partial n_i} \left( -\frac{1}{2}\nabla^2 \right) \psi_j d^3\mathbf{r} + \mathcal{CC} \right]$$

$$+ \int v^{KS} \left[ |\psi_i(\mathbf{r})|^2 + \sum_{j\neq i} n_j \frac{\partial |\psi_j(\mathbf{r})|^2}{\partial n_i} \right] d^3\mathbf{r} \tag{C.12}$$

$$\frac{\partial \tilde{E}}{\partial n_i} = \varepsilon_i + \sum_{j\neq i} n_j \left[ \int \frac{\partial \psi_j^*}{\partial n_i} \left( -\frac{1}{2}\nabla^2 + v^{KS} \right) \psi_j d^3\mathbf{r} + \mathcal{CC} \right]$$

or alternatively,

$$\frac{\partial \tilde{E}}{\partial n_i} = \varepsilon_i + \sum_{j\neq i} \varepsilon_j n_j \left[ \int \frac{\partial \psi_j^*}{\partial n_i} \psi_j d^3\mathbf{r} + \mathcal{CC} \right] = \varepsilon_i + \sum_{j\neq i} \varepsilon_j n_j \left[ \int \frac{\partial |\psi_j(\mathbf{r})|^2}{\partial n_i} d^3\mathbf{r} \right] \tag{C.13}$$

Since the states $\psi_j(\mathbf{r})$ are normalized, it is known that

$$\int \frac{\partial |\psi_j(\mathbf{r})|^2}{\partial n_i} d^3\mathbf{r} = \frac{\partial}{\partial n_i} \int |\psi_j(\mathbf{r})|^2 d^3\mathbf{r} = 0 \tag{C.14}$$

Thus, the final expression is

$$\frac{\partial \tilde{E}}{\partial n_i} = \varepsilon_i \tag{C.15}$$